Delft University of Technology

Faculty of Aerospace Engineering

Delft, June 23, 2017

Plasma Actuators in Space-Based Systems

Name: Dimitrije Petković
Student number: 4162722

Thesis committee:

Ir. P. P. Sundaramoorthy,	TU Delft, Supervisor
Dr. A. Cervone	TU Delft, Chair of Assessment Committee
Dr. R. Pereira,	TU Delft
Dr. M. Kotsonis	TU Delft

Abstract

Plasma actuators are fully electronic devices without any moving mechanical parts. Hence they have increased reliability and lower complexity when compared to conventional actuators used for same purposes. Mobile components also contribute to increased vibrations, noise, loss of energy and they require lubrication. Non-thermal plasma actuators are highly efficient as they directly convert electrical into kinetic energy without use of any mechanical parts. Lack of mobile components in plasma actuators contribute to lower mass, meaning lower cost of spacecrafts. Another benefit related to use of these actuators is their short response time, which increases dynamical and control abilities of complete spacecraft. All the benefits just stated make this technology potentially very interesting for space-based applications. Presented thesis represents feasibility study, a first step required for application of plasma actuator on a spacecraft.

This research examined two objectives. First was to study the effect of an altitude on momentum exchange between high velocity external flow and created ionic wind. Second objective was to investigate and design DBD plasma actuator able to withstand orbital thermal loads. This study consists of literature research on two most common plasma actuators; various aspects of launch, orbit and re-entry of spacecrafts; and two analytical models. First model aims in estimating the influence of an altitude on the actuator force creation, which can be used for shock stand-off distance modification, and thus steering applications. Other model aims in estimating actuator thermal loads occurring due to spacecraft orbit in Low Earth Orbit. Results show that altitude has large effect on actuator force production. Analytical model shows an average reduction of 4.51 or 4.44 times per 10 km, depending on actuator's orientation with respect to external flow. Difficulties relating high velocity flow fields such as molecular dissociation and very high friction heat loads are presented. Results show that DBD actuator system can produced significant perturbations between spacecraft surface and natural shockwave. Made perturbations are in form of a compression wave that interacts with natural shock wave and creates a dis-balance of forces proficient for spacecraft reentry steering. Second analytical model shows that there exist actuator materials which can withstand thermal loads due to spacecraft orbital Sun exposure. This thesis shows a promising first order results needed to qualify and apply DBD actuator on spacecraft. However much research on optimization and design are still required.

Contents

List of Acronyms

AC Alternating Current

CAD Computer Aided Design

DBD Dielectric Barrier Discharge

DC Direct Current

ECSS European Cooperation for Space Standardization

EHD Electrohydrodynamic

FEM Finite Element Method

FWHM Full Width Half Maximum

GEO Geostationary Equatorial Orbit

HV High Voltage

IPA Isopropyl Alcohol

JB Jacchia-Bowman

LEO Low Earth Orbit

MEK Methyl Ethyl Ketone

NRLMSISE Naval Research Laboratory Mass Spectrometer Incoherent Scatter Radar Extended Model

PIV Particle Image Velocimetry

PMMA Poly(methyl methacrylate)

PMT Photomultiplier-Tube

RCS Reaction Control System

List of Figures

List of Tables

1 INTRODUCTION

Plasma actuators are fully electronic devices that were originally developed to create ozone gas. The most researched plasma actuators are corona discharge and Dielectric Barrier Discharge (DBD) actuators. The most interesting area for implementation of this technology is on trains and lorries. Miniaturization allowed application of this technology in several other areas, but up until now, this technology has not found mass commercial usage in aerospace industry. In aircraft industry, plasma actuators are used for modification of boundary layer characteristics; in order to decrease drag, increase lift and delay stall angle. This can be achieved with two or more electrodes positioned at specific points on top of the wing. If high voltage is applied, air between two electrodes ionizes. Charged ions gain acceleration and collide with neutral atmospheric particles. During collision, momentum is transferred resulting in two phenomena, ionic wind and electrohydrodynamic (EHD) force. More information about actuators and physics behind them can be found in Chapter 2.

To this date non-thermal plasma actuators are still not used in any space-based system. This created an opportunity to research something innovative, interesting and potentially very efficient. In order to apply plasma actuators on spacecrafts, the first step is to conduct feasibility study, with a goal of testing actuator's performance in conditions expected to occur during spacecraft's lifetime. Major benefits associated with plasma actuators are low mass, cost and power consumption; high robustness, short response time and low simulation computational efforts. All of the benefits just stated make this technology potentially very interesting for space-based applications. If they are to be exploited, a feasibility study is required. Idea behind this research is to perform a first step in determining if usage of plasma actuators is feasible in space-based operations.

Research Questions and Thesis Outline

In order to perform feasibility study, literature review was conducted and resulted in three research questions. For the sake of simplicity this thesis defines spacecraft's life into three stages, namely launch, orbit and re-entry. First two research questions investigate actuator's ability to operate under conditions expected to occur during launch and re-entry, while third deals with thermal loads expected to occur during spacecraft's orbit. Plasma actuators could potentially be operated during launch and re-entry of spacecrafts. Hence in order to be operational during re-entry, they have to withstand harsh environmental effects related to orbital flight phase. The most critical effect on orbiting spacecraft are large temperature gradients resulted from change in energy flux due to spacecraft's cyclic exposure to Sun. Thus proper design of actuator materials has to be performed. Research questions are presented below:

1) Is it feasible to operate plasma actuators in (1) flow characterized by large Mach number; and under (2) atmospheric conditions defined by altitude variations?

2) Can plasma actuator be used for spacecraft steering applications?

3) How can plasma actuator be designed in order to withstand thermal loads occurring during spacecraft orbits?

Thesis outline represents necessary path required for answering research questions. It will help the reader orient while going through chapters. Thesis is divided into two parts: first deals with launch or re-entry stages and second concerns spacecraft's survivability during orbital stage. Thesis outline is presented in Figure 1.1. Chapter 2 is an introductory, and has aim to provide information about corona discharge and DBD actuator types. Development background, physical and electrical properties of both plasma actuators along with related advantages and disadvantages will be presented. Based on Chapter 2 decision is made on which actuator type to consider for rest of this thesis.

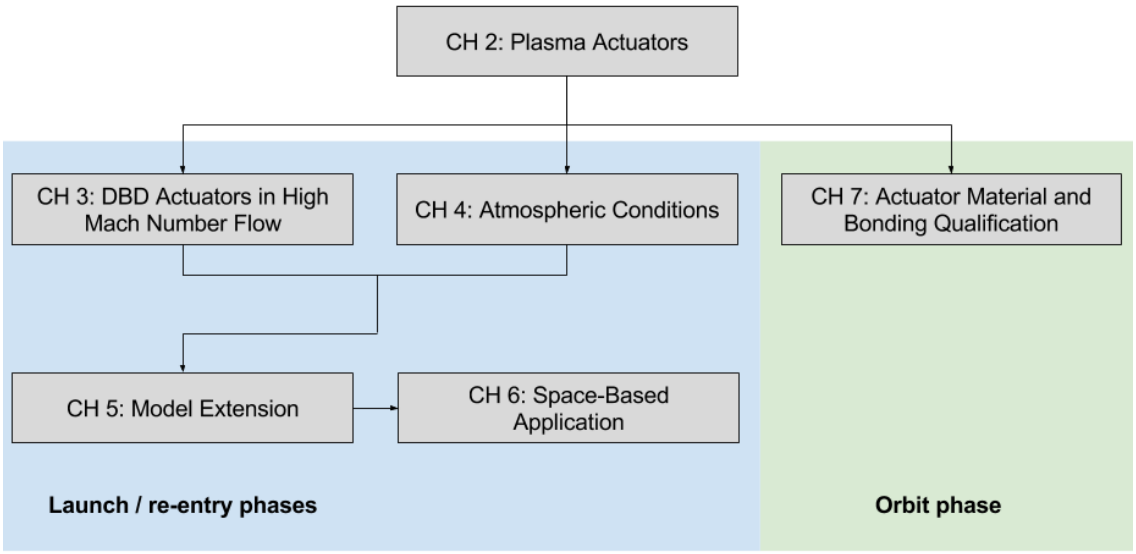

Figure 1.1: Thesis outline

Chapter 3 presents literature on DBD actuators used in high Mach number. In this chapter Mach limit is defined based on problems related to molecular dissociation that occur at large Mach numbers and simple space-based application is showed. In order to find operational altitude range for plasma actuators, Chapter 4 uses three atmospheric models to plot density, temperature, pressure, number of atmospheric constituents and mean free path as a function of geometric altitude; and dynamic viscosity and gas constant as a function of temperature. Combination of chapters 2, 3 and 4 gave required limitations and parameters needed in order to modify and extend model made by [Pereira, 2016]. This model computes actuator force, shear friction force and modeled load cell force as a function of free-stream velocity. Originally this model was used at sea level conditions, but after some modifications and made assumptions one is able to use it until 50 km altitude. In order to provide answer to second research question, chapters 2, 3, 4 and 5 are combined and give space-based application for spacecraft during launch or re-entry. DBD actuator is positioned very close

to stagnation point on circular cylinder. According to [Nishihara et al., 2011] DBD actuator could produce compression wave that travels towards and collides with neutral bow shock, increasing its stand-off distance by 25%. In Chapter 6 relation between shock stand-off distance and pressure distribution on cylindrical body is presented. This chapter deals with an idea that a change in pressure on body surface could be potentially used in spacecraft steering application during its launch or re-entry phases.

In order to give answer related to third research question, Chapter 7 presents parametric modeling and test definition required for actuator qualification. Modelling using ANSYS is performed in order to test thermal loads and related deflections. Stresses are result of uneven expansions or contractions resulted from different coefficients of expansion that each actuator component has. Validation of this model and qualification of different dielectric materials and adhesives shall be done using experiments defined in Section 7.2. Due to cost and time budgets limitation qualification tests were not performed. They provide a first step needed in order to safely use plasma actuators in space-based systems, that hopefully someone will investigate in near future.

To summaries introduction, this Master's thesis shall investigate following:

- Background information and physics behind corona discharge and DBD actuators;
- Information on DBD actuators in high Mach number flow fields;
- Definition of atmospheric conditions as a function of altitude;
- DBD actuator's performance as a function of altitude for fixed M=5 flow field, using adapted [Pereira, 2016] model. Filling the knowledge gap, as currently no research is conducted on altitudes higher than 12 km. This thesis covers altitudes up to 50 km;
- Possible actuator application for spacecraft or rocket steering at flow field defined by M=5;
- Modeling of actuator stresses and deformations due to orbital thermal cycling; and
- Definition of test required for actuator qualification

2 PLASMA ACTUATORS

Goal of this chapter is to introduce and choose between two major plasma actuator types currently used in aerospace industry. First section covers background and some physical properties of corona discharge actuators. Due to drawbacks concerning discharge stability of this actuator type, in second section a single dielectric barrier discharge actuator is going to be introduced. Its beneficial characteristics, research interest and its development at Aerospace Faculty of TU Delft were determinant factors for choosing DBD actuator for space-based application exploration.

2.1 Corona Discharge Actuators

Aim of this section is to present surface corona discharge actuator by discussing its background, phenomenon behind electric wind and related electrical properties.

2.1.1 Background and actuator physics

The first cold atmospheric plasma actuator that was researched, developed and used was corona discharge actuator. This actuator type is used due to its simplicity to produce and run by inducing weak ionic wind close to surface wall. When in, 1985 Direct Current (DC) surface corona discharge plasma actuator was state of the art, [Goldman et al., 1985] defined corona discharge as a *"gas discharge where the geometry confines the gas ionizing processes to high-field ionization region(s) around the active electrode(s)"*. This definition was revisited by [Schutze et al., 1998] and adapted for the DC corona discharge. Newly definition states that *"the corona discharge is a weakly luminous discharge, which usually appears at atmospheric pressure near sharp points or thin wires, where the electric field is sufficiently large"*. [Schutze et al., 1998] considers corona as one of two possible discharge types. Depending on field potential it is either a Townsend discharge or a negative glow discharge. Townsend mechanism is a condition where source of free electrons and a strong electric field are required to produce a discharge in an avalanche manner. Where, the avalanche manner is characterized by a electron multiplication that occurs during cascade ionization. This mechanism represents one of the fundamental mechanisms in the ionization process.

[Moreau, 2007] considers case of two plane electrodes placed at sea level atmospheric conditions with DC high voltage applied between them. [Moreau, 2007] states that under the electric field, electrons situated in a gap between two electrodes are created by the photo-ionization. According to the author: *"photo-ionization happens due to fact that electrons that are accelerated toward the anode, ionize atmospheric gas by collision with neutral molecules such as* $A + e^- \longrightarrow A^+ + 2e^-$ *where A is a neutral particle and* A^+ *is the positive ion"* [Moreau, 2007]. Author states that due to multiplication of electron that proceeds along their drift from cathode to anode, an avalanche is developed. This results in a discharge that creates a current. Figure 2.1 shows schematic representing corona discharge actuator in a point-to-plane configuration. In Figure 2.1, high voltage point and grounded electrode are named injection and collecting electrodes, respectively [Leger et al., 2002]. It can be observed that the gap between high voltage sharp point electrode and grounded plane is divided in two zones. Zone which is closer to high voltage tip and being much smaller, few tenths

of millimeter in length, is called ionization zone [Moreau, 2007]. Second zone is much larger and is called ion drift zone. Using configuration from Figure 2.1 one can produce either positive or negative corona. If the strong electric field is situated near anode or cathode, produced corona is either positive or negative respectively.

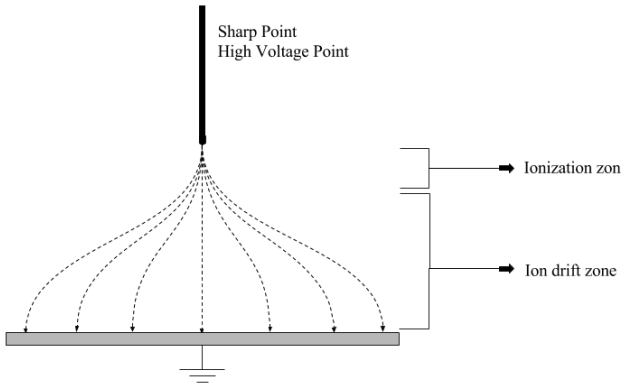

Figure 2.1: Point-to-plate corona discharge actuator as defined by [Moreau, 2007]

Production of electrons in positive corona occurs due to photo ionization in the electrode gap [Moreau, 2007]. As high voltage or strong electric field is applied at anode, electrons created in gap will accelerate towards anode, and produce an avalanche effect. When electrons enter ionization zone near sharp tip they are forced back towards cathode due to Coulomb forces and enter ion drift zone where they collide into grounded electrode. Author makes an assumption that no recombination occurs as the electric field is not sufficiently strong [Moreau, 2007]. This assumption was not properly explained and no reference was given to give some insight. Difficulties arose when it was desired to find what is the highest applicable electric field strength for any given configuration. When considering negative coronas author makes another assumption. [Moreau, 2007] assumes that positive ions (which are created by detachment in ionization zone) go quickly towards sharp point. Similarly to positive corona, negative ions instead of positive are created, and accelerated towards the grounded electrode.

2.1.2 Electric wind

In both positive and negative corona, ions that travel through gap between two electrodes will collide with neutral fluid and transfer gained momentum. Change of momentum results in creation of two important phenomena called electric wind and Electrohydrodynamic (EHD) force. One of the oldest relevant scientific paper that could be found concerning electric wind is written by [Robinson, 1961]. Author defines an electric wind as: *"the movement of gas induced by the repulsion of ions from the vicinity of a high-voltage discharge electrode"* [Robinson, 1961]. He states that the knowledge of ionic wind as phenomenon was known back in 1709 but its potential was not used up until the twentieth century. Nowadays electric wind together with second phenomenon EHD force are used in many applications [Corke et al., 2007]. Representation of the electrohydrodynamic actuator made by [Leger et al., 2002] is showed in Figure 2.2.

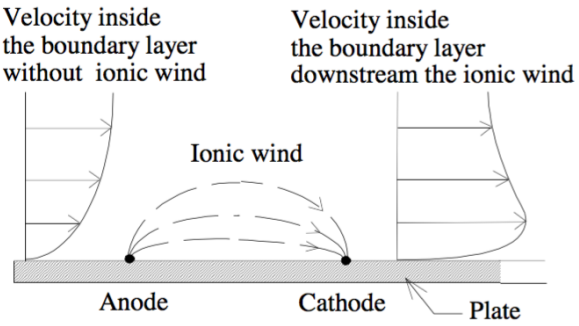

Figure 2.2: Electrohydrodynamic (EHD) actuator as defined by [Leger et al., 2002]

Figure 2.2 shows that the ionic wind introduced tangentially and very close to flat plate increases velocity inside boundary layer close to the flat plate. This is beneficial due to several reasons. It modifies boundary layer in such a way that it can shift transition from laminar to turbulent flow over flat surface such as an aircraft wing. Shift in transition point means that larger part of the wing can be used for lift production. Modification of boundary layer also influences skin friction drag, acoustic and vibrational noises inside aircraft structure. All of these beneficial attributes are the reasons behind an increasing number of scientists and engineers that are looking into plasma actuators. In proceedings of this section electric wind as a part of surface corona discharge actuator will be covered. Later there will be dedicated sections for the electric wind and EHD force.

One of the most important electro-mechanical parameter of corona discharge actuator is so called electrohydrodynamical number N_{EHD}. Electrohydrodynamical number can be computed using Equation 2.1, *"it represents a ratio of corona discharge-induced body force to inertial force on the gas"* [Moreau, 2007].

$$N_{EHD} = \frac{i}{l\rho\mu u^2} \tag{2.1}$$

Where:

- i is the time averaged discharge current
- ρ is the fluid density
- l is the electrode length
- μ is the ion mobility
- u is the local air flow velocity

If this dimensionless number approaches zero one may say that the airflow is not affected by electric wind produced by plasma actuator. However, if N_{EHD} approaches infinity one may say that free air stream is considerably affected.

According to [Moreau, 2007] researches cannot find a common ground when on reason behind creation of electric wind. Some of them believe that electric wind results from ion drift; while the others argue that the streamer propagation is its main cause. Author believes that electric wind can be induced by combination of both phenomena [Moreau, 2007]. To compute electric wind velocity [Moreau, 2007] uses expression made by

[Robinson, 1961] and modified by [Sigmond and Lågstad, 1993]. This expression is presented in Equation 2.2:

$$V_G = \sqrt{\frac{i \cdot d}{\rho \cdot \mu \cdot A_G}} \tag{2.2}$$

Where:

i is the time-averaged discharge current

d is the electrode gap

ρ is the gas density

μ is the ion mobility

A_G is the discharge cross-section

2.1.3 Electrical properties

Electrical properties of the surface corona discharge will be covered in next following paragraphs. Results from this sub-section were adapted from [Moreau, 2007]. Study carried by the author uses configuration depicted in Figure 2.3.

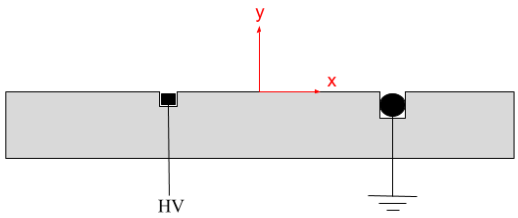

Figure 2.3: Electrode geometrical configuration found in DC surface wire-to-wire configuration [Moreau, 2007]

In Figure 2.3 it can be observed that High Voltage (HV) anode electrode has a smaller area. By doing so, a stronger electric field can be induced in a cathode. In above configuration anode can be characterized by a point, while cathode by a plane [Moreau, 2007]. Author declares that four distinctive regimes exist in surface coronas. Each regime manifests itself differently with different current values. These are presented below:

- The first with the lowest current density value is called spot regime. To obtain a higher current density value regime one needs to increase $\frac{voltage}{electrode\ gap}$ ratio.
- Second regime is called streamer discharge regime. *"Its current density ranges from 0.2 to 0.5 mAm^{-1}"* [Moreau, 2007].
- Third regime which is interesting for aerospace applications is named glow discharge and it is known as typical corona. It has two very important features which streamer discharge regime lacks, namely stability and reachable high current.

- Fourth (the most undesirable) regime is called filamentary regime. In this regime current levels are too high, which makes it very hard to control. Due to high $\frac{voltage}{electrode\ gap}$ ratio, spark can be seen on surface between two electrodes. This should be remembered as it will be one of the reasons for development of DBD actuators.

[Moreau, 2007] claims that when corona is in the streamer regime, current will be composed out of two components. First component happens as a result of ion drifting and second comes from a streamer propagation. When discharge goes from streamer into glow regime second current component disappears making discharge act similar to a low pressure glow. [Moreau, 2007] found a relation of current against air-stream velocity obtained on a flat plate as a function of free stream velocity; and is presented in Figure 2.4.

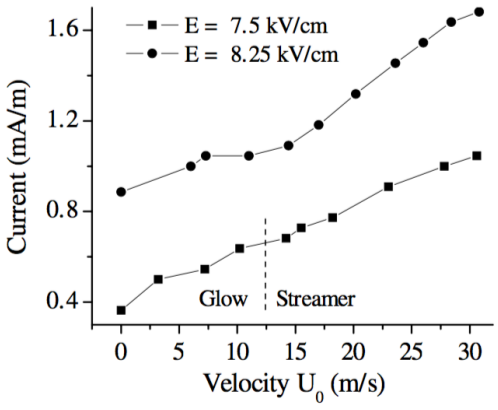

Figure 2.4: Curent versus airstream velocity for two $\frac{voltage}{electrode\ gap}$ ratio values [Moreau, 2007]

Figure 2.4 clearly depicts almost linear trend where current density increases with free-stream velocity; that is in the same direction as the created ionic wind. This figure also shows that for the higher ratio $\frac{voltage}{electrode\ gap}$ greater current density values can be obtained with the same actuator components and their relative distances and sizes. Author also assume that electrical properties of surface discharge actuators change with varying different geometrical properties of setup (electrodes sizes and gap between them). Research shows that electrical properties of surface discharge actuators do not only vary with geometrical properties but also with different atmospheric conditions such as pressure, humidity and temperature of the surrounding gas [Moreau, 2007]. Based on many scientific works [Moreau, 2007] represents five main tendencies concerning electrical properties of surface discharge actuators. These are presented in the list below.

1. The cathode diameter should be as large as possible compared to the anode in order to make discharge more stable with less glow-to-arc transitions that are undesirable and uncontrollable.

2. When the temperature is under 60°C there will be no variations in discharge with ΔT. Under this condition discharge will only change with pressure variations.

3. Discharge stability decreases with an increase in relative air humidity.

4. Free air-stream notably modifies physical mechanisms and limits glow-to-arc transition; and finally

5. Dielectric wall surface is one of the most influential factors for the electrical properties of the surface discharge actuators

Using configuration from Figure 2.3 for different current densities, velocity profiles were computed as a function of distance from plate's surface. This can be seen in Figure 2.5, which shows a trend of increasing electric wind velocity with current density levels. This figure also shows that the velocity is highest when the distance from the surface is from 1 mm to 2 mm.

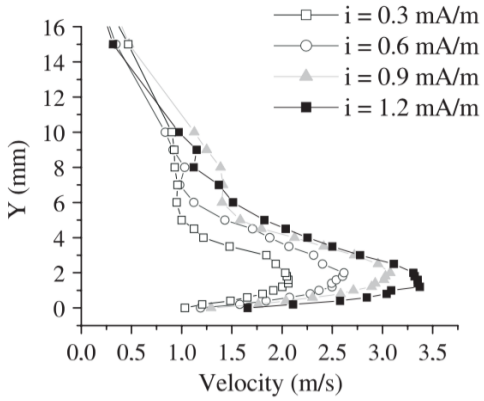

Figure 2.5: Vertical velocity profiles for different current values as defined by [Moreau, 2007]

Observing Figure 2.5, one may come to the conclusion that current density could be increased until the desirable ionic wind velocity is reached, but this is not true. As earlier stated it is very hard to control discharge when it goes into the filamentary regime, which is entered if ratio $\frac{voltage}{electrode\ gap}$ is increased beyond glow-to-arc transition point. [Moreau, 2007] argues that from a practical point of view, the maximum velocity measured until year 2007 was 5 m/s. Relationship found between ionic wind velocity and applied current density is presented in Equation 2.3

$$V_{Gmax} \propto \sqrt{I} \tag{2.3}$$

This means that after some point the benefits of higher ionic wind velocity are overrun by drawbacks of too high current. This is the reason why new actuator type had to be designed that could produce stronger ionic winds without the drawback of arcing and uncontrollable discharge. Section 2.2 is going to cover design and properties of so called DBD plasma actuator.

2.2 Single Dielectric Barrier Discharge Actuator

This section focuses on dielectric barrier discharge plasma actuator. Compared to surface corona plasma actuator, the most important difference is that *"DBD actuator can sustain a large-volume discharge at atmospheric pressure without the discharges collapsing into a constricted arc"* [Enloe et al., 2004]. Interesting reason why one should focus on this actuator type is that recent studies demonstrated that DBD plasma actuators can be operated at many different pressure levels [Balcon et al., 2009]. This plasma actuator type is the most globally used actuator. Most of the research on plasma actuators in last decade is done on investigating and improving performances of DBD type actuators. *"This tremendous growth in research stems from their special features, including the fact that they are fully electronic with no moving parts; a fast time response for unsteady applications; a very low mass, which is especially important in applications with high g-loads; the ability to apply the actuators onto surfaces without the addition of cavities or holes;*

the efficient conversion of the input power without parasitic losses when properly optimized; and the ability to simulate easily their effect in numerical flow solvers" [Corke et al., 2010].

2.2.1 Background and actuator physics

In this section background on DBD plasma actuators and physics behind them are going to be discussed. Schematic of the typical DBD actuator is presented in Figure 2.6. It shows that dielectric barrier discharge plasma actuator got its name from dielectric material in which second electrode is immersed so that it can be isolated. DBD plasma actuator consists out of one more electrode that is exposed to outside free-stream gas. Connection between electrodes is made by Alternating Current (AC) electric field. Input waveform for a classic DBD is usually AC sinusoidal signal. According to [Benard and Moreau, 2014] typical geometrical properties of this actuator type are electrode width of a few mm, electrode gap between encapsulated and air exposed electrode is in order of few mm or in majority cases zero (Figure 2.6), and dielectric material is usually made of Plexiglas, Kapton, Teflon, glass or ceramics. It should be noted that DBD plasma actuator can be operated using DC electric field. However, AC power supply is preferred over DC by most researches as related breakdown electric field E_b is lower [Corke et al., 2009].

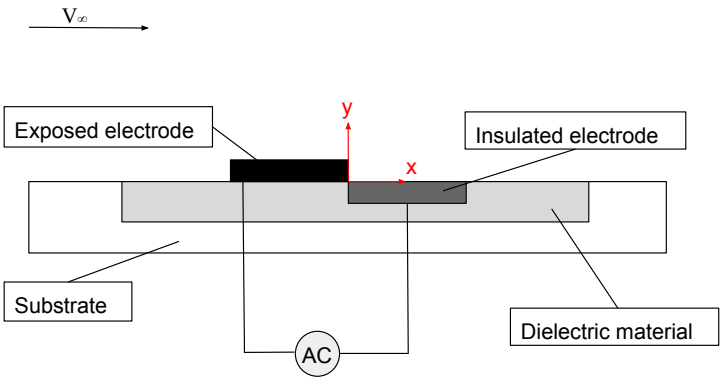

Figure 2.6: DBD plasma actuator

When amplitude of alternating current exceeds E_b gas above insulated electrode ionizes and becomes plasma. Ionization occurs through generation of electron-ion pairs, which require one condition. That is, there must be certain amount of free electrons present above insulated electrode [Corke et al., 2009]. The ionized air under unaided eye resembles uniformity in color and intensity. *"When time-resolved images are taken, they indicate that plasma above the covered electrode is highly dynamic, spatially evolving, non-equilibrium process with features that develop on the timescale of the AC period"* [Corke et al., 2010]. This can be clearly seen if one compares Figure 2.7 that is taken with a simple photo-camera and left part of Figure 2.8 taken with Photomultiplier-Tube (PMT). Both of these figures are adapted from [Corke et al., 2010] research.

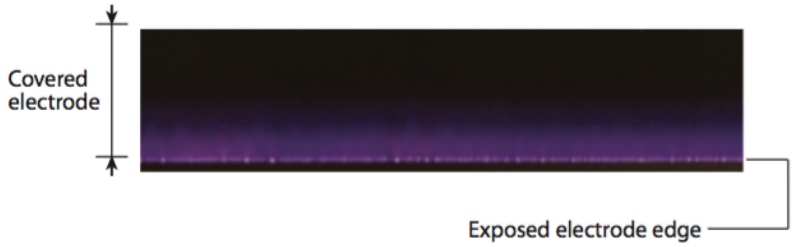

Figure 2.7: Ionization as a result of DBD actuation at sea level conditions [Corke et al., 2010]

According to [Corke et al., 2010] light emission time series is characterized by three properties:

1. Ionization of the air occurs only over a part of AC cycle
2. When it is ionized, air will have different properties and current strength will be different for each of the AC half-cycles
3. Light emission is made out of the numerous very narrow peaks showing that the discharge is not continuous but made out of many micro-discharges

Author backs up his statement by mentioning that several respected authors found same fundamental features. They all characterize this process as DBD [Corke et al., 2010]. Above mentioned features can easily be seen in Figure 2.8.

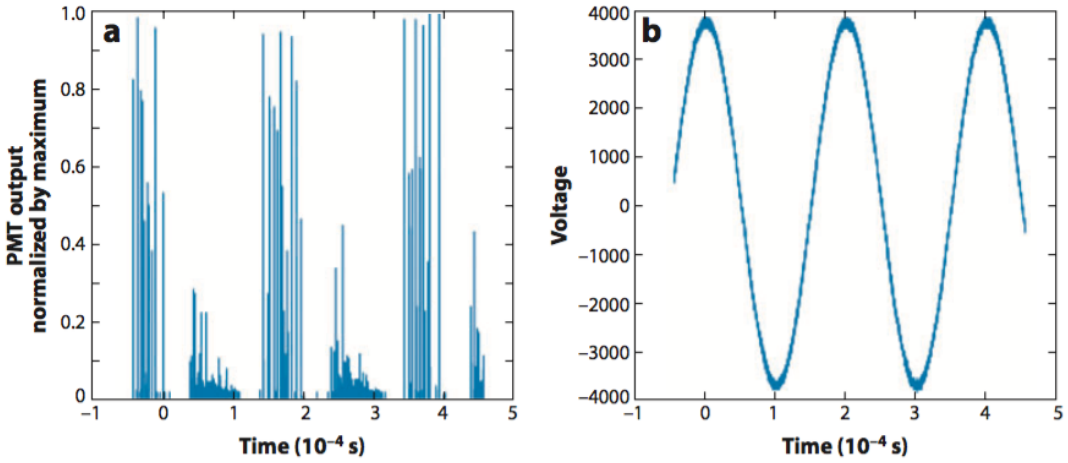

Figure 2.8: *"Time series of photomultiplier-tube output (a) that is viewing ionized-air light emission at one location over electrode covered by a dielectric and corresponding AC input (b) to a plasma actuator"* [Corke et al., 2010]

To prove the first property one has to observe part (a) of Figure 2.8. Between each group of peaks, greater and lesser, there are five distinctive periods of time where there is no photomultiplier-tube (PMT) output, meaning that air is ionized over certain sections of AC cycle. If one observes left side of Figure 2.8, three greater and three lesser groups of peaks can be found. Each of the peak group consists of numerous micro-discharges that prove third property. Right side of the same figure shows an AC input to a plasma actuator.

In it one can distinct two alternating sides from the sinusoidal waveform. These correspond to two half-cycles of AC. When compared (a) and (b) parts of Figure 2.8, it can be seen that grater PMT output peak groups correspond to the positive half of the AC cycles, and that lower correspond to the negative half. As the applied voltage is same, it can be said that character of the ionized air is different for each AC cycle side, proving second property.

Change in AC halves and corresponding phenomena that physically occurs at the plasma actuator was nicely explained and depicted by [Corke et al., 2007]. In their research authors use Figure 2.9, the illustration of electron drift that is dictated by each AC period.

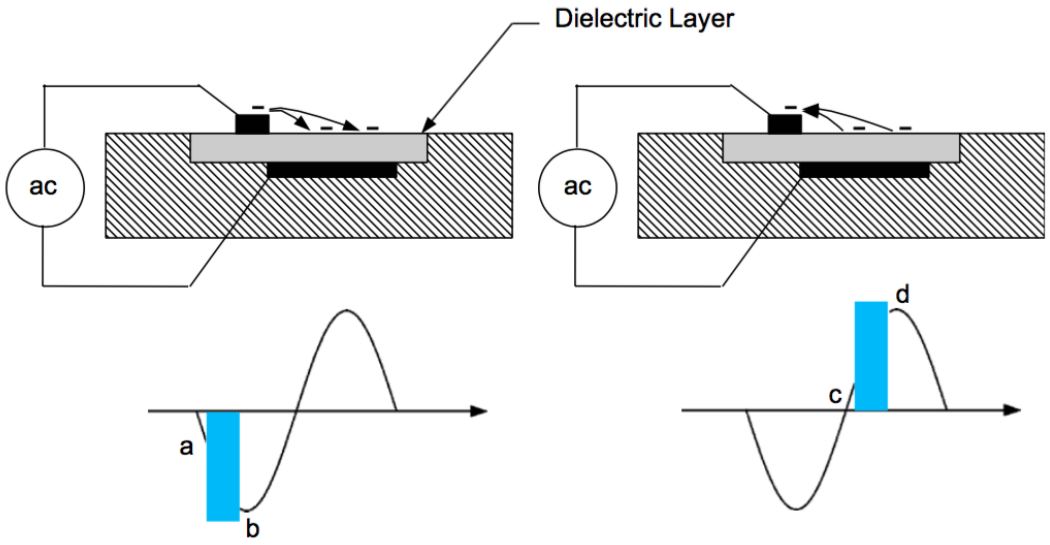

Figure 2.9: *"Illustration of electron drift that dictates portions of AC period where air ionizes Single Dielectric Barrier Discharge (SDBD) process"* [Corke et al., 2007]

According to [Corke et al., 2007] research, in particular the left side of Figure 2.9 it can be seen that less negative charge is positioned on dielectric surface and more negative is situated on top of air-exposed electrode. This means that charge on dielectric surface is going to build up. Left bottom corner from the Figure 2.9 depicts a blue rectangle in AC cycle. [Corke et al., 2007] use this rectangle to graphically represent part of the AC cycle where air is ionized. Knowing this information one can assume that ionization starts at position marked with letter (a) and diminishes at position marked with (b). Distance from (a) to (b) represents period of the cycle where potential difference between surfaces exceeds breakdown field value, which starts breakdown of electron-ion pairs and thus create plasma. If the applied voltage on air exposed electrode remains constant, discharge will be terminated as there will be no more potential difference between two surfaces due to charge build up in dielectric surface. When this occurs ionization stops; this is marked with (b). Other part of AC cycle and physical phenomena that occur in actuator are presented in the right side of Figure 2.9. It shows same phenomena but now in opposite direction. Discharge and ionization effect is due to transmission of electrons from dielectric surface to air exposed electrode which is in this case more positive surface. In this part of figure, [Corke et al., 2007] marks ionization period with letters (c) and (d).

To prove this theory, a new unrelated source had to be found. [Benard and Moreau, 2014] conducted an

experimental research in order to observe electrical and mechanical characteristics of AC DBD plasma actuators used for airflow control. Authors state that discharge is occurring during distinct periods in both halves of AC cycle. In their research [Benard and Moreau, 2014] prove statement said by [Pons et al., 2004] that the streamer discharge occurs during the positive-going cycle and that glow-like discharge ignites during the negative-going cycles. [Benard et al., 2013] states that distribution of positive ions above dielectric material and hence insulated electrode actively affects propagation of streamer discharge.
According to authors *"the streamers consist of quasi-neutral plasma columns formed along the edge of the air exposed electrode, these columns exhibiting a non-neutral head and propagating along the dielectric surface in branches with curved path lines probably because of strong deformation of the electric field at the dielectric surface due to residual charge effects"* [Benard et al., 2013]. Formed micro-discharges will be distributed stochastically along the edge, with a lifetime in order of nanoseconds and propagation velocity from 10^{-4} to 10^{-5} ms^{-1} [Benard et al., 2013]. According to author: *"during the negative going-cycle, the discharge produces electrons that propagate away from the electron-emitting electrode towards the dielectric surface, while positive ions are attracted"* [Benard et al., 2013]. After this, a diffuse cloud is formed on top of dielectric surface, while the discharge is at glow and emitting light. After cloud formation, electrons tend to accumulate and by doing so they shield the electric field not allowing streamers to appear when AC voltage is applied. *"Unlike electrons, ions stay longer in the vicinity of the electrode due to their mass and thus, a high-density region extends above the surface in which the electric field is high"* [Benard et al., 2013].

In their experiment, [Benard and Moreau, 2014] found that streamer discharge, occurring due to streamer propagation, is characterized by high current pulses, up to 250 mA, while glow-like discharge is characterized by much weaker pulses, up to 10 mA. Hence, it can be concluded that during glow-like discharge velocity of the ionic wind will be higher. This is based on the fact that power consumption will be lower and more electrical energy can be used in transferring momentum from charged particles to neutral particles [Benard and Moreau, 2014]. So both streamer and glow periods will occur once during one AC cycle. As discharge will progress through cycles one can safely observe that there will be fluctuations in the discharge of DBD actuators and thus the force and ionic wind velocity. These two aspects are going to be covered in next two sections of this chapter.

2.2.2 Electrohydrodynamic force

As stated before, EHD force is a product of transfer of momentum that occur between ionized and neutral particles present in the atmosphere [Balcon et al., 2009]. A more elaborate reason for creation of EHD force was given by [Boeuf et al., 2009]. In this research authors state that EHD force created by a surface DBD plasma actuators is due to momentum transfer from ions to neutral molecules in unipolar regions of the discharge [Boeuf et al., 2009]. By unipolar authors mean regions where a positive or a negative, non-neutral ion cloud develops above the dielectric surface. They also state that the momentum transfer takes place mainly during the low current phases between high current pulses, and that the streamers developing along the surface do not contribute significantly to the total EHD force. There are many models, which aim in calculating EHD force. Each of them uses specific assumptions and have different final equations. The most interesting and used models are going to be presented in next few paragraphs.
[Kriegseis et al., 2012] set up an experimental study using Particle Image Velocimetry (PIV)-based estimations to: 1) compute exchange of momentum between plasma and surrounding air; and 2) to estimate EHD force created by DBD plasma actuator. Authors found four cases using integral method and another two

cases using differential method. They state that: *"all implemented integral methods originate from the momentum balance equation* [Kriegseis et al., 2012]. Control volumes used for force estimations are depicted in Figure 2.10.

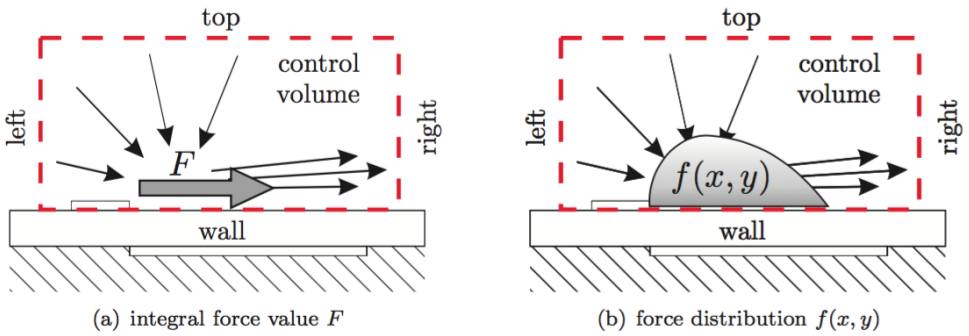

(a) integral force value F (b) force distribution $f(x, y)$

Figure 2.10: Control volumes used for (a) integral force value and (b) force distribution as defined by [Kriegseis et al., 2012]

According to [Kriegseis et al., 2012] Equation 2.4 reduces to Equation 2.5 when one assumes incompressible 2D, steady flow and assumes that there will be no contribution from $\vec{t}$-integral on any of the outer control volume surfaces.

$$\frac{D}{Dt}\iiint_{V(t))} \rho\vec{u}\,dV = \iiint_{V} \rho\vec{k}\,dV + \iint_{S} \vec{t}\,dS \tag{2.4}$$

$$F = \rho\int_{right} u^2dy - \rho\int_{left} u^2dy + \rho\int_{top} uvdx + \int_{wall} \tau_w dx \tag{2.5}$$

However, depending on the available measurement equipment further simplifications may be required such that certain right-hand side terms of Equation 2.5 are neglected [Kriegseis et al., 2012].
Four cases presented in this paper are from four different researchers. Their names and correspond research papers can be found in the original paper. Equations and their brief explanations are going to be presented in following lines.
First case takes into account all four integral parts: right, left, top and wall (bottom). Author that made this equation based it on no-slip wall condition. Meaning that wall part of integral was computed in such a way that shear stress was calculated with first measured velocity above the surface. This case is presented in Equation 2.6.

$$F = \rho\int_{right} u^2dy - \rho\int_{left} u^2dy + \rho\int_{top} uvdx + \mu\int_{wall} \frac{\Delta u}{\Delta y}|_{1.IA}dx \tag{2.6}$$

Next case made by another author does not take into account the shear element of the integral Equation 2.5, meaning that it only computes the momentum flux crossing control volume boundaries. It will consist out of right, left and top part and is presented in Equation 2.7. One note that should be made, is that this equation is representing a net force as the shear or friction force is taken out.

$$F = \rho\int_{right} u^2dy - \rho\int_{left} u^2dy + \rho\int_{top} uvdx \tag{2.7}$$

If flow is stationary or quiescent one may use third case. Here author assumed that flux over all boundaries except the right one is negligible. With this assumption Equation 2.8 was made.

$$F = \rho \int_{right} u^2 dy \tag{2.8}$$

Last case of the integral method summarized by [Kriegseis et al., 2012] assumes that the airflow at left boundary is unaffected by the actuator thus only this term is going to be left out of the Equation 2.5.

$$F = \rho \int_{right} u^2 dy + \rho \int_{top} uv dx + \int_{wall} \tau_w dx \tag{2.9}$$

At this point summarizing of integral method cases is covered and two cases which use differential method can be presented. Fifth case is based on the Navier-Stokes equations. It assumes that pressure gradients inside the system are neglected. Remaining unknowns are forces in x and y direction, and because there are two equations, this makes a system of two equations and two unknowns. Force in x-direction can be computed using Equation 2.10. Force in y-direction is found in analogous way.

$$f_x(x,y) = \rho \left(u\frac{\partial u}{\partial x} + v\frac{\partial u}{\partial y} \right) - \eta \left(\frac{\partial^2 u}{\partial x^2} + \frac{\partial^2 u}{\partial y^2} \right) \tag{2.10}$$

Last case is as well computed using differential method but instead of being based on Navier-Stokes equation, its foundation comes from vorticity equation. This case is based on two assumptions. It assumes no pressure gradients inside the control volume, and makes an assumption that curl of the force is strongly dominated by $\partial f_x / \partial y$. This means that:

$$\frac{\partial f_x}{\partial y} \gg \frac{\partial f_y}{\partial x} \tag{2.11}$$

This leads to the Equation 2.12, which corresponds to the case 6 from [Kriegseis et al., 2012] research.

$$f_x(x,y) = -\rho \int_{\infty}^{0} \left[u\frac{\partial \omega}{\partial x} + v\frac{\partial \omega}{\partial y} - \frac{\eta}{\rho} \left(\frac{\partial^2 \omega}{\partial x^2} + \frac{\partial^2 \omega}{\partial y^2} \right) \right] dy \tag{2.12}$$

According to [Benard et al., 2013] negative-going and positive-going cycles produce different electric wind velocities. These velocity fluctuations during one AC period also cause the difference in gas flow production. Authors confirm that *"during a period with a positive-going voltage, no significant pressure change was observed, while a period of negative-going voltage promotes a clear jump in pressure. This suggests that the body force is only produced during the negative-going voltage half cycle"* [Benard et al., 2013]. The difference in gas flow production hints that higher force production will be during negative-going half of AC voltage cycle. Even though the force produced during a two halves of the AC cycle is not the same in magnitude, [Enloe et al., 2009] found out that they will be induced in the same direction. They also found out that the positive-going force will not be able to overcome drag in the close proximity of the actuator wall due to lack of momentum.

"Force calculation based on the integral methods has demonstrated good results with calculated mean forces in agreement with direct load measurements. If the same methodology is applied to time-resolved measurements, than a time evolution of the total force integrated over a spatial domain should be obtained" [Debien et al., 2012]. This means that positive EHD force will occur during a positive-going cycle, while

the negative EHD force will occur during a negative going cycle. [Debien et al., 2012] results for plate-to-plate configuration are presented in Figure 2.11. Figure 2.11 shows positive (283 mN/m) and negative (-219 mN/m) forces during two halves of the cycle. This is in contradiction to what [Enloe et al., 2009] have said and requires further discussion.

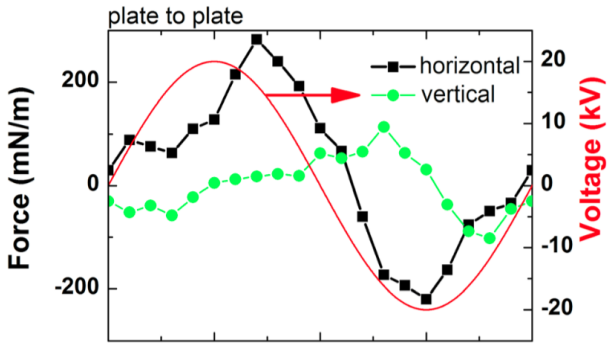

Figure 2.11: EHD force versus time as defined by [Debien et al., 2012]

Due to this contradiction [Benard et al., 2013] conducted a research to find spatial and temporal evolutions of the volume force. Their investigation confirmed [Enloe et al., 2009] findings that the glow regime is responsible for a large positive volume force, while the streamer regime also produces a positive force whose amplitude is highly reduced. [Benard et al., 2013] results can be seen in figures 2.12 and 2.13.

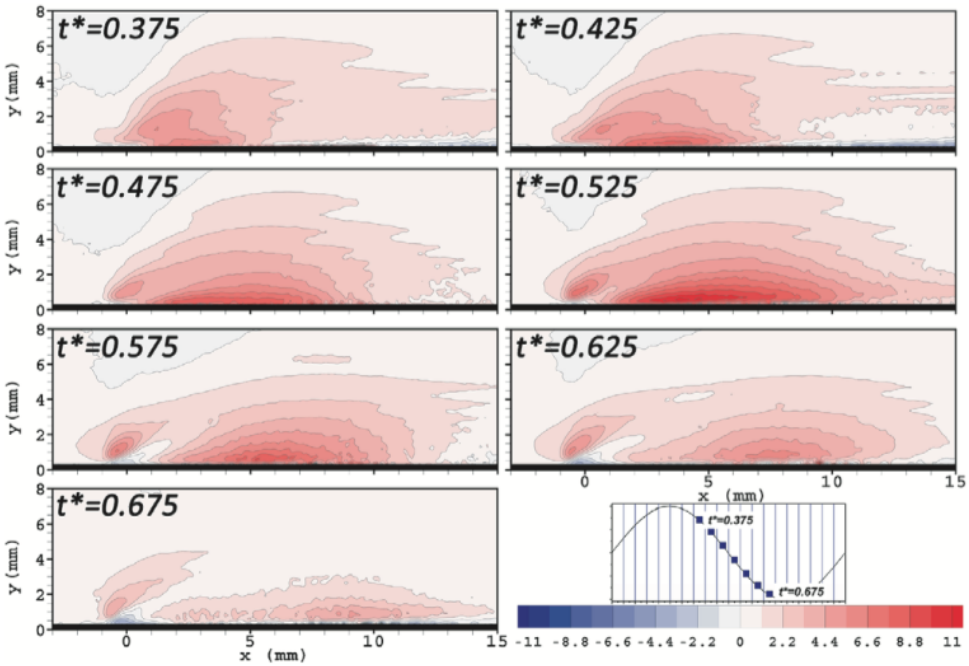

Figure 2.12: *"Spatial distribution of the electrohydrodynamic volume force $f_x(\boldsymbol{x},t)$, forms during the period of glow regime. Scale is given in $x10^{-3}$ Nm^{-3} "*[Benard et al., 2013]

Figure 2.12 shows the production of positive volume force during the glow regime. If one observes temporal changes in force intensity it can be seen that the strongest force is produced in the middle of the glow period.

[Benard and Moreau, 2014] state that positive volume force in streamer propagation region is due to positive going cycle presented in Figure 2.13. This can be seen in the left two parts of figure below. Authors also state that when compared to glow period produced force, this will be very weak, as it was stated before by [Enloe et al., 2009].

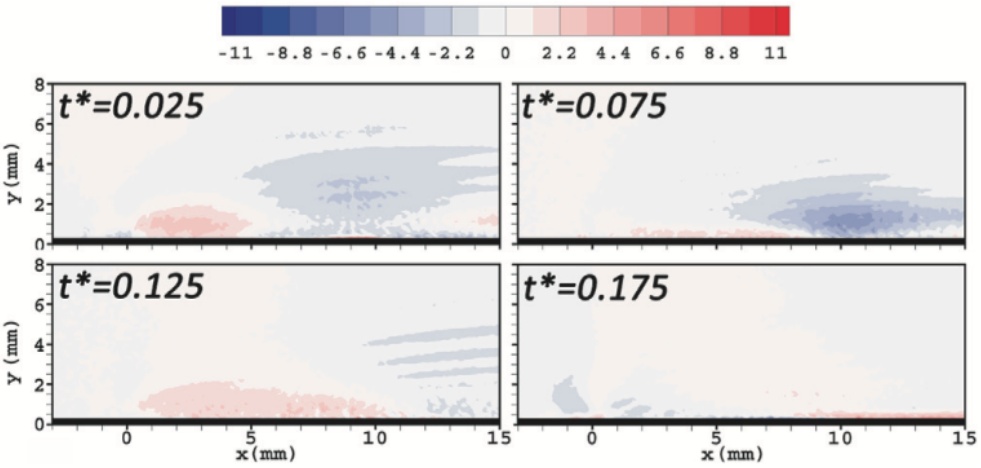

Figure 2.13: *"Spatial distribution of the electrohydrodynamic volume force $f_x(\boldsymbol{x},t)$, forms during the period of streamer regime. Scale is given in $x10^{-3}$ Nm^{-3}"*[Benard et al., 2013]

In order to validate above stated, another research had to be found. [Boeuf et al., 2009] computed out three important features of the EHD force produced by AC DBD actuators. First found feature backs up [Enloe et al., 2009] statement. Authors say that the direction of EHD force along the surface does not depend on sinusoidal cycle phase (positive or negative). Second feature that [Boeuf et al., 2009] found was that there is a large negative force (directed toward the top electrode) that is localized in a very small region next tot the top electrode during the negative part of the cycle. By stating this authors came to the same results as ones found in [Benard et al., 2013] research. Third found feature is that the EHD force has different spatial distribution depending on cycle phase: the force due to negative ions in the negative phase is distributed rather smoothly and uniformly, over a length of about 5 mm along the dielectric surface, while the force due to positive ions, in the positive phase of the cycle, is distributed non-uniformly, closer to top electrode. There is no force during high current pulses since the EHD force is quasi-zero in a quasi-neutral plasma (the channel of streamers) [Boeuf et al., 2009].
Last paragraph in this section will present some EHD force conclusions made by various research:

- *"It is demonstrated that intensity as well as the domain of force increases with increasing operating voltage. It is shown that 30% of the overall induced momentum is consumed by wall friction"* [Kriegseis et al., 2012]
- *"Discharge efficiency to produce EHD force is less than 1 mN/W. For a given frequency, the efficiency in production of the EHD force strongly decreases with voltage amplitude above a given voltage (because more energy is spent in streamer discharges at higher voltage). The calculated efficiency at the maximum force is on the order of 0.2 mN/W, and this is consistent with the measurements"* [Boeuf et al., 2009]
- *"When the plasma force is deposited closer to the surface, wall drag increases resulting in less net force imparted to the air"* [Font et al., 2009]

- *"Force imparted by the plasma over a large volume should result in lower drag losses if the increase in plasma volume is away from the surface"* [Font et al., 2009]
- *"Actuator power consumption does not change significantly as different external flow speeds are applied, both in the counter-flow and co-flow DBD configurations"* [Pereira et al., 2014]

2.2.3 Electric wind

Similarly to the EHD force, electric wind is also produced by momentum transfer between ionized and neutral particles. [Balcon et al., 2009] in their research aimed in investigating electric wind formation in quiescent air over time using PIV measurements. One of the results obtained during this research is presented in Figure 2.14. Left column of this figure represents the beginning of excitation right after 2 ms. One can observe start of counter-clockwise rotating vortex situated right at the left side of an electrode (x=0 mm). The induced electric wind positioned at 1 mm above the edge of grounded electrode, with a maximum velocity of 0.4 m/s is directed downward. According to the author *"this indicates that air acts as a low pass filter for the momentum transfer occurring in the discharge region and consequently wall jet formation is not as fast as electric discharge ignition"* [Balcon et al., 2009].
From Figure 2.14 it can be seen that after 25 ms and 50 ms it is possible to evaluate convecting velocity of the vortex at approximately 0.6 m/s. Also after 50 ms it can observed that the main flow is more parallel to the wall with a greater maximum velocity of about 2.4 m/s located 10 mm beyond the edge of active electrode. *"After this point, the induced flow is still detached from the wall due to pressure gradients near the wall surface an to the vortex sense of rotation"* [Balcon et al., 2009].
After 100 ms one can observe that there is no more vortex. Here the flow is convected to the main airflow stream. At 400 ms one can no more see the evolution of the flow. The only assumption that can be made here is that the flow reached the steady-state. As the frequency applied in this experiment was 1 kHz, [Balcon et al., 2009] state that the steady-state period of 400ms corresponds to 400 periods of AC cycling.

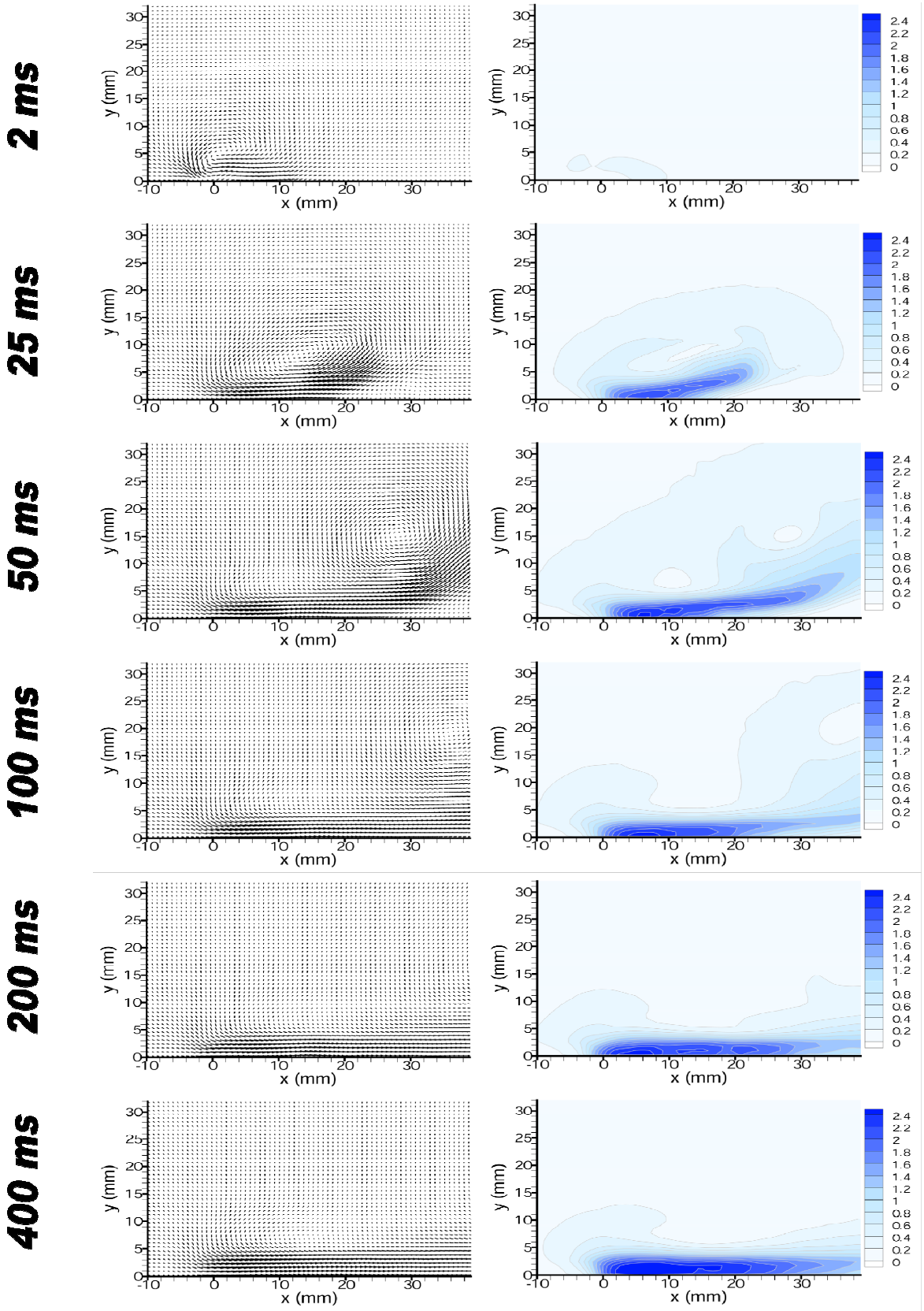

Figure 2.14: Velocity vector field and norm (m/s) for actuation times ranging from 2 ms to 400 ms [Balcon et al., 2009]

In their research [Balcon et al., 2009] made velocity profiles as a function of distance to the surface for two x positions away from the active electrode. These profiles are presented in Figure 2.15.

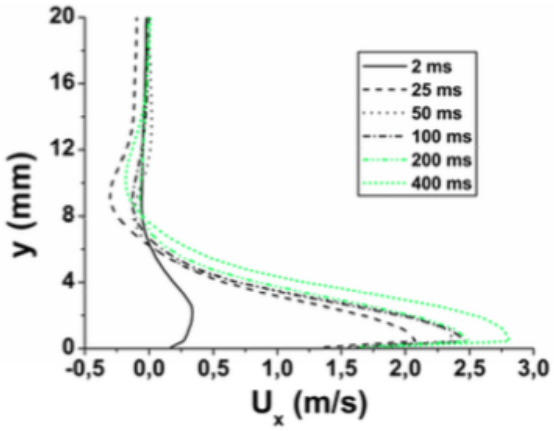

(a) Velocity profiles at x=5 mm for actuation times from 2 to 400 ms

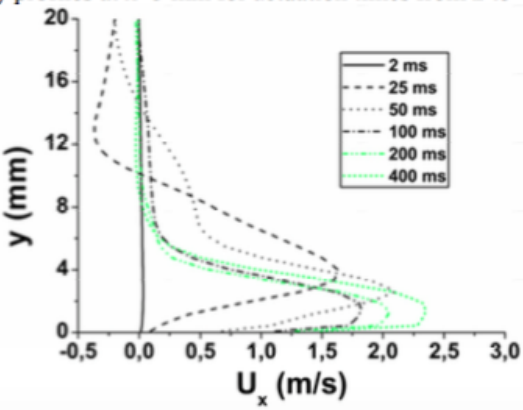

(b) Velocity profiles at x=20 mm for actuation times from 2 to 400 ms

Figure 2.15: Vertical velocity profiles for different actuation times [Balcon et al., 2009]

If one observes Figure 2.15, it can be seen that at 5 mm from the edge of the air exposed electrode velocity becomes nearly constant after 25 ms. It can be concluded that with increasing actuation time so does the flow velocity as the figure clearly shows that the highest velocity of about 2.7 m/s is obtained after 400 ms. Authors state *"that for the actuation times longer than 400 ms the shape of the velocity stays unchanged and the maximum velocity remains 2.7 m/s"* [Balcon et al., 2009]. Bottom part of Figure 2.15 shows the velocity profile at the end of the grounded electrode. At this point the differences between velocities at different actuation times is more clear. One can observe again the same trend that with longer actuation times there are higher velocities with one anomaly. This anomaly is that the velocity profile for 100 ms is lower than profile obtained at 50 ms. According to the author main reason behind this anomaly are strong viscous forces very close to dielectric surface [Balcon et al., 2009].

Mass flow rate of the single dielectric barrier discharge can be found using Equation 2.13.

$$Q = \rho L \int_0^\infty u(y) \partial y \tag{2.13}$$

Where L is the electrode length, or the size of the electrode perpendicular to the induced flow direction and

ρ is the fluid density. Authors came to the conclusion that *"for all positions, the flow rate increases with the actuation time in a non-linear fashion"* [Balcon et al., 2009].
Authors found one more interesting conclusion. Namely *"the maximum velocity is always located between the edges of the electrode pair where the electrical discharge occurs. The momentum transfer between charged and neutral particles taking place only in this region it is consistent that no flow acceleration is measured downstream"* [Balcon et al., 2009].
Last part of this section is going to deal with the efficiency of DBD plasma actuators. Under the assumption that the flow is quiescent, efficiency can be computed using the Equation 2.14.

$$\eta = \frac{P_{mechanical}}{P_{electrical}} \tag{2.14}$$

To find the mechanical power [Benard and Moreau, 2014] assume that the mechanical power corresponds to the kinetic energy density flow rate which can be expressed by Equation 2.15.

$$P_{mechanical} = \frac{1}{2}\rho_G L \int_0^\infty U^3(y)dy \tag{2.15}$$

[Benard and Moreau, 2014] made several remarks concerning efficiency of DBD plasma actuators where the grounded electrode was not encapsulated:

- The efficiency value is very low, it increases with dielectric thickness
- The efficiency increases for power consumption up to about 1.5 W/cm, after which it decreases
- Even though plasma actuator efficiency is very low, the effectiveness for flow control can be excellent

Literature study of this thesis found only one paper dealing with DBD plasma actuator operation in the low pressure environment. Paper was made by [Benard et al., 2008a], and it studies DBD plasma actuator's ability to produce electric wind in various pressure environments with lowest of 0.2 atm. According to Figure 4.6, 0.2 atm corresponds to geometrical altitude of 12 km.

Figure 2.16 shows power consumption per unit length of DBD actuator as a function of atmospheric pressure.

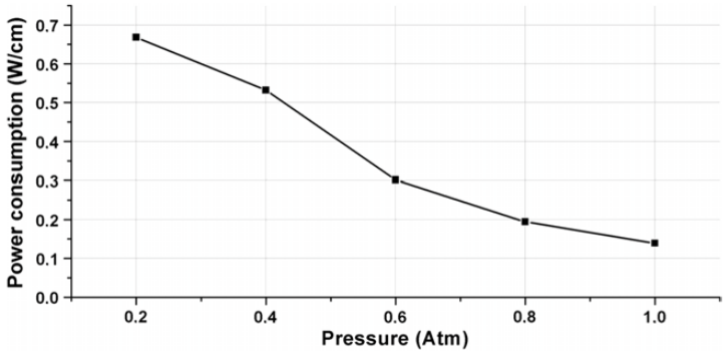

Figure 2.16: Electrical power consumption per unit length of DBD actuator (values time-averaged over 100 cycles) [Benard et al., 2008a]

Figure 2.16 shows an increase in power consumption with a decrease in pressure. This is due tot the fact that in low pressure environment, micro-discharges are created more often when voltage is kept constant.

According to the author, when the gas density is reduced, current pulses become more intense as the electric field is kept constant resulting in less collisions between ions and neutral particles. [Benard et al., 2008a] also found out that the plasma extension is linearly related to the electrical power consumption. This statement was proven in Figure 2.17.

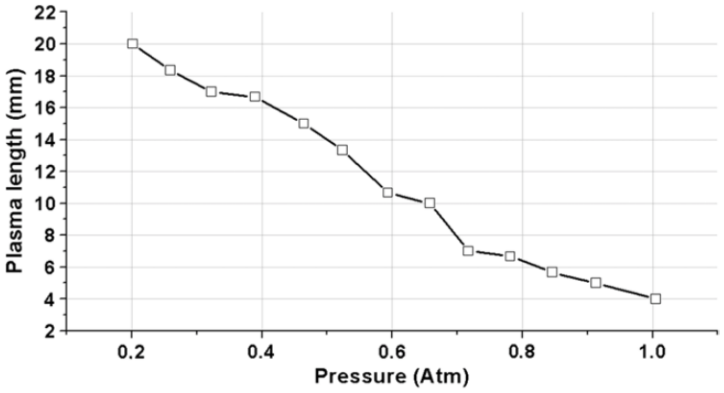

Figure 2.17: Plasma extension [Benard et al., 2008a]

Last finding of [Benard et al., 2008a] is that the shape of the velocity profile (in the direction away from the surface) is not dependent on the ambient pressure levels. However, velocity profiles show a shift in the direction of the electric wind when pressure is reduced. Concerning the magnitude of the electric wind, authors found out that it is greatly modified with pressure changes. They found that the maximum velocity obtained for a surface DBD actuator increases with the decrease of atmospheric pressure.

3 DBD ACTUATORS IN HIGH MACH NUMBER FLOW FIELD

Nowadays many research teams work with various plasma actuator types applied from quiescent to transonic airflow conditions, but wide research gap in supersonic and hypersonic flows exist [Bletzinger et al., 2005]. As the aim of this Master's thesis is to explore possibility of using plasma actuators (with main focus on the DBD actuator type) in space-based system, one has to provide insight of their use in flow fields characterized by high Mach numbers, experienced during launch and re-entry mission phases. If the flow is classified according to the Mach number, it can be divided into six categories: subsonic (M<0.8), transonic (0.8<M<1.2), sonic (M = 1), supersonic (1.2<M<5), hypersonic (5<M<10) and high-hypersonic (M>10). Following sections present literature covering plasma actuator operation in transonic, supersonic and hypersonic flows.

3.1 Transonic Flow

Before one dives into supersonic and hypersonic airflows, it is helpful to mention some research that was done at transonic speeds. [Pavon et al., 2007] conducted study where authors demonstrated that DBD can be sustained in transonic airflows, up to isentropic Mach numbers (M_{is}) of 1.1. At isentropic Mach number of 0.7 he explains the phenomenon behind an increase in breakdown voltage with an increase of airflow velocity. Author found out that the dominant cause for the breakdown voltage increase is the depletion of metastable states. Second finding of this research was that when the frequency is decreased, the breakdown voltage will increase. Reason behind this is that when frequency is lowered, there will be fewer number of metastable molecules, which in fact means that energy level is decreased; meaning an increase in breakdown voltage. Discharge breakdown voltage as a function of Mach number is presented in Figure 3.1.

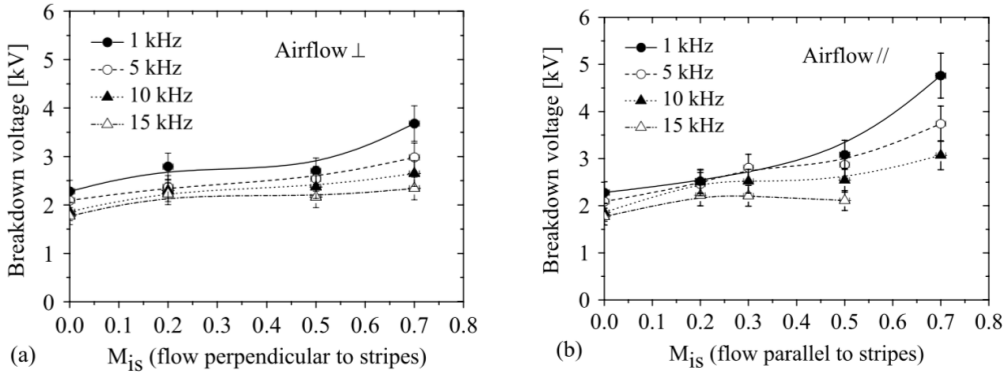

(a) (b)

Figure 3.1: Discharge breakdown voltages for an airflow perpendicular (a) and parallel (b) to the electrode stripes [Pavon et al., 2007]

Figure 3.1 gives a first hint why use of DBD actuators for space-based system could present as a difficulty.

Namely for all tested frequencies there is an increase in breakdown voltage with increase of Mach number. Higher breakdown voltage results in higher power consumption, which is limited for all space-based systems by battery mass and size of solar panels.

3.2 Supersonic Flow

When plasma actuators are operated in supersonic flow fields, two flow related phenomena can be modified. Boundary layer manipulation is first and second phenomenon is shock wave modification. Changes in boundary layer are interesting for this thesis because they could be introduced using DBD plasma actuators, whose power consumption is very low (<10 W) [Im et al., 2010]. This is very desirable in space and aeronautical applications as mass is one of the most critical designing parameters. Boundary layer can be modified in several ways:

- Laminar-to-turbulent transition delay using glow discharge plasma actuators [Grundmann and Tropea, 2007]
- Active vortex generation for aerodynamic flow control [Benard et al., 2008b]
- Separation control [Post and Corke, 2004]; and
- Turbulent boundary layer manipulation [Porter et al., 2007]

Presently many research groups use a high power consumption, DC plasma actuators for various flow control applications. These thermal DC actuators can use from 100 W to about 10000 W, which is much higher than needed for DBD actuator [Im et al., 2010]. Use of the DBD plasma actuator in flows described with high Mach number is very difficult and limited as velocities created with DBD actuator (induced ionic winds) are very small compared to surrounding environmental flow. This does not mean that it is impossible to use this actuator type in supersonic flow. As flow near the surface inside boundary layer is fraction of flow outside of it, one can state that DBDs can introduce a significant perturbation to the boundary layer and in particular the transition from laminar-to-turbulent point [Pal et al., 2012]. One of these researches was done by [Im et al., 2010]. In this paper, authors demonstrate that when DBD plasma actuator is used in M=4.7 flow, the turbulent boundary layer can be reduced while the power consumption is 6.8 W. Visualization of these results was done by use of planar Rayleigh scattering off of condensed CO_2 particles [Im et al., 2010]. These results can be seen in Figure 3.2.

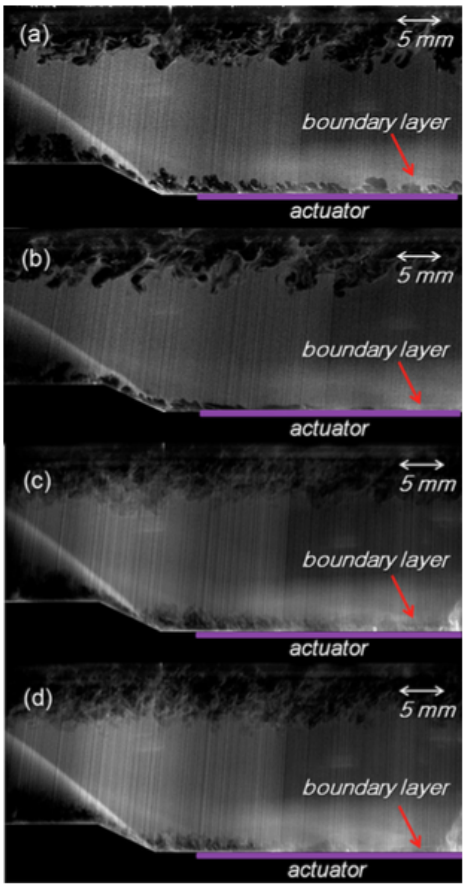

Figure 3.2: Instantaneous CO_2 Rayleigh scattering images (a) plasma off case, (b) plasma on case, averaged images, (c) plasma off case, and (d) plasma on case [Im et al., 2010]

Figure 3.2 shows four cases: (a) and (b) represent instantaneous, while (c) and (d) represented averaged results. (a) and (d) depict cases where plasma actuator is turned-off, while the other two describe flow when actuator is turned-on. In both instantaneous and averaged results, if the height of dark region on the wall is observed and estimated, one can deduce that the thickness of turbulent boundary layer is reduced when DBD plasma actuator is used and discharge is activated. [Im et al., 2010] relate this thinning of the boundary layer to the generation of span-wise flow.

[Bisek et al., 2014] conducted a computational study of a cylinder with DBD actuator under M = 5 airflow. They came to conclusion that when nanosecond pulse driven DBD actuator is attached to cylinder in supersonic flow a strong compression wave can be produced. Compression wave reduces total drag at expense of increased peak surface heating. Authors also found that DBD actuator could not be used to improve the cylinder's surface conditions, but it showed up to be very effective at moving a strong standing, wave with low power consumption.
From the same research group came paper made in 2011 by [Nishihara et al., 2011]. They showed a Mach 5 bow shock perturbations introduced by surface DBD plasma actuator. One of the main reasons why DBD actuator is not extensively researched in high Mach number flow fields is that EHD effect is most significant in free stream flows of about 10 m/s. Authors state that *"the main problem of DBD actuator type when*

used at supersonic, and hypersonic velocities is to sustain high space charge density and high electric field in the discharge" [Nishihara et al., 2011]. This is the reason why actuator was positioned very close to the stagnation point (point in which proximity, flow velocity is zero or very close to zero). When considering actuator location, two cases tested. First where an actuator was positioned symmetrical with respect to a stagnation point and second where actuator's edge is positioned at the flow stagnation point.

Perturbations caused by actuator made a compression wave, that travelled upstream towards baseline bow shock naturally created by a cylinder in supersonic flow. When compression wave collides into bow shock, it also displace it in the upstream direction, increasing stand-off distance by up to a quarter of its original value, and bend it away from the cylinder model [Nishihara et al., 2011]. This interaction can be seen in Figure 3.3 that depicts the difference of Schlieren signal intensity from the baseline Schlieren signal, when actuator is operated in two-pulse burst mode at 100 kHz pulse repetition rate and 200 Hz burst repetition rate.

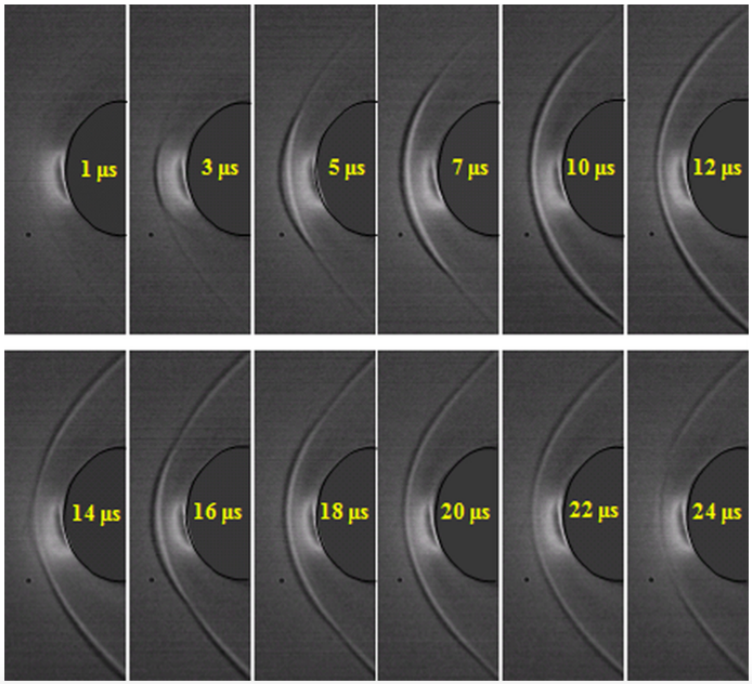

Figure 3.3: Difference of Schlieren signal intensity from the baseline Schlieren signal [Nishihara et al., 2011]

First pulse is generated at 0 μs and the other at 10 μs. From Figure 3.3 bow shock stand-off distance peaks approximately at 5 μs and at 14 μs. According to the authors reason behind the generation of compression wave in surface DBD plasma actuator is energy thermalization or localized heating. This statement was based on research conducted by [Popov, 2001], but [Nishihara et al., 2011] could not fully understand detailed kinetic mechanism of this process in broad range of reduced electric fields.

Interaction between baseline shock wave and compression wave generated under conditions same as in Figure 3.3 can be seen more clearly in Figure 3.4. Here we can see time evolution of compression shock, up about 3 μs where it interacts and moves the baseline shock away from its neutral position.

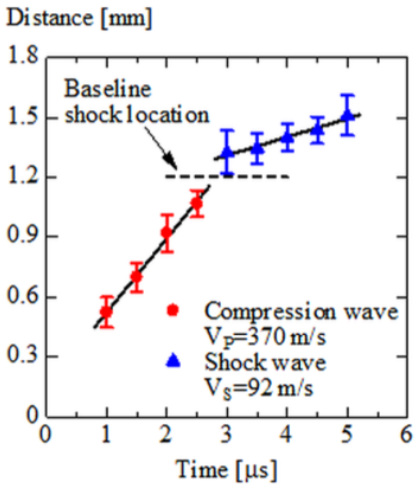

Figure 3.4: Time evolution of compression wave and perturbed bow shock location along the stagnation streamline [Nishihara et al., 2011]

[Nishihara et al., 2011] computed the relative change in shock stand-off distance when actuator is operated in burst mode. This is presented in Figure 3.5. In both figures error bars were computed from intensity peak Full Width at Half Maximum (FWHM).

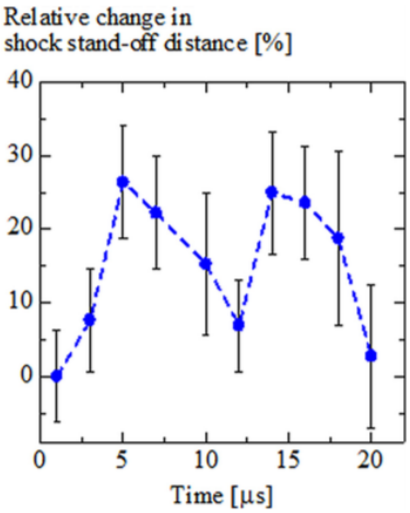

Figure 3.5: Percentage increase of the shock stand-off distance after the first and the second discharges pulses [Nishihara et al., 2011]

According to authors, *"possible uses of this method could be modulation of supersonic laminar to turbulence transition, control of shear layer instability or control of shock-shock and shock-boundary layer interaction"* [Nishihara et al., 2011]. This opens opportunity to design a control system for space-based vehicle traveling at M=5.

3.3 Hypersonic Flow

Plasma discharge is characterized by the regions of high temperature in the field. When hypersonic flow, which is characterized with high kinetic energy, collides with ionized regions, there might occur an energy interaction [Sriram et al., 2012]. Knowing that flow velocity has consequential influence on plasma characteristics created by DBD actuator, and the above mentioned energy interaction make DBD actuator difficult to model, test and build in these flow conditions [Pavon et al., 2007]. One of the main problems associated with hypersonic flight is the alteration of chemical and thermal properties of air. Atoms and molecules composing air mixture, mentioned in Chapter 4 under certain temperature will break bond, recombine and ionize. Enormous increase in temperature comes from high kinetic energy that is transferred to thermal energy at the surface of flying vehicle. According to [Atkinson, 2012] following events will occur at certain temperatures:

- 2000 K $\rightarrow$ O_2 begins to dissociate
- 4000 K $\rightarrow$ N_2 begins to dissociate
- 5000 K $\rightarrow$ Air begins to ionize
- 6000 K $\rightarrow$ O_2 is completely dissociated
- 7000 K $\rightarrow$ N and O start to ionize
- 9000 K $\rightarrow$ N_2 is completely dissociated
- 10000 K $\rightarrow$ Ar starts to ionize

[Sriram et al., 2012] conducted a study where DBD plasma actuator was placed inside hypersonic flow made by two gases. First gas used was Air, characterized with M = 6.25 flow velocity, while the second gas was Argon, characterized with M = 9.07 flow velocity. Two actuators, one 15 mm long and other 5 mm long were placed inside flows to investigated the effect of actuator length. Third investigated variable was plasma pulsing frequency by applying 8 kHz and 19 kHz to the longer actuator.

Authors concluded that in presence of DBD actuator surface pressure on top of a flat plate significantly changes. When actuator is turned on the frequency applied to it will also vary the measured pressure. This can be seen in Figure 3.6. Another conclusion that [Sriram et al., 2012] found is that considering measurements obtained during their research, authors are not able to provide any information about the general trend and phenomenology involved. Knowing this along with unavailability of papers concerning DBD actuators and high Mach number flow conditions, it is required to perform additional research to characterize and optimize DBD actuators in these conditions.

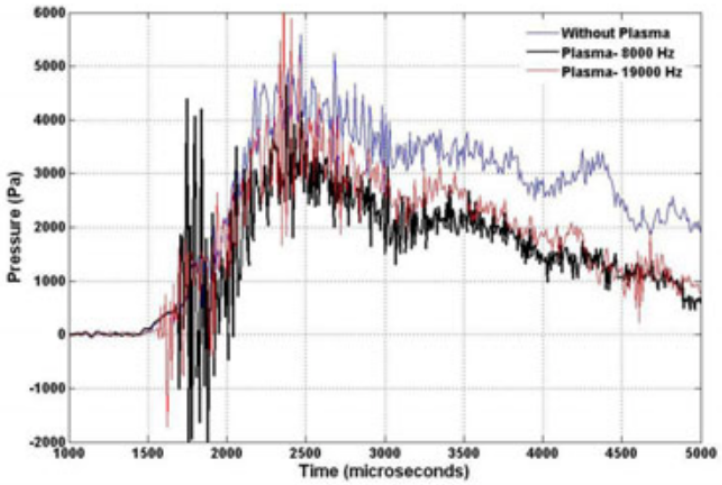

Figure 3.6: Surface Pressure signals in sensor 3 in the centre array with and without plasma, with actuator of 15mm length, with air as test gas [Sriram et al., 2012]

Following few paragraphs will present another research, parametric study that depicts use of micro-second pulse surface DBD actuators for net heat flux reduction on cylindrical body placed in re-entry hypersonic flow at Mach number of 17 [Bhatia et al., 2014]. This research consists of two simulations. First simulation models the effect of DBD actuators on viscous perfect gas hypersonic flows, that assume thermochemical equilibrium, and the other models actuator's effect on thermochemical non-equilibrium hypersonic flow. In introduction of this research authors mention research conducted by Nishihara and its team. As earlier stated, [Nishihara et al., 2011] used nanosecond DBD actuators for increase of shock stand-off distance. By doing so an advantage of heat loss due increased shock distance is compensated by net heat added to the complete system. Therefore the steering of vehicle in M = 5 flow using DBD plasma actuator comes at a cost of an increased heat during its duty cycle [Bhatia et al., 2014]. This might not be a critical problem for vehicles flying at supersonic velocities but, it definitely is for vehicles subjected to hypersonic flows. Due to this reason authors positioned actuators near the stagnation line in three different orientations in order to use induced ionic wind in order to release some of the heat accumulated at surface of the cylinder. Actuator positions and induced EHD force directions can be seen in Figure 3.7. It should be noted that Mach 17 free-stream vector is directed from left to right.

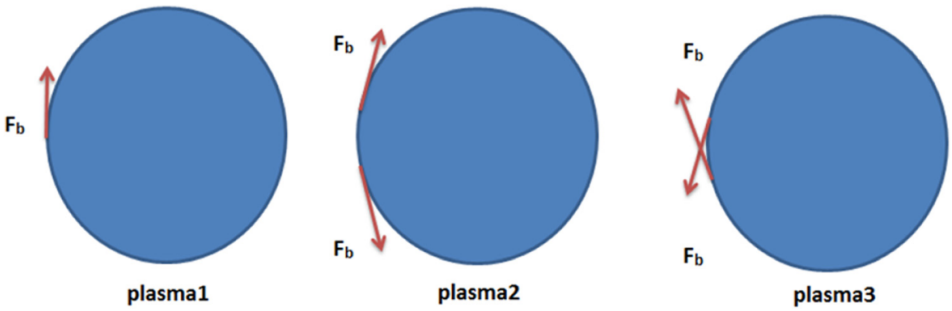

Figure 3.7: Three configurations for DBD plasma actuators[Bhatia et al., 2014]

In Figure 3.7, first configuration (plasma1), is made of one actuator positioned at stagnation point with flow forcing in upward direction. Second and third configurations consist of two actuators positioned 25 mm above and below stagnation point. Difference between plasma2 and plasma3 configurations is the direction of actuator forcing. In plasma2 configuration DBD actuators are forcing away from each other, while in other setup actuators are forcing towards each other, toward stagnation point. For non-equilibrium flow, this research assumes air composition made ou of only two di-atomic molecules, namely mixture of 75.62% N_2 and 24.38% O_2.

The effect of plasma actuation on viscous hypersonic flow can be seen in Figure 3.8. Here one can see thermal heat transfer coefficient as a function of different radial positions along the cylinder, where zero is marking a stagnation point perpendicular to free-stream flow. Surface heat transfer coefficient is computed using equation below:

$$C_h = \frac{q_w}{\frac{1}{2}\rho_\infty U_\infty} \tag{3.1}$$

Where q_w is the net heat flux impinging wall in perpendicular direction. The right part of Figure 3.8 shows the zoomed-in part of the full plot showed in left part. When compared all three configurations one can clearly see that the highest heat flux reduction is achieved with plasma3 configuration where forcing is directed towards stagnation line.

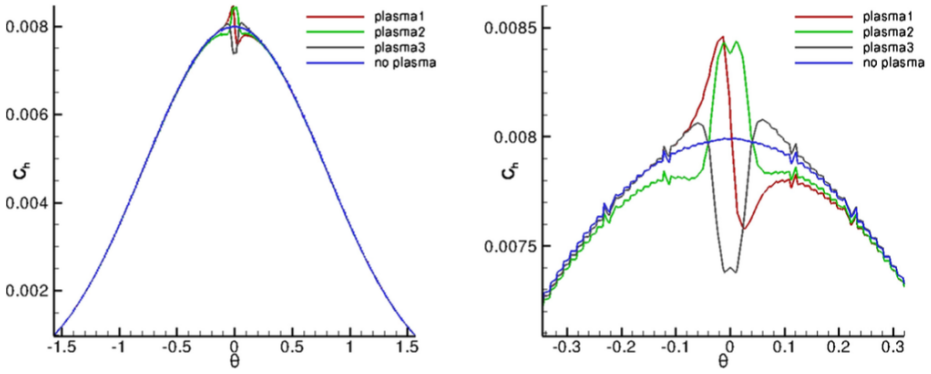

Figure 3.8: Effect of plasma actuation on the surface heat transfer coefficient, C_h of hypersonic flow over cylinder [Bhatia et al., 2014]

To understand how plasma actuator is influencing the flow physics, velocity and temperature profiles near stagnation point authors make a series of plots, presented in Figure 3.9. Figure below has four parts: top left represents nominal case without plasma actuation; top right represents case of plasma1 configuration; bottom left represents plasma2 configuration; and bottom right represents plasma3 configuration. If top left part of a Figure 3.9 is compared to top right part, it can be stated that plasma1 is capable of "pushing" temperature contour lines away from the stagnation point, thus reducing heat flux impinging actuator's surface (about 25 mm downstream from stagnation point). This proves that with use of one plasma actuator beneficial heat reduction effects can be obtained near stagnation point and inside boundary layer, even when actuator is placed in hypersonic flow field. Similarly to plasma1 configuration, plasma3 case also "pushes" temperature contours away from the cylinder surface causing overall reduction in heat flux. However plasma2 configuration is somewhat different as it "pulls-in" contours in range of -50 mm <y< 50 mm and "pushes" them for the rest of modelled region. Reduction of temperature occurs as actuator is inducing a flow in close proximity of the stagnation point. At stagnation point the value of heat flux is the greatest as flow comes to

rest, thus complete kinetic energy is transferred into thermal energy. When flow is introduced it causes shift of the point where flow velocity is zero away from stagnation line in direction of induced flow. To represent change in flow velocity when plasma actuators are used, authors plot velocity profiles for all cases. These are presented in Figure 3.10

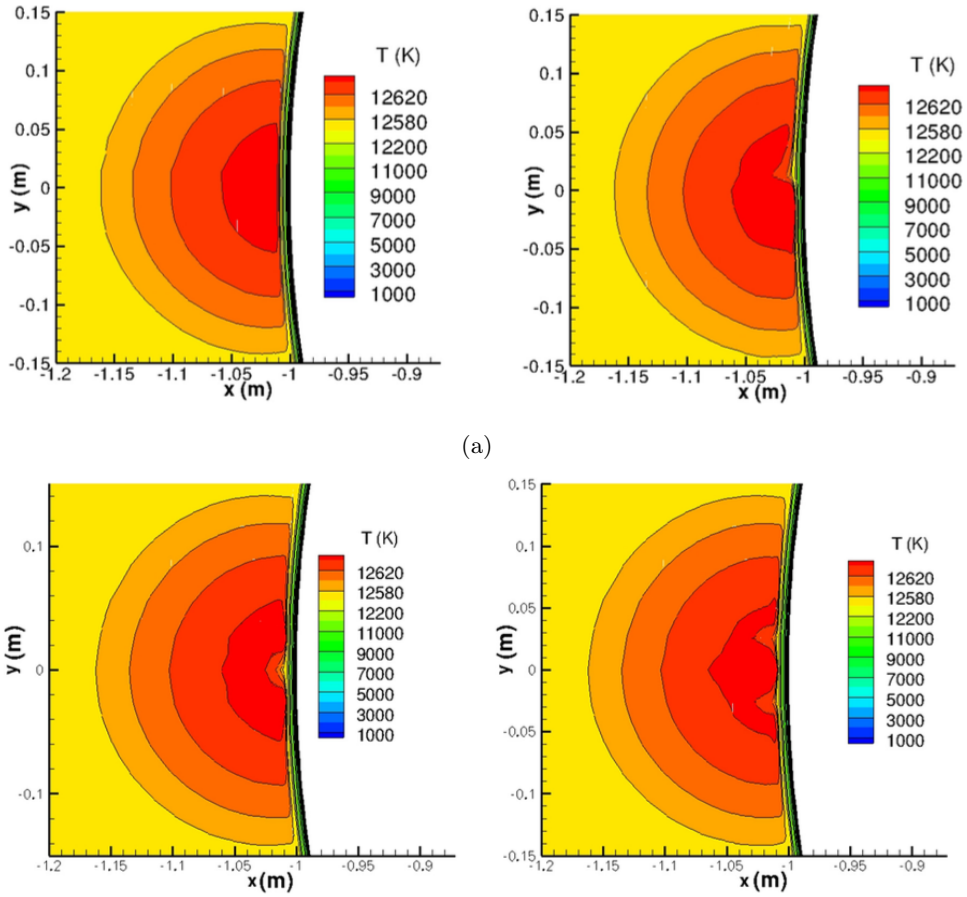

Figure 3.9: Temperature profiles in proximity to the stagnation point with no and three configurations with DBD plasma actuators [Bhatia et al., 2014]

Top part of Figure 3.10 depicts comparison between plasma1 with no-plasma nominal case. Subplot (b) represents comparison between plasma2 and no-plasma case, and subplot (c) shows comparison between plasma3 and no-plasma configurations. It should be noted that in all three subplots fill line represents no-plasma case and dashed lines represent three other configurations respectively. If actuators are positioned similarly to plasma1 or plasma3 cases, induced flow oppose free-stream; and if they are positioned same as for plasma2 case the induced flow will be in the same direction as hypersonic flow. Opposing flow velocity means that the heat flux next to surface will be reduced, meaning lower heat transfer. Adding velocity to the free-stream flow will do the opposite, hence increase the heat flux and temperature at cylinder surface. With all above stated, [Bhatia et al., 2014] came to the conclusion that with use of DBD plasma actuators in plasma3 configuration, also known as a counter-flow moment addition, results in maximum reduction of 7.68% in the stagnation point heat flux.

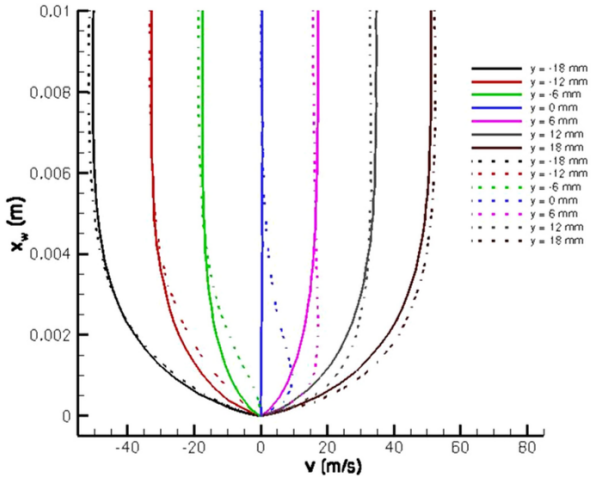

(a)

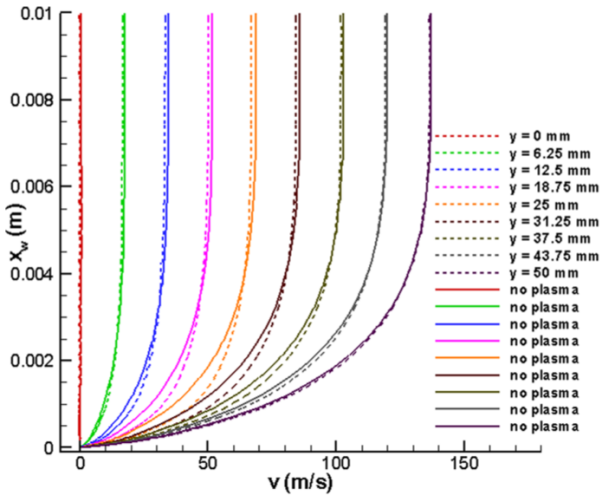

(b)

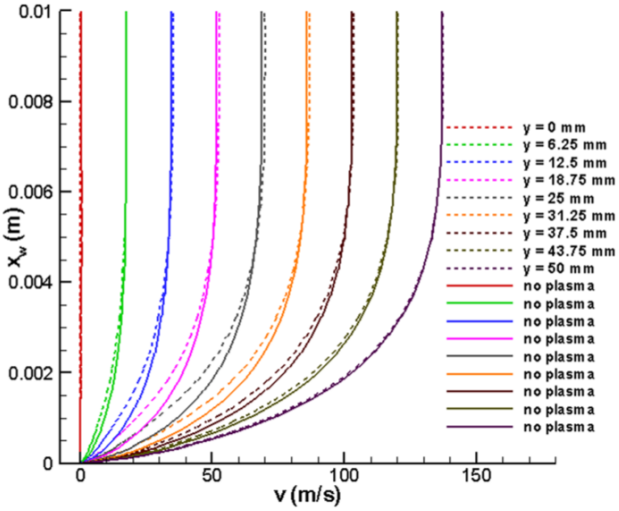

(c)

Figure 3.10: Velocity profiles in the normal direction from the stagnation line for (a) plasma1 (b) plasma2 and (c) plasma3 all against no plasma case [Bhatia et al., 2014]

It should be noted that none of the research presented in Section 3.3 take into account that there exist no dielectric material that can withstand heat loads expected to occur at hypersonic flow velocities. As it was computed by [Bhatia et al., 2014] modelled stagnation point temperatures at M = 17 exceed 12500 K. To my knowledge no dielectric material has higher melting temperature than 2345 K (Aluminium Oxide), which is below the required one. If it is desired to use DBD actuators at hypersonic flow fields, one would have to either develop new dielectric material or use active or passive cooling techniques. This would certainly increase both mass and cost of DBD actuation system, meaning that one would have to conduct cost-benefit analysis before any testing is done. Another promising solution to high temperatures is provided by research group from U.S. Air Force Research Laboratory in Ohio. They conducted a study concerning control of high angle of attack reentry flow with plasma actuators. [Atkinson et al., 2013] developed a phenomenological model that simulates the effect of magnetically accelerated surface discharges on the 2:1 blunt elliptic cone. In order to lower the heat loads on the spacecraft's surface, conical reentry vehicles could come into the atmosphere at high angle of attack. By doing so it increases drag meaning lower velocity and lesser heat loads. Benefit of reduced heat loads is that the overall spacecraft weight can be lowered, as spacecraft's surface requires lower level of heat protection. This comes with a drawback. Namely stability and control of the spacecraft becomes unpredictable, as leeward side separation lowers the effectiveness of vertical tall, effecting yaw stability [Atkinson et al., 2013]. Currently used system for spacecraft steering during reentry is Reaction Control System (RCS). This system has two drawbacks, namely it is comprised of mechanical parts and it requires fuel for operation. Both of these drawbacks contribute to an increase in spacecraft mass and a decrease in its reliability. If RCS was replaced with system made of magnetically accelerated surface plasma actuators numerous benefits could be gained. Some of these benefits are: very low mass, cost and power consumption; extremely fast response; and an increased reliability due to lack of moving mechanical parts. Thus the goal of research made by [Atkinson et al., 2013] was to explore the feasibility of using these actuators to control complex flow structure around reentry spacecraft.

3.4 Chapter Conclusions

In order to answer research question , literature on DBD actuator operation in high Mach number flow fields had to be reviewed. It was found that the number of researches and literature papers concerning this subject is currently very limited. However several problems associated with usage of DBD actuator in high velocity flow field were found. [Nishihara et al., 2011] found that the main problem at supersonic or higher velocities is difficulty to conserve high discharge electric field and high space charge density. Also at hypersonic velocities stagnation point temperatures reach 12500 K [Bhatia et al., 2014], meaning that dissociation and ionization of molecules will occur. As the main problem associated with hypersonic flight is the alteration of chemical and thermal properties of air, and in order to keep scope of this thesis manageable, it was decided to limit Mach number to 5.5. Beside all mentioned problems [Nishihara et al., 2011] found out that DBD actuator positioned close to stagnation point at M=5 flow, is capable of altering natural bow shock, increasing its stand-off distance up to 25%. [Bhatia et al., 2014] found that by shock wave modification one can solve problems of large mechanical and thermal loads, that occur while flying in supersonic and hypersonic flow. In addition to this as a result of shock wave stand-off distance modification, pressure distribution on a body also changes. Meaning that by applying DBD plasma actuator close to stagnation point, one can introduce controlling moments and steer the spacecraft.

4 ATMOSPHERIC CONDITIONS

If the most common application is considered, where spacecraft orbits the Earth, its life can be divided into three stages: launch, orbit, and re-entry. During launch and re-entry there will be trend of decreasing and increasing atmospheric conditions respectively. DBD actuator's performance is influenced by atmospheric conditions. Density and number of atmospheric constituents influences transfer of momentum between particles (Section 2.2); ionization rate and ion drift velocity are influenced by pressure and applied electric field (Section 5.2); and temperature gradients influence performance and strength of dielectric material (Section 7.1). As aim of this research is to apply plasma actuator to space-based system it is out of most importance to find operational range and limitations relating all three stages.

Previous chapter states that paper made by [Benard et al., 2008a] is the only one which deals with DBD actuator operation in the low pressure environment. The lowest considered pressure corresponds to an altitude of about 12 km. This shows knowledge gap considering DBD actuator operation at altitudes above this altitude. One of the thesis goals is to investigate actuator's performance at altitudes higher than 12 km. Actuator performance will be computed using parametric model, for which a defined atmospheric parameters are needed.

Neutral atmosphere surrounding the Earth can be divided into three regions:

1. Homosphere (surface up to about 90 km)
    - Troposphere (surface $\rightarrow$ 11 km)
    - Stratosphere (11 km $\rightarrow$ 50 km)
    - Mesosphere (50 km $\rightarrow$ 90 km)
2. Thermosphere (from about 90 km up to 400 km); and
3. Exosphere (above 400 km)

Parameters that are of most interest for this research are the density, atmospheric constituents, pressure, atomic mean free path, dynamic viscosity and temperature. These are going to be covered and plotted in following sections in order to find operational range and limitations of DBD plasma actuators.

4.1 Density

Density is defined as the amount of particles per unit of volume. It is decreasing with altitude and it is out of most importance to find the operating range for DBD actuators. In this research density is going to be calculated using two models that are suggested by European Cooperation for Space Standardization (ECSS). First model is the US Naval Research Laboratory Mass Spectrometer Incoherent Scatter Radar Extended Model (NRLMSISE-00). Its main goal is to describe the neutral temperature and atmosphere constituent's density as a function of altitude. This model is based on extensive measurements made by satellites, rockets and radars, with a large temporal and spatial distribution [ECSS-E-ST-10-04C, 2008]. This model can be

used from the Earth's surface up to the exosphere, but according to the [ECSS-E-ST-10-04C, 2008], when atmospheric density estimation is needed, it shall be used up to altitude of 120 km. Inputs required by NRLMSISE-00, and outputs it provides are presented in Table 4.1

Table 4.1: NRLMSISE-00 Inputs and Outputs

Inputs	Outputs
Time of the day	Total number of following
Day, Month, Year	constituents: O, O_2, N_2,
Geographic Longitude	He, Ar, H, N
Geographic Magnitude	and Anomalous O
Desired Altitude Range	Temperature
F10.7 - Daily Solar Flux	Atmospheric Density
$F10.7_{avg}$ 81 day	
Averaged Solar Flux	
Ap - Daily Magnetic Index	

It should be noted that for the mean activity conditions (that will be used in this research) the estimated uncertainty of the NRLMSISE-00 species density is 15% [ECSS-E-ST-10-04C, 2008]. Before moving onto another model, one shall first explain some of the indices used in NRLMSISE-00.

- F10.7 index is the solar radio flux at 10.7 cm (2800 MHz). In meteorological estimation this index is an excellent indicator of solar activity. It is a good proxy for the combination of coronal solar emissions modulated by bright solar active regions and chromatic transition region, whose energies are deposited in the thermosphere of the Earth's atmosphere [Bowman et al., 2008].
- Ap index describes the amplitude of planetary geomagnetic activity for a given day.

According to the [ECSS-E-ST-10-04C, 2008], above 120 km, one shall use Jacchia-Bowman 2006 (JB-2006) model for density estimations. This is a thermospheric density model that also describes temperature in thermosphere and exosphere. JB-2006 includes two important novel features:

1. *"Novel formulation concerns the semi-annual density variation observed in the thermosphere, but not previously included in any of the semi-empirical atmospheric models"* [ECSS-E-ST-10-04C, 2008]
2. *"Now formulation of solar indices, relating more realistically to the dependence of heat and energy inputs from the solar radiation to specific altitude regions and heating processes within the upper atmosphere"* [ECSS-E-ST-10-04C, 2008]

New indices are presented in list below:

- *"S10.7 index is integrated (26-34 nm) solar emission activity indicator. The energy in this band-pass comes from solar active regions, plage and network. A running 81-day centered smoothed set of values using the moving boxcar method was created, and these data are referred to as* $S10.7_{avg}$*"* [Bowman et al., 2008]
- *"M10.7 index is derived from Mg II core-to-wing ratio that originates from the NOAA series operational satellites. The Mg II core-to-wing ratio is calculated between the variable lines and nearly non-varying*

wings. The result is a measure of chromospheric and some photospheric solar active region activity independent of instrument sensitivity change through time, and is referred to as the Mg II core-to-wing. A running 81-day centered smoothed set of values using the moving boxcar method was created, and these data are referred to as M10.7$_{avg}$" [Bowman et al., 2008]

In order to plot density versus altitude for both of these models, one has define all input parameters. Chosen altitude range is from the Earth's surface until 400 km in altitude. If re-entry applications were later chosen in as potential DBD application to space based system, one could argue that 400 km of altitude is too high. However as at this research is a feasibility study, one must consider high altitudes as well. The value of 400 km was chosen to limit the scope of this research. As suggested by [ECSS-E-ST-10-04C, 2008] chosen indices for NRLMSISE-00 are presented in Table 4.2. Data for high solar activity is not taken into consideration, due to problem for DBD actuator operation associated with lack of atmospheric density, as the momentum exchange reduces with decrease in density. Thus making the low solar activity data more critical. Subscript ***avg*** stands for the 81 day average centered around chosen date.

According to the standard for the short term and local-scale variations, the estimated uncertainty of NRLMSISE-00 species density is 100%. Within the homosphere, the uncertainty of this model is below 5%. Also for mean solar activity

Table 4.2: NRLMSISE-00 Conditions and Indices

Low Solar Activity:	Moderate Solar Activity:
$F10.7 = 65$	$F10.7 = 140$
$F10.7_{avg} = 65$	$F10.7_{avg} = 140$
$Ap = 0$	$Ap = 15$

According to [ECSS-E-ST-10-04C, 2008] conditions and indices used in modelling density with JB-2006 model are showed in Table 4.3.

Table 4.3: JB-2006 Conditions and Indices

	$F10.7$	$F10.7_{avg}$	$S10.7$	$S10.7_{avg}$	$M10.7$	$M10.7_{avg}$	Ap
Low Solar Activity	65	65	60	60	60	60	0
Moderate Solar Activity	140	140	125	125	125	125	15

Expected uncertainties when using these two models in above stated conditions are [ECSS-E-ST-10-04C, 2008]:

- Estimated uncertainty of species density, for a short term and local-scale variations using NRLMSISE-00 is 100%.
- Within the homosphere, the uncertainty of NRLMSISE-00 is below 5%.
- For mean solar activity conditions, the estimated uncertainty of the JB-2006 total density within the thermosphere is 10-15% (depending on altitude)

Density as a function of altitude can be seen in Figure 4.1 .

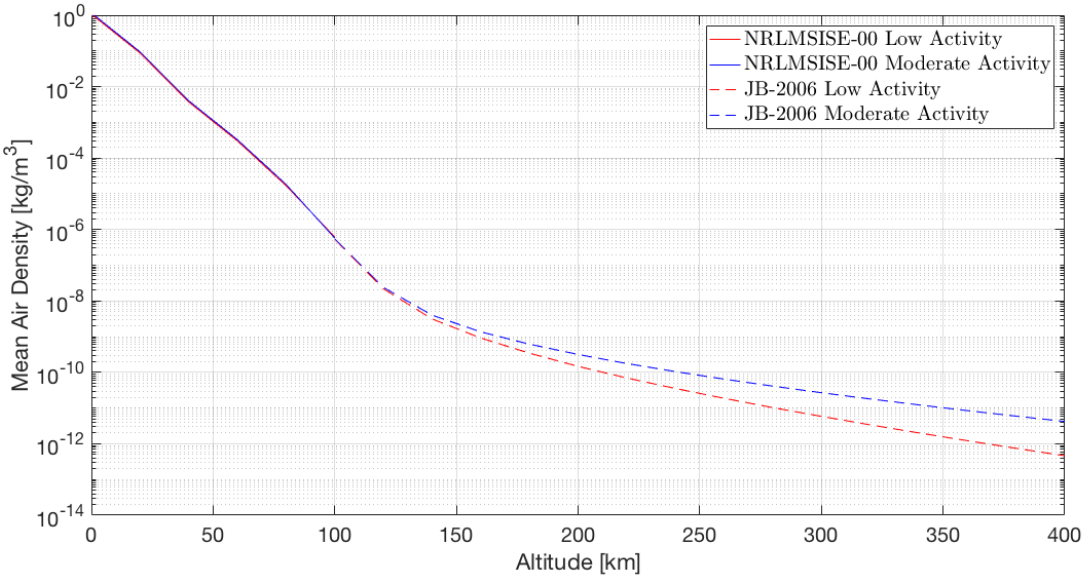

Figure 4.1: Density as a function of altitude estimated using NRLMSISE-00 and JB-2006

4.2 Atmospheric Constituents

In order to estimate atmospheric constituents as a function of altitude NRLMSISE-00 shall be used [ECSS-E-ST-10-04C, 2008]. This model focuses on eight most present particle types, namely Helium (He), Oxygen (O), di-atomic Oxygen (O_2), Nitrogen (N), di-atomic Nitrogen (N_2), Argon (Ar), Hydrogen (H) and anomalous Oxygen. Data provided by the ECSS standard was used to plot two figures, Figure 4.2 and Figure 4.3, which respectively represent number of constituents for low and moderate solar activity. Conditions used in for plotting these are the same as in Table 4.2.

As it can be seen from two figures 4.2 and 4.3, the data is missing for constituents that are below 100 km altitude. This was done in order to clearly represent constituents at an altitudes above 100 km. For altitudes below 100 km please refer to Figure 4.4. Here it is clear that there exists no major difference between low and moderate solar activity case.

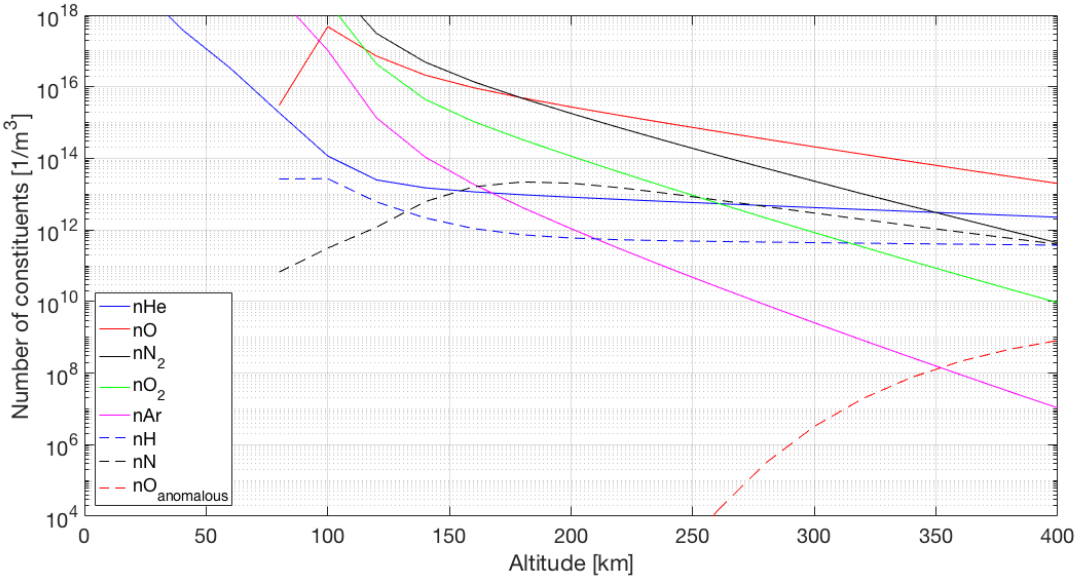

Figure 4.2: Atmospheric constituents profile for low solar and geomagnetic activities estimated using NRLMSISE-00

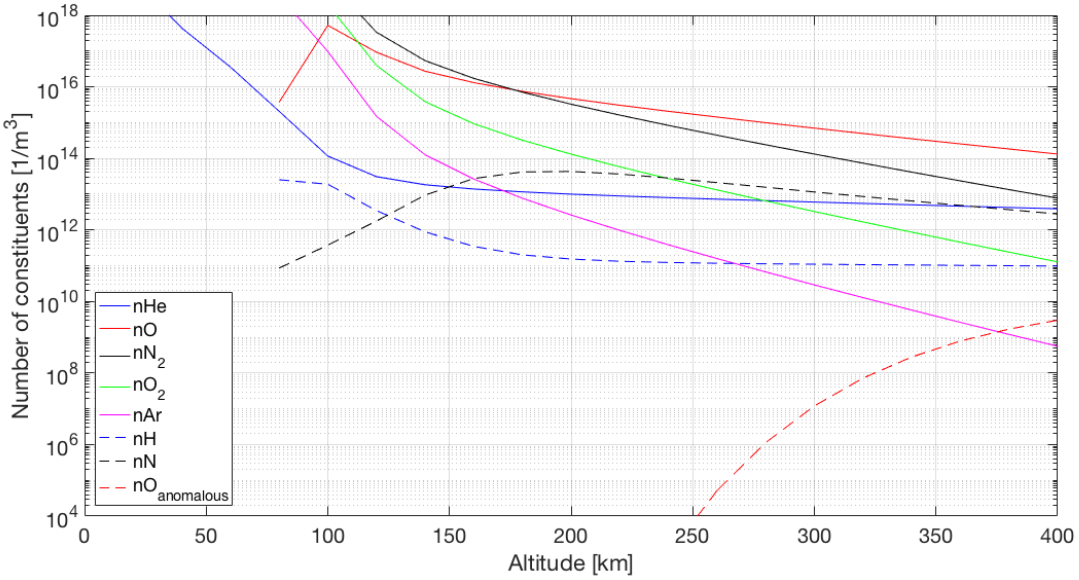

Figure 4.3: Atmospheric constituents profile for moderate solar and geomagnetic activities estimated using NRLMSISE-00

Figure 4.4 shows that there is no major difference between low and moderate solar activity case. At an altitude below 80 km, atmosphere is mostly created by two elements: N_2 of about 78.1 % and O_2 of about 20.96 %. Thus these two particle types will be out of most importance in future modelling. Note that Argon molecule has higher molar mass than O_2 and N_2 (M_{Ar} = 39.948 [g/mol]> M_{O_2} = 31.998 [g/mol]> M_{N_2} = 28.014 [g/mol]). However as its percentage in air mixture at this altitude is lower than 1%, thus when modelling it

is safe to assume that air is composed out of two most present gasses N_2 and O_2.

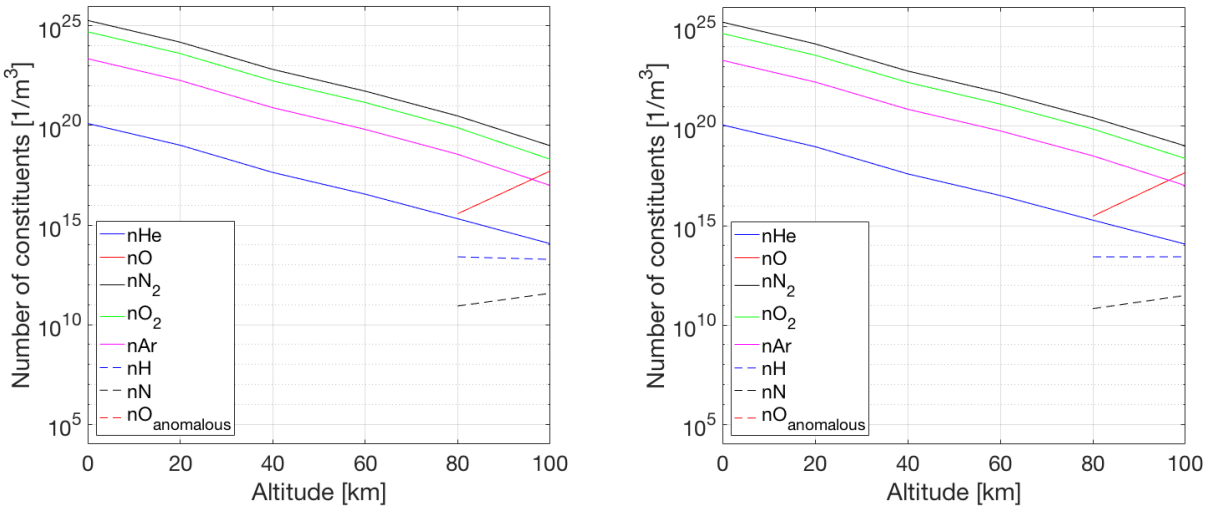

(a) (b)

Figure 4.4: Atmospheric constituents profile for low (a) and moderate (b) solar and geomagnetic activities estimated using NRLMSISE-00

4.3 Temperature, Pressure and Other Parameters

Temperature profile was obtained using two models, namely NRLMSISE-00 and U.S. Standard Atmosphere. Reason behind using U.S. Standard Atmosphere [Atmosphere, 1976] is that below 80 km in altitude, [ECSS-E-ST-10-04C, 2008] does not provide many data points for NRLMSISE-00. Conditions used for NRLMSISE-00 are presented in Table 4.2.

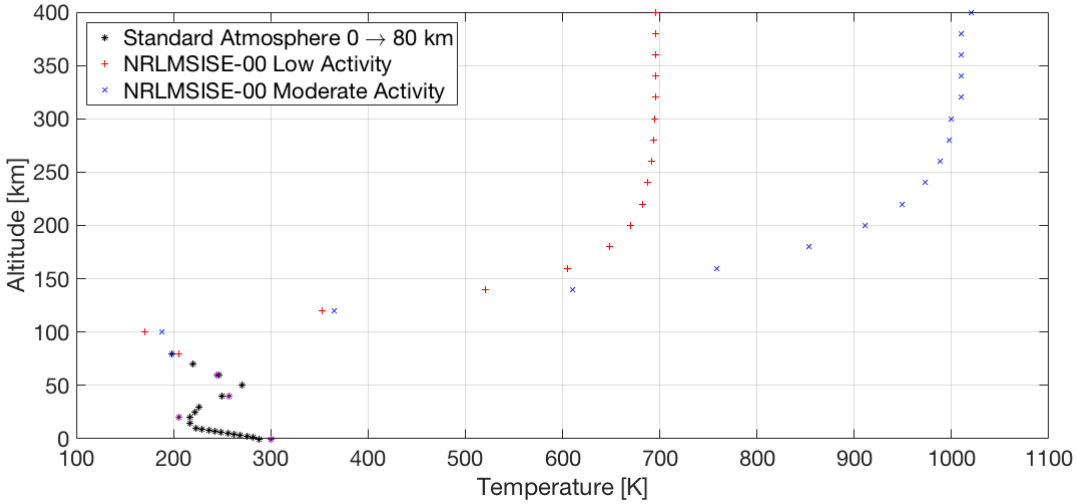

Figure 4.5: Temperature as a function of altitude using [ECSS-E-ST-10-04C, 2008] and [Atmosphere, 1976]

According to obtained results in Figure 4.5, it can be stated that there is no difference in homosphere between three data sets. Above 110 km in altitude, the difference between low and moderate solar activity is evident. Thus in design stage it will be out of most importance to chose a worst case scenario.

[Schlatter, 2009] conducted a research in which he computed the atmospheric composition and a vertical structure to about 1000 km in altitude. Using information provided in this research Figure 4.6 was computed.

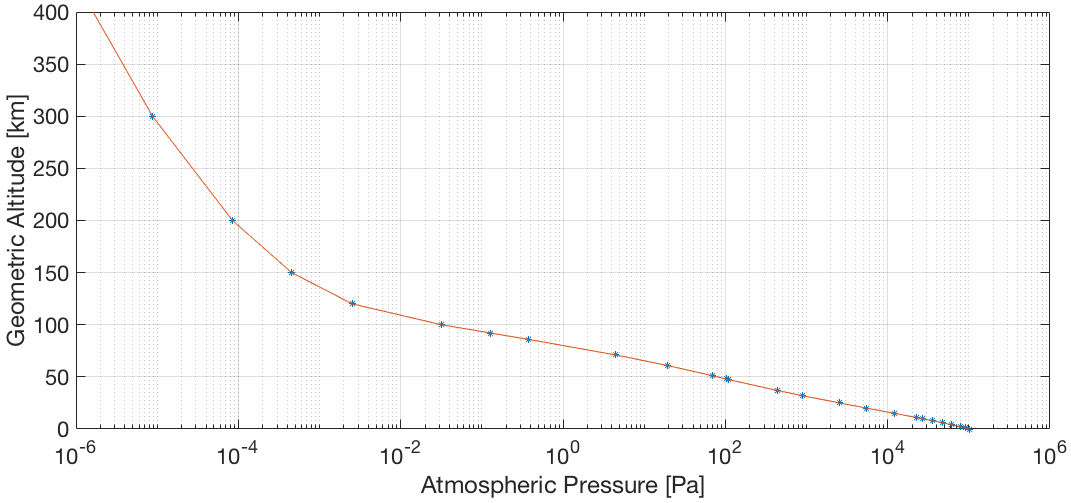

Figure 4.6: Atmospheric pressure as a function of geometric altitude [Schlatter, 2009]

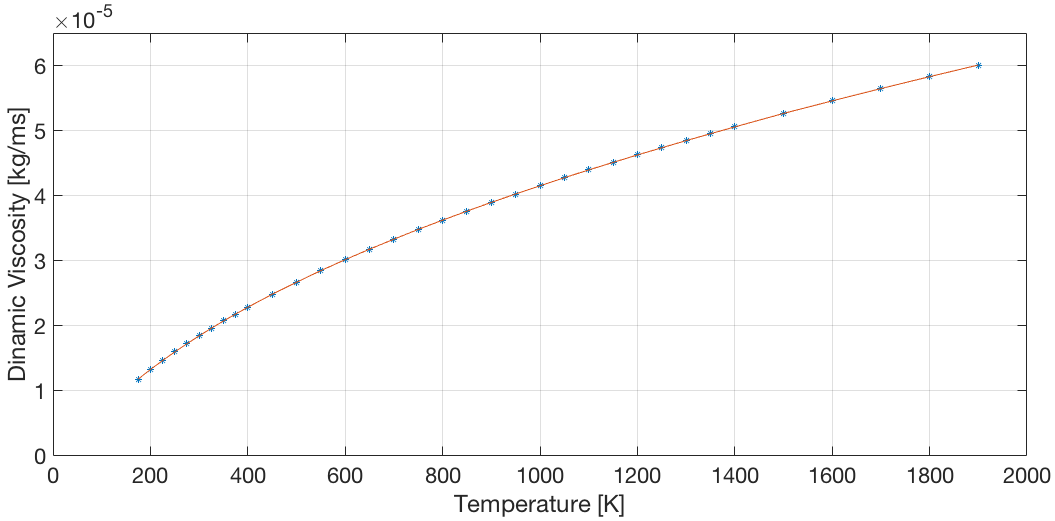

Figure 4.7: Dynamic viscosity μ as a function of temperature

Dynamic viscosity and specific heat constant are two parameters that vary with temperature. Their relations are plotted until 2900 K due to data unavailability for higher temperature values. Sparsity of data can be explained by a fact that at 2000 K O_2 molecules dissociate; at higher temperatures other molecules also dissociate and ionize. This is difficult to model and even challenging to experimentally test. More on molecule

dissociation will be covered in Section 3.3. Dynamic viscosity of air and specific heat constant as a function of altitude can be seen in Figure 4.7 and Figure 4.8:

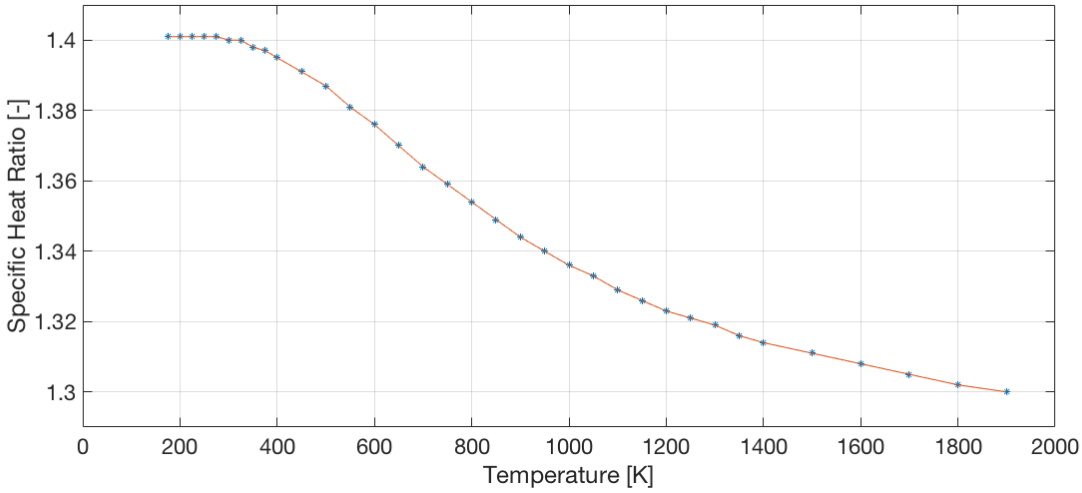

Figure 4.8: Specific heat constant γ as a function of temperature

Last but not least parameter covered in this section concerns mean free path of atoms as they travel through atmosphere. Mean free path is defined by average distance travelled by a moving particle between two successive collisions. It can be found using Equation 4.1. Results are presented as a Figure 4.9.

$$\lambda = \frac{RT}{\sqrt{2}\pi d_a^2 N_a p_{atm}} \tag{4.1}$$

Where:

λ is the mean free path

R is gas constant, $R = 8.314510$ J/Kmol

T is ambient temperature

d_a is collisional cross section, $d_a = 3.57 * 10^{-10}$ m

Na is the Avogardo's number, $Na = 6.0221367 * 10^{23}$ 1/mol

p_{atm} is atmospheric pressure

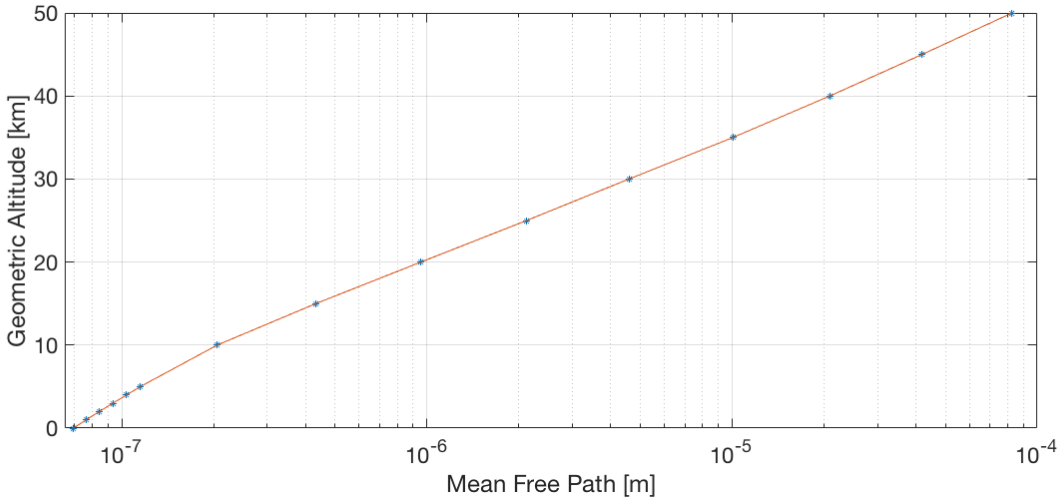

Figure 4.9: Mean free path as a function of altitude

4.4 Chapter Conclusions

Atmospheric conditions as a function of altitude are presented. In previous two chapters it was found that characteristics and performance of DBD actuators vary with atmospheric conditions. This means that definition of Earth's atmosphere is critical for this research, in order to provide DBD actuator's performance parameters for different altitudes. Plots were obtained using three models NRLMSISE-00, U.S. Standard Atmosphere and JB-2006 for low and medium solar activities. Different parameters and corresponding plots can be found in list below.

- Density vs. altitude in Figure 4.1
- Atmospheric constituents number vs. altitude in figures 4.2, 4.3 and 4.4
- Altitude vs. temperature in Figure 4.5
- Altitude vs. pressure in Figure 4.6
- Dynamic viscosity vs. temperature in Figure 4.7
- Specific heat constant vs. temperature in Figure 4.8; and
- Mean free path vs. altitude in Figure 4.9

5 EXTENDED DBD ACTUATOR MODEL

In this chapter one will try to expand an existing model in order to test influence of "mechanical" parameters, such as density, temperature and pressure. The influence of "electrical" parameters concerning plasma formation, ionization rate or drift velocity will not be covered by this research. Many models describing body force created by DBD plasma actuators exist. Some of which are made by [Likhanskii et al., 2008], [Jayaraman and Shyy, 2008] or [Kotsonis and Ghaemi, 2012]. All of these do not take into account external flow velocity as a changing parameter, and model plasma body force in quiescent conditions.
Chosen model, that takes external flow into account is developed in-house by [Pereira, 2016]. This model investigates the effect of flow velocity on plasma body force when actuator is positioned inside the boundary layer both in co-flow and counter-flow configurations; taking into account flow velocities from 0 to 60 m/s. As the model takes the assumption of incompressible flow it will not be modified for flow velocities above 100 m/s. Following theoretical method is taken from *Chapter 3: Effect of External Flow Velocity On Momentum Transfer of DBD Actuators*, which is a part of [Pereira, 2016] dissertation. For more detailed explanations please refer to the original source.

5.1 Model Theoretical Background

Plasma actuator that was used in experiments and model development by [Pereira, 2016] is briefly described in this section. Actuator physical characteristics are presented in list below:

- Actuator consists of 2 electrodes separated by dielectric material
- Electrodes were made out of self adhesive copper tapes
- Electrodes were placed next to each other so that there was no gap between them
- Electrode with adhesive layer thickness was 60 μm
- Exposed electrode width was 10 mm and encapsulated electrode width was 20 mm
- Dielectric material was Poly(methyl methacrylate) PMMA, more recognizable under commercial names such as Plexiglas or Acrylic
- Dielectric material thickness was 3 mm

In order to prevent plasma formation on the lower side of the plate, the encapsulated electrode was covered with Kapton tape. Power to the actuator was provided by TREK 20/20C HV amplifier ($\pm$20 kV, $\pm$20 mA) imposing a sinusoidal signal of 40 kV_{pp} applied voltage and 2 kHz carrier frequency on the exposed electrode while keeping the covered electrode at ground potential [Pereira, 2016].

Experimental set-up is showed in Figure 5.1. In it one can see a wind tunnel wall with flow velocity in positive x-direction; electrodes, load cell, dielectric material; and expected forces with their directions. For detailed explanation of the testing facilities used please refer to the original source.

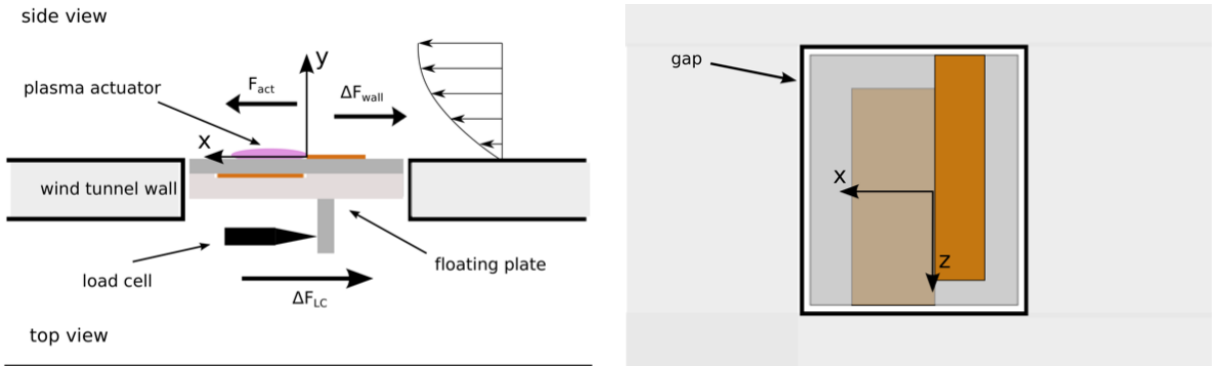

(a) (b)

Figure 5.1: Experimental set-up (not to scale) as defined by [Pereira, 2016] from (a) side view and (b) top view

Figure 5.1 shows both side and top view of the experimental set-up, upon which model was designed. As mentioned earlier, this model tests actuator placement in both co-flow and counter-flow configurations. This was achieved by changing the geometrical configuration of two electrodes with respect to incoming free stream flow. This is presented in Figure 5.2.

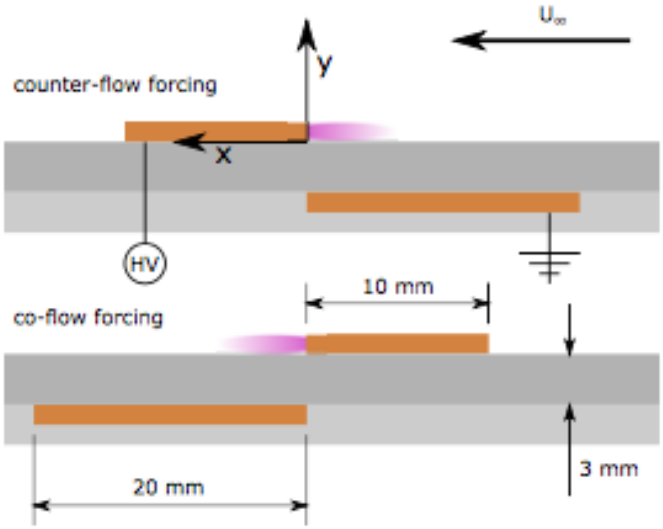

Figure 5.2: Electrode placement in both configurations as defined by [Pereira et al., 2014]

Next to already stated force measurements, Chapter 3 of [Pereira, 2016] also deals with electrical power consumption and plasma light intensity level measurements. As these two are not the focus of this research, they will not be covered here. For experimental set-up and equations used in model for computation of these parameters please refer to [Pereira, 2016] dissertation.

5.1.1 Baseline boundary layer

According to the author, wind tunnel boundary layer was characterized in order to establish the state and scale of the flow in which actuator is operating. Velocities were measured using system consisting of a Pitot tube and Mensor DPG 2400 digital manometer used for measurement of total pressure outside and inside boundary layer and static pressure inside the boundary layer. According to the author the velocity profile U(y) of the boundary layer can be characterized through parameter named shape factor H_{12}. As earlier stated, this experiment and model only takes into account the incompressible flow, the shape factor using this assumption is given by:

$$H_{12} = \frac{\delta_1}{\delta_2} = \frac{\int_0^\infty (1 - \frac{U(y)}{U_\infty})dy}{\int_0^\infty \frac{U(y)}{U_\infty}(1 - \frac{U(y)}{U_\infty})dy} \tag{5.1}$$

Where:

- δ_1 is the integral boundary layer parameter defining the displacement thickness
- δ_2 is the integral boundary layer parameter defining the momentum thickness

According to the author: *"the upper limit of the integrals in above equation was set at δ_{99}, corresponding to the wall distance at which $U(\delta_{99}) = 0.99\ U_\infty$"[Pereira, 2016].* The wall shear stress was computed using equation below:

$$\tau_{wall} = \mu \frac{\partial U}{\partial y}|_{y=0} \tag{5.2}$$

Where:

- μ is the air dynamic viscosity and it changes with change of temperature. Thus one has to make sure to change this parameter when model is modified for different altitudes

According to [Pereira et al., 2014]: *"air speed U_0 is the velocity 'felt' by the plasma due to the wind tunnel wall boundary layer, computed as the average velocity in the boundary layer up to the height of the body force region"*:

$$U_0(U_\infty) = \frac{1}{h}\int_0^\infty U(y)dy \tag{5.3}$$

Where:

- h is the height of body force region. According to the author for this study h=1 mm based on previous measurements made by [Kotsonis and Ghaemi, 2012]

Obtained results for the boundary layer without interference of the plasma actuator is presented in Table 5.1:

Table 5.1: Non-actuated boundary layer characteristics as calculated by [Pereira, 2016]

U_∞ (m/s)	δ_{99} (mm)	H_{12}	τ_{wall} (Pa)	U_0 (m/s)
10	10.1	2.02	0.058	1.4
20	9.5	1.28	1.04	10.3
30	10.4	1.32	1.38	13.9
40	9.6	1.29	2.03	20.2
50	9.2	1.31	2.62	24.5
60	8.9	1.27	3.18	30.7

Results from table above will be later used in model for computation of the forces.

5.1.2 Momentum transfer model

This section has aim in explaining simple analytical model developed by [Pereira, 2016] that estimates the impact of external flow velocity on the momentum exchange between created ions and neutral air particles. This model takes two very influential assumptions, namely, the incompressibility of the flow (as earlier mentioned) and impermeability of the wall. First mentioned assumption limits applicability of this model for space based systems. However as earlier found in Section 3.3 DBD plasma actuator can be used near the stagnation point for supersonic flight, as at this point flow velocity is equal to zero.

Author defines a body force as a distributed force exerted by plasma discharge on the surrounding volume of neutral air. Term force is used by author to represent an integrated total body force the actuator is exerting on the flow. As this research is modification of existing [Pereira, 2016] model, these terms with their meaning will also be used here. If one observes Equation 5.4 it can be seen that the force measured by the load cell is actually the difference of measured force when actuator is turned on and off. This means that force created by the actuator can be found by this difference in load cell measurements. To this difference one must also add the difference in skin friction developed at the wall as a result of actuation. According to the [Pereira, 2016] one can expect this because boundary layer profile is going to change due to applied actuation.

$$\Delta \overrightarrow{\mathrm{F}}_{LC} = \overrightarrow{\mathrm{F}}_{LC_{on}} - \overrightarrow{\mathrm{F}}_{LC_{off}} = \overrightarrow{\mathrm{F}}_{act} + \Delta \overrightarrow{\mathrm{F}}_{wall} = \overrightarrow{\mathrm{F}}_{act} + (\overrightarrow{\mathrm{F}}_{wall_{on}} - \overrightarrow{\mathrm{F}}_{wall_{off}}) \tag{5.4}$$

Where subscripts represent:

LC $\rightarrow$ load cell

on/off $\rightarrow$ actuator is powered on and off

act $\rightarrow$ actuator

In order to model these forces in MATLAB author defined a computational model schematic where body force region is divided into N elements along the stream-wise direction. In model provided by the author, grounded electrode length l is divided into 500 elements (N=500). Schematic for co-flow forcing is presented in Figure 5.3.

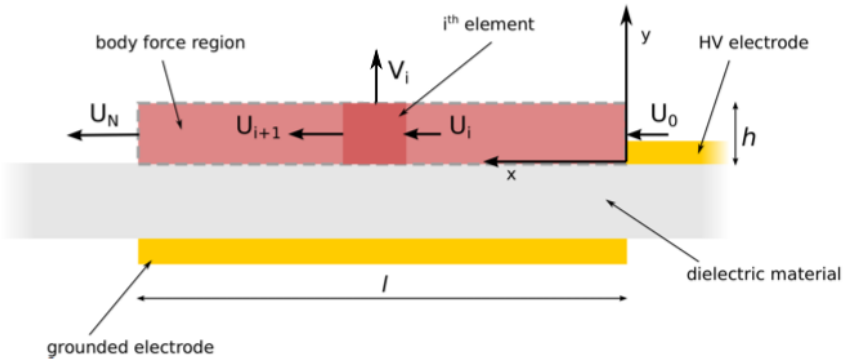

Figure 5.3: Element size and parameters for model concerning co-flow forcing as defined by [Pereira, 2016]

According to [Pereira, 2016] mass conservation of the i^{th} element can be computed using:

$$\nabla.\overrightarrow{\mathrm{U}} = 0 \rightarrow \frac{U_{i+1} - U_i}{dl} + \frac{V_i}{h} = 0 \tag{5.5}$$

Where:

$\overrightarrow{\mathrm{U}}$ represents the fluid velocity vector consisting of U and V components corresponding to velocities in x and y directions respectively

dl is the element length (covered electrode length $l = 0.02$ divided by number of elements $N = 500$)

Conservation of momentum in positive x direction can be described by:

$$dF_x = \int\int \overrightarrow{\mathrm{U}}(\rho\overrightarrow{\mathrm{U}}.\overrightarrow{\mathrm{n}})dA = \rho(U_{i+1}^2 - U_i^2).h + \frac{U_{i+1} + U_i}{2}\rho.V_i.dl \tag{5.6}$$

Where:

dF_x is the force in x direction acting on the element

ρ is atmospheric density defined in Chapter 4

dA is the elemental area

$\overrightarrow{\mathrm{n}}$ is the vector normal ro element surface pointing outwards

Combining equations 5.5 and 5.6 one can find:

$$dF_x = \frac{1}{2}\rho.h(U_{i+1}^2 - U_i^2) \tag{5.7}$$

Author also decomposes the left hand side of Equation 5.7 into sum presented below:

$$dF_x = dF_{act} + dF_{shear} \tag{5.8}$$

Where:

dF_{act} is the force produced by the actuator in x direction

dF_{shear} is shear force coming from viscosity of the fluid at each element

Author assumes that the atmosphere is composed out of two most concentrated molecules (N_2 and O_2). [Pereira, 2016] also assumes that momentum of the ionized (charged) species is transferred to neutral particles through numerous collisions, in a way that velocity after momentum transfer is the same for all molecules, across each fluid element i. Author makes another assumption by making no distinction between positive, negative ions and free radicals for the sake of simplicity. With all above stated the momentum added to the flow at each element can be found using Equation 5.9.

$$dp_i = \rho h i_D (V_D - U_i) dl \tag{5.9}$$

Where:

dp_i is the change in momentum

i_D is the fraction of ionized species in plasma compared to neural air molecules

V_D is the ion drift velocity

To compute i_D author uses a lower complexity solution , where he assumes [Pavon et al., 2007] statement, that the intensity of light emitted by the discharge is proportional to the ionized fraction. [Pereira et al., 2014] experimentally computed the ionized fraction spatial distribution and presents it as a Figure 5.4. This figure consists out of four parts. Left side shows co-flow forcing configuration, while the right side shows counter-flow forcing configuration. Lower part of the figure parts (c) and (d) show zoomed versions of (a) and (b) respectively, representing detailed parts near the electrode edge.

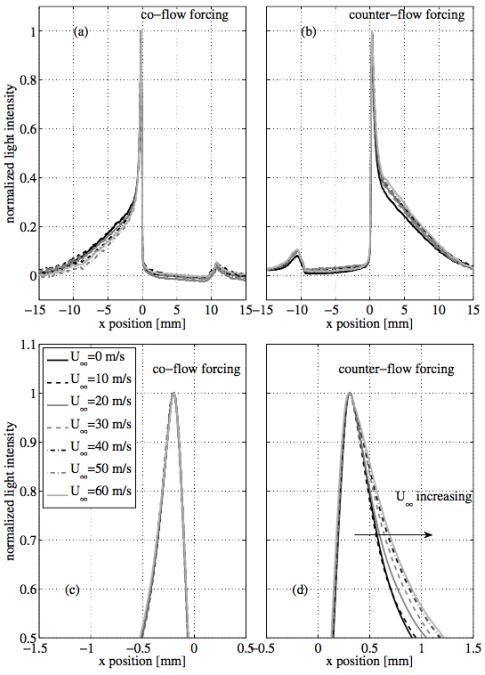

Figure 5.4: Integrated and normalized light intensity of discharge as computed by [Pereira et al., 2014]

Author scaled the maximum values occurring at electrode edge, lower part of Figure 5.4, to match value computed by [Massines et al., 1998]. [Pereira, 2016] reported the imposed ionized fraction distribution as a Figure 5.5.

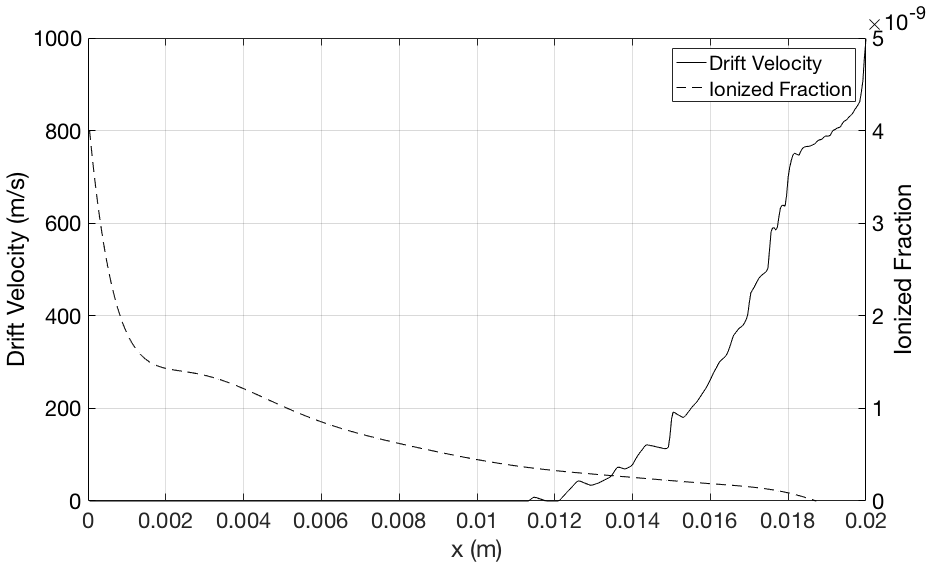

Figure 5.5: Imposed ionized fraction distribution computed by [Pereira, 2016]

To compute spatial distribution of the average ion drift velocity author uses electrostatic field computed with Poisson equation. Dielectric material characteristics, PMMA's permittivity equals 3 and applied voltage is kept constant at 20 kV. These two parameters were chosen to stay constant for later model adaption with idea to keep the same test set-up. Knowing this, one can compute horizontal component of electric field at the body force region using Equation 5.10.

$$E_x(x) = \frac{1}{h}\int_{y=0}^{h} E_x dy(x) \tag{5.10}$$

[Pereira, 2016] derives ion drift velocity using Equation 5.11.

$$V_D = 0.79 V_{D_{N_2^+}} + 0.21 V_{D_{O_2^+}} \tag{5.11}$$

[Pereira, 2016] states that only positive ions contribute to ion drift velocity as the negative ions (O^-,O_2^-) does not affect model estimations as they have velocity which is in same order of magnitude [McKnight, 1970]. Body force of each element can be found using Newton's second law:

$$dF_{act} = \frac{dp_i}{dt} \tag{5.12}$$

Where:

- dt is the characteristic time during which momentum transfer across each element is performed. It can be computed using relation: $dt = \frac{\lambda}{V_D}$
- λ is mean free path, which is the average distance travelled by a moving particle between two successive collisions. This parameter depends on atmospheric pressure meaning that one has to modify this parameter as pressure changes according to Chapter 4.

In order to compute wall shear stresses at wall surface and top of the fluid element author assumes a first order approximation meaning that the gradient of velocity normal to the wall is estimated using average

velocity in the element at the representative height ($y = kh$). [Pereira, 2016] defines a representative height assuming a linear velocity profile, where product kh represents the distance from the wall at which U_0 gives the same shear stress as determined earlier experimentally:

$$\frac{\mu U_0}{kh} = \tau_{wall} \Rightarrow k = \frac{\mu U_0}{k\tau_{wall}} \tag{5.13}$$

Assuming that the shear force at the top elemental edge is kept constant throughout the considered control volume its value is set such that the boundary layer is in force equilibrium when no plasma is present. According to [Pereira, 2016] shear force at each i^{th} element is given by Equation 5.14.

$$dF_{shear} = dF_{edge} + dF_{wall} \approx \frac{\mu}{kh}(U_0 - U_i)dl \tag{5.14}$$

To compute the velocity of proceeding element (U_{i+1}) using marching scheme, one has to combine equations 5.14, 5.12 and 5.7. Marching procedure shall be initiated using starting velocity taken from Table 5.1. This value is experimentally found by [Pereira, 2016].

$$U_{i+1}^2 = U_i^2 + 2\frac{V_D}{\lambda} i_D (V_D - U_i)dl + 2\frac{\mu}{\rho k h^2}(U_0 - U_i)dl \tag{5.15}$$

Total body force that fluid experiences over plasma region can be computed using Equation 5.16.

$$F_x = \rho h(U_N^2 - U_0^2) + \sum_{i=0}^{N} \frac{U_i + U_{i+1}}{2} \rho V_i dl \tag{5.16}$$

Similarly, the wall shear force over plasma region is given by Equation 5.17

$$F_{wall} = -\sum_{i=0}^{N} \mu \frac{U_i}{kh} dl \tag{5.17}$$

According to [Pereira, 2016] the shear force at the upper edge of the control volume can be found using Equation 5.18.

$$F_{edge} = \frac{\mu U_0}{kh} l \tag{5.18}$$

Finally combining above three equations one can find the isolated actuator body force using Equation 5.19.

$$F_{act} = F_x - (F_{edge} + F_{wall}) \tag{5.19}$$

5.1.3 Sea level base results

This section is going to present results obtained by [Pereira, 2016] in his dissertation. These are obtained at sea level altitude under influence of external flow velocities ranging from 0 to 60 m/s for both co-flow and counter-flow configurations. After this in Section 5.2, this simple analytical model is going to be modified in a way to represent operation of same DBD plasma actuator under free stream velocity of M=5 at different altitudes ranging from 10 to 50 km. Reason behind chosen Mach number is given in Chapter 3 and altitude range will be defined later in this section. Modified values and plots are going to be compared to the base results obtained by [Pereira, 2016].

Model input variables are presented in Table 5.2. Only the first six parameters will be modified in model adaption. Reason behind this is going to be given in Section 5.2.

Table 5.2: Input parameters as defined by [Pereira, 2016]

Parameter	Value	Note
ρ	1.225 (kg/m^3)	atmospheric density
λ	$6 * 10^{-8}$ (m)	mean free path
T	293.15 (K)	atmospheric temperature
p_{atm}	760 $(mmHg)$	atmospheric pressure
μ	$1.85 * 10^{-5}$ (kg/ms)	dynamic viscosity
n_a	$2.5 * 10^{25}$ $(1/m^3)$	molecular concentration
N	500 $(-)$	number of points
l	0.02 (m)	body force length
h	0.001 (m)	body force height
f	2000 (Hz)	applied frequency
V_{d_0}	400 (m/s)	initial drift velocity
n_i	$1 * 10^{17}$ $(1/m^3)$	plasma ion concentration
V_{max}	20000 (V)	maximum applied voltage
T_0	273.15 (K)	zero Celsius in Kelvin
p_0	$p_0 = p_{atm}\frac{T_0}{T}$ $(mmHg)$	defined by Hornbeck [Pereira, 2016]
N_{2_f}	0.79 $(-)$	fraction of N_2 in atmosphere
O_{2_f}	0.21 $(-)$	fraction of O_2 in atmosphere
m_{N_2}	28 (g/mol) molar mass of	nitrogen molecule molar mass
m_{O_2}	32 (g/mol)	nitrogen molecule molar mass
h_f	0.5 $(-)$	fraction of h considered to compute friction forces

Up until this point direction of modelled forces were not clearly stated. According to [Pereira, 2016]:

- $\Delta\overrightarrow{\mathrm{F}}_{wall}$ is always opposite to external flow
- $\overrightarrow{\mathrm{F}}_{act}$ is in direction of external flow in co-flow, and in opposite direction when operated in counter-flow forcing configuration
- $\Delta\overrightarrow{\mathrm{F}}_{LC}$ is the reaction force imposed on the load cell, and as such its direction is always opposite of the sum of two previously mentioned forces

Obtained results are showed in following two figures. Figure 5.6 plots force values for co-flow and counter-flow configurations. It compares experimentally obtained with modelled force values as calculated by [Pereira, 2016]. Results from Figure 5.6 show that modelled load cell force for co-flow forcing configuration has trend of slight decrease over complete velocity range. Contrary, when DBD actuator is operated in counter-flow configuration load cell will register an increase in force with increase in free-stream flow velocity. Difference between two forcing configurations can be explained by the difference of momentum exchange between charged ions and neutral particles. According to [Pereira, 2016] in co-flow forcing configuration, difference in velocity is reduced as particles flow in the same direction. With lower velocity difference, the momentum transfer between particles is lesser, meaning registered force on load cell is also lower. Opposite occur in counter-flow configuration. Here velocity difference becomes higher as neutral particles and charged ions travel in opposite direction, meaning higher momentum exchange and higher registered force on load cell. When modelled data

is compared with experimental results, [Pereira, 2016] concludes that results of the two match sufficiently well, and thus validates the model under conditions mentioned in Table 5.2.

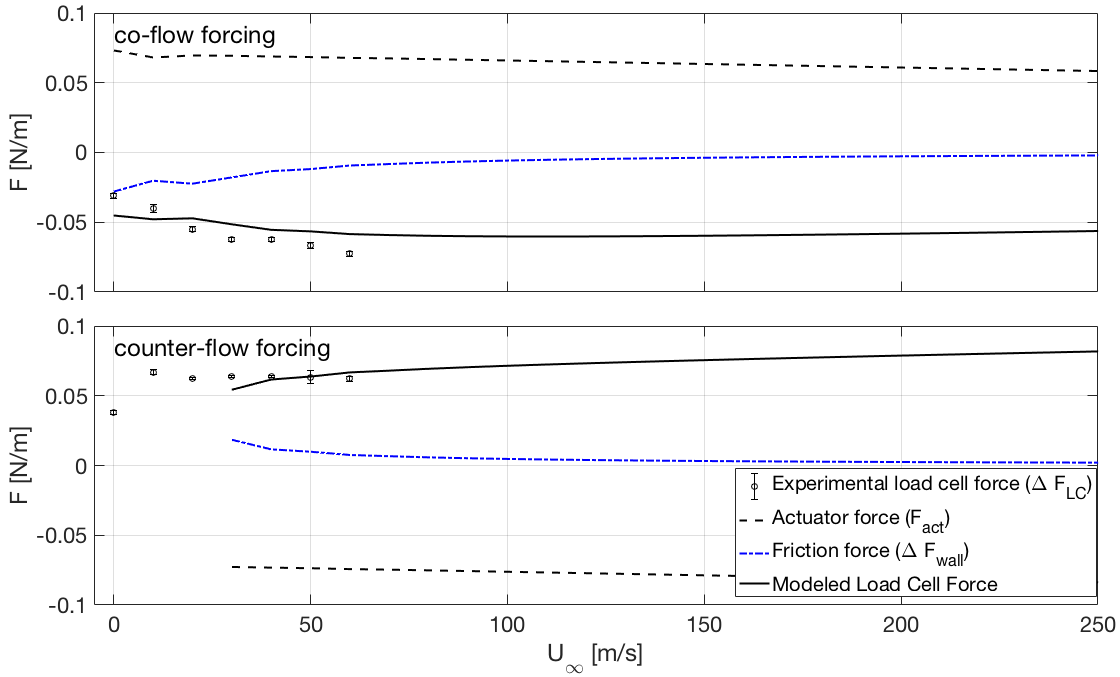

Figure 5.6: Experimental vs. modelled forces as computed by [Pereira, 2016]

If one observes Figure 5.6, it can be seen that for counter-flow forcing configuration plotting starts from 30 m/s. Reason behind this is limitation of this model. As this is a simple model it is not able to take into account reversal flow that occurs as actuator is able to induce flow separation when opposing flow. Reversal flow was predicted to occur up until 30 m/s free airstream. Thus the limitation of this model is its inability to compute load cell force near quiescent conditions for counter-flow forcing configuration. In order to look more into detail between two forcing configurations, Figure 5.7 was created. This figure depicts three individual absolute force terms ($\Delta\overrightarrow{F}_{LC}$, $\Delta\overrightarrow{F}_{wall}$ and $\Delta\overrightarrow{F}_{act}$).

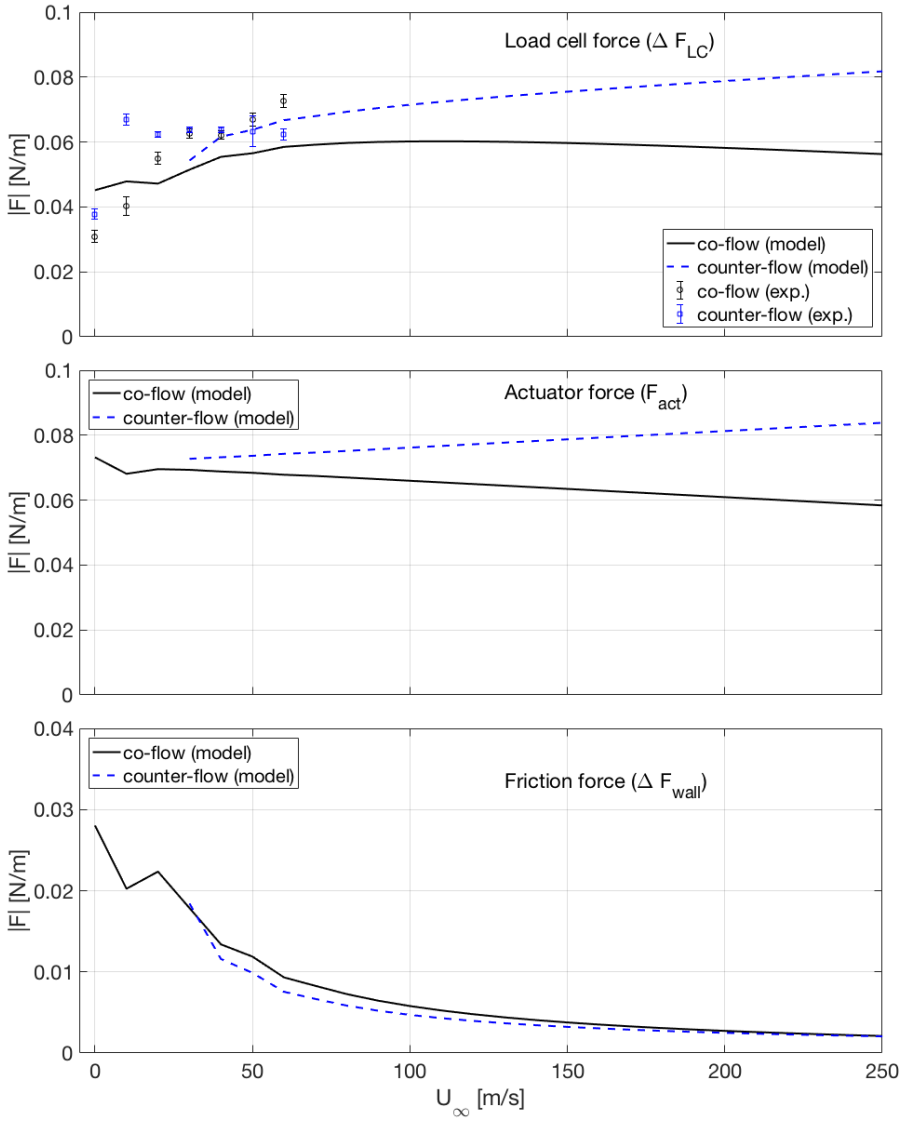

Figure 5.7: Experimental vs. modelled forces as computed by [Pereira, 2016]

Figure 5.7 shows that the effect of wall friction is high at low velocities, but then quickly decreases with increase of external flow velocity for both forcing configurations. Detailed explanation of this phenomenon can be found in [Pereira, 2016].

5.2 Model Extension

Goal of this section is to modify model made by [Pereira, 2016] with goal of extending its operational range for different altitudes. During research it was decided to modify only environmental conditions, while keeping actuator physical parameters constant. Rationale behind this decision was that model and testing equipment used by [Pereira, 2016] are well designed and made in-house. Hence the complete test set-up and actuator already exist and are property of Aerospace Engineering Faculty at TU Delft, meaning that if decided to perform tests, costs will be significantly reduced.

5.2.1 Model changes and new parameters

First problem that arose, during model adaption, concerns its performance in low pressure environment; more precisely relation between E/p_0 and V_D. This relation shows the ion drift velocity as a function of ratio of electric field strength and atmospheric pressure. To find relation between these two parameters, author uses research performed by [Varney, 1953], who computes drift velocities of ions in oxygen, nitrogen and carbon monoxide. Main result of [Varney, 1953] research are two figures presented below.

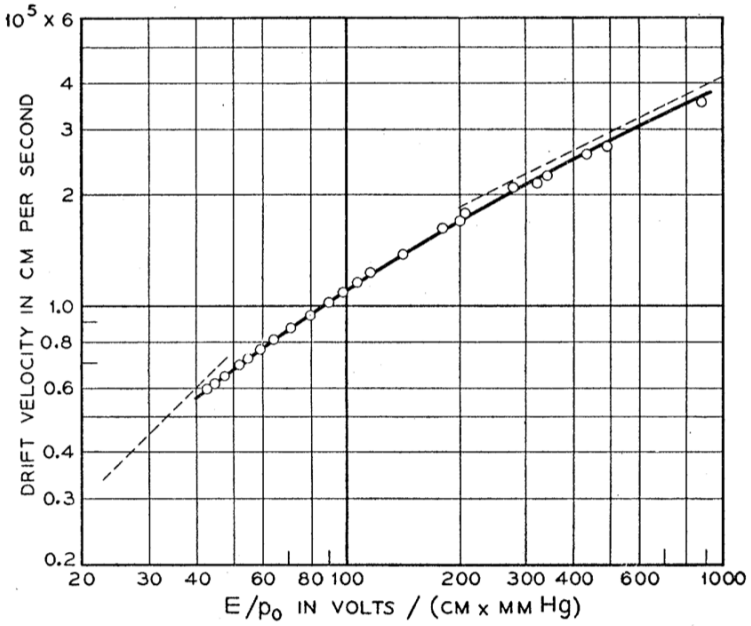

Figure 5.8: Ion drift velocities as a function of E/p_0 in oxygen [Varney, 1953]

Figure 5.8 and Figure 5.9 represent ion drift velocities in Oxygen and Nitrogen gases respectively; and both are plotted in a log-log scale. If one observes these figures, it can be seen that in both cases, x-axis goes until 1000 mark. [Pereira, 2016] takes data points from these graphs and interpolates between them in order to make fit line from 0 to 1000 on x-axis.

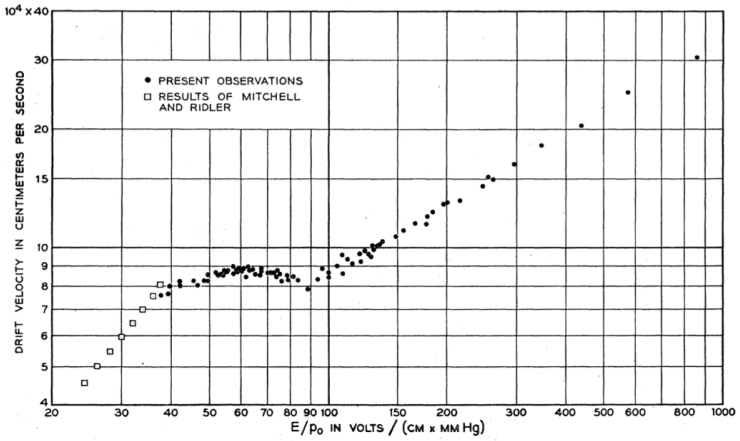

Figure 5.9: Ion drift velocities as a function of E/p_0 in nitrogen [Varney, 1953]

Problem arises when E stays constant as it comes from DBD actuator power supply defined in set-up by [Pereira, 2016], while pressure decreases with altitude. For lower pressures considered in this research ratio of E/p_0 must be extended until 5000. Research that takes into account higher E/p_0 ratios could not be found, so it was decided to extrapolate figures made by [Varney, 1953]. Exponential fit was chosen to extrapolate data. Both lower and higher confidence bounds were plot as extrapolation goes many times over the original range. Extrapolated values are showed in Figure 5.10.

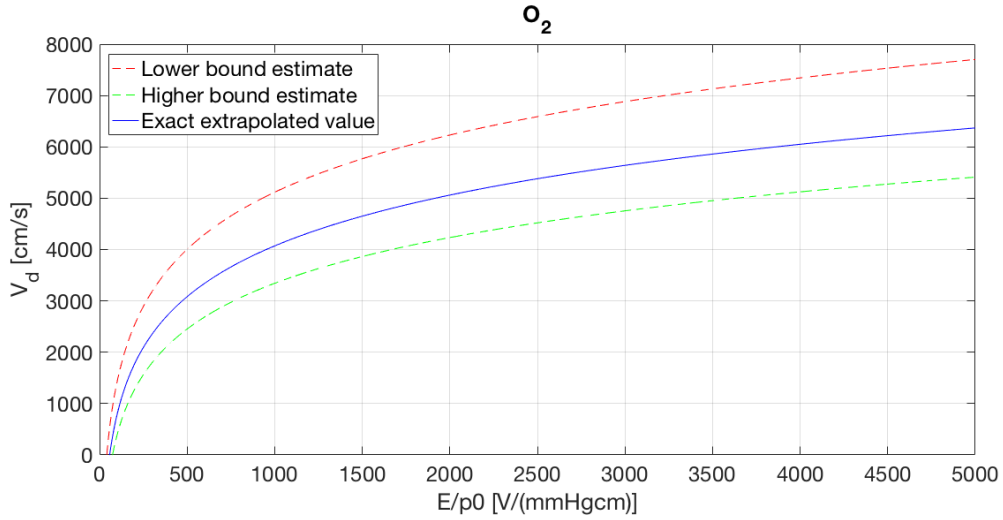

(a)

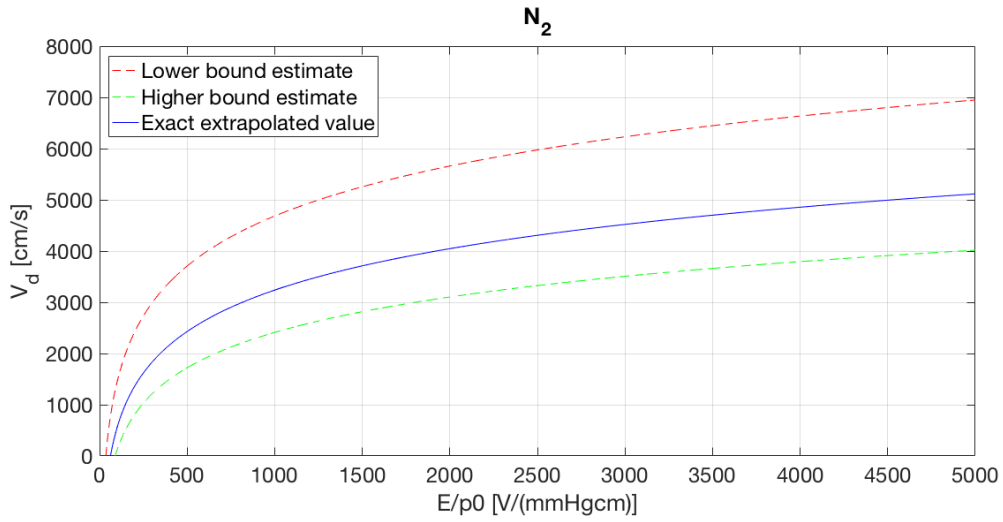

(b)

Figure 5.10: Ion drift velocities as a function of E/p_0 ratio in (a) oxygen and (b) nitrogen gas

In order to verify extrapolation for each of three (higher bound, exact estimation and lower bound) lines, one had to input newly obtained drift velocity values into model using parameters as defined by [Pereira, 2016]. The closest fit of force plots was obtained with use of lower bound confidence values, so it was decided to interpolate this line and continue with model adaption.

Previously defined model will be modified in a way to allow variation of following parameters:

- $\rho \rightarrow$ atmospheric density will be modified according to Section 4.1
- $\lambda \rightarrow$ mean free path will be modified according to Section 4.3
- $T \rightarrow$ atmospheric temperature will be modified according to Section 4.3
- $p_{atm} \rightarrow$ atmospheric pressure will be modified according to Section 4.3
- $\mu \rightarrow$ dynamic viscosity will be modified according to Section 4.3
- $n_a \rightarrow$ molecular concentration will be modified according to Section 4.2

To define above listed parameters and altitude range for which model will be adapted, one has to present possible space-based case scenario. In Chapter 3 all currently available research on plasma actuators operated in high speed (from transonic to hypersonic) flows is presented. Size of the available research and what was found in it shows that operation of DBD actuators at flows characterized by high Mach numbers is followed by many difficulties. Some problems, associated with high temperatures that occur at hypersonic velocities, are thermal stresses that occur in actuator and dissociation/ionization of molecules. Other problems, associated with high velocity of neutral molecules, are negligible momentum exchange between charged ions and surrounding flow field. These problems limit DBD actuator operation at hypersonic velocities. Due to inability to find more parametric or experimental research on DBD actuator in hypersonic velocities, it was decided to combine studies of [Bhatia et al., 2014] and [Nishihara et al., 2011] in order to model application of plasma actuators on a spherical body subjected to M=5 flow field. Next to this, it was decided to adapt [Pereira, 2016] existing model for altitude range from 0 to 50 km. For altitudes above 50 km, atmospheric pressure is limiting calculation of drift velocity. Knowing all earlier said, possible application of DBD plasma actuators at these conditions is for steering of spherical spacecraft while in re-entry or launch stage of flight. Two dimensional spacecraft body can be seen in Figure 5.11

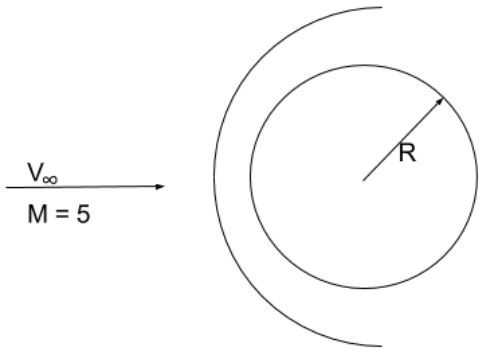

Figure 5.11: Chosen spherical body

Table 5.3: Dependent model parameters before normal shock wave

$H\ (km)$	$\rho\ (kg/m^3)$	$\lambda\ (m)$	$T\ (K)$	$p_{atm}\ (mmHg)$	$\mu\ (kg/ms)$	$n_a\ (1/m^3)$
10	0.3048	$2.054 * 10^{-7}$	223.2	198.766	$1.456 * 10^{-5}$	$5.34565 * 10^{24}$
20	0.0937	$9.556 * 10^{-7}$	216.7	41.471	$1.421 * 10^{-5}$	$1.7237 * 10^{24}$
30	0.01797	$4.595 * 10^{-6}$	226.5	9.016	$1.473 * 10^{-5}$	$3.1508 * 10^{23}$
40	0.00402	$2.091 * 10^{-5}$	250.3	2.189	$1.6 * 10^{-5}$	$6.5325 * 10^{22}$
50	$1.052 * 10^{-3}$	$8.268 * 10^{-5}$	270.6	0.598	$1.7 * 10^{-5}$	$1.859 * 10^{22}$

If Figure 5.11 is observed it can be seen that when spherical body is subjected to flow characterised with Mach number of 5 it experiences shock. According to [Anderson Jr, 2010] atmospheric parameters are going to change across normal shock wave, which can be assumed as DBD actuator is going to be positioned very close to stagnation line, which is normal to velocity vector. Using Appendix B of [Anderson Jr, 2010] for M=5, following scaling ratios were obtained: $p_2/p_1 = 29$, $\rho_2/\rho_1 = 5$, $T_2/T_1 = 5.8$ and $M_2 = 0.4152$; where index 1 and 2 represent conditions before and after normal shock wave respectively. Conditions after shock wave are not the same as ones near stagnation point on spherical body. It is assumed that flow between shock wave and body is incompressible for the sake of simplicity. However this might not be correct as it is safe to assume incompressibility under condition that M<0.3. This assumption will be validated if stagnation pressure at cylinder cone is 32.65 times greater than atmospheric pressure before normal shock wave. This value is taken from Appendix B of [Anderson Jr, 2010] and takes compressibility into account. Finally when incompressibility is assumed, isentropic flow relations shall be used to compute atmospheric conditions in stagnation point. As Mach number after normal shock could not be found in Appendix A of [Anderson Jr, 2010] one has to use equations 5.20, 5.21 and 5.22.

$$\frac{\rho_0}{\rho_2} = \left(1 + \frac{\gamma - 1}{2} M^2\right)^{\frac{1}{\gamma - 1}} = 1.088 \tag{5.20}$$

$$\frac{T_0}{T_2} = 1 + \frac{\gamma - 1}{2} M^2 = 1.034 \tag{5.21}$$

$$\frac{p_{atm_0}}{p_{atm_2}} = \left(1 + \frac{\gamma - 1}{2} M^2\right)^{\frac{\gamma}{\gamma - 1}} = 1.126 \tag{5.22}$$

It should be noted that assumption of constant Mach number after shockwave was made and that in above equations γ of 1.4 was chosen. Final ratios required in order to find atmospheric properties at the stagnation point: $p_0/p_1 = 32.654$, $\rho_0/\rho_1 = 5.44$ and $T_0/T_1 = 5.9972$; where index 1 and 0 represent conditions before normal shock wave and at body's stagnation point respectively. DBD plasma actuator will be placed very close to stagnation point, so it is safe to assume that it will experience very similar conditions as ones present in the stagnation point. Modified values are presented in Table 5.4.

Table 5.4: Dependent model parameters after normal shockwave

$H\ (km)$	$\rho\ (kg/m^3)$	$\lambda\ (m)$	$T\ (K)$	$p\ (mmHg)$	$\mu\ (kg/ms)$	$n_a\ (1/m^3)$
10	1.6581	$3.7719 * 10^{-8}$	1338.575	6490.505	$4.927 * 10^{-5}$	$5.34565 * 10^{24}$
20	0.5097	$1.7551 * 10^{-7}$	1299.593	1354.194	$4.849 * 10^{-5}$	$1.7237 * 10^{24}$
30	0.09776	$8.4384 * 10^{-7}$	1358.366	294.408	$4.967 * 10^{-5}$	$3.1508 * 10^{23}$
40	0.02187	$3.8399 * 10^{-6}$	1501.099	71.479	$5.271 * 10^{-5}$	$6.5325 * 10^{22}$
50	0.00572	$1.5185 * 10^{-5}$	1622.842	19.527	$5.498 * 10^{-5}$	$1.859 * 10^{22}$

It should be noted that λ, the mean free path had to be computed again, due to new values of pressures and temperatures. For this Equation 4.1 was used. An assumption was made that the number of constituents do not change over normal shock wave.

Unfortunately assumption to keep power supply same as used by [Pereira, 2016] give unrealistic values of produced actuator force for altitudes above 10 km. This being a simple model, it does not take into account reversal flow (velocities in opposite direction), which are created due to extrapolated values of E/p_0. This resulted in a new assumption, that drift velocity and ionization rate stays constant across all altitudes, thus same as in Figure 5.5. To achieve this E/p_0 ratio would have to be constant. As pressure is decreasing with altitude, electric field strength to DBD actuator would have to decrease as well, making power subsystem mass lower. This is very desirable in space-based systems as lower mass would imply lower costs, but as this is a first order feasibility study, this benefit will not be quantified.

5.2.2 Model extension results

Model results for altitudes of 10, 20, 30, 40 and 50 km can be found in Figure 5.12. Figure below represents modelled actuator ($\overrightarrow{F}_{act}$), load cell ($\overrightarrow{F}_{LC}$) and change in friction ($\Delta\overrightarrow{F}_{wall}$) forces over range of free stream velocities for both co-flow and counter-flow configurations. When these are compared with Figure 5.6, one can observe same trends. At an altitude of 10 km, actuator is able to produce higher force for both configurations than at sea level calculated by [Pereira, 2016]. This result was expected under stated conditions, that is actuator placed in M=5 flow and behind normal shock wave. As it can be seen from Table 5.4, atmospheric conditions (density, pressure and temperature) behind shock are higher than one at sea level. Denser atmosphere means that there will be more molecules that exchange momentum.

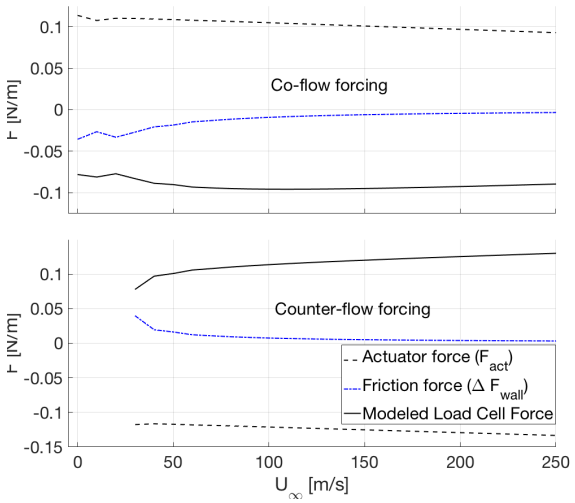

(a) H = 10 km

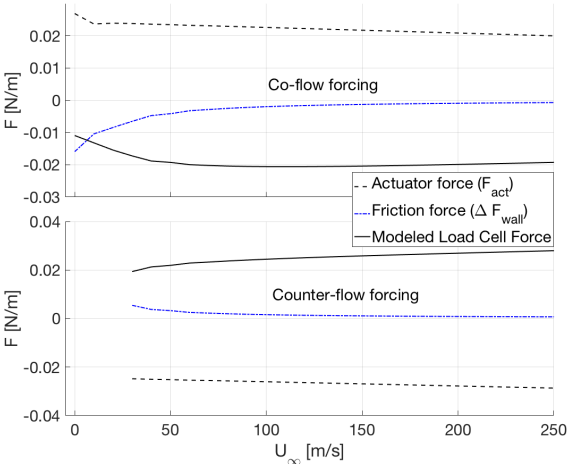

(b) H = 20 km

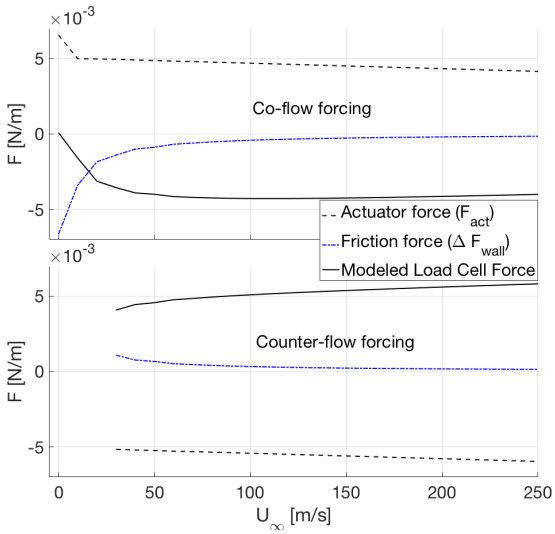

(c) H = 30 km

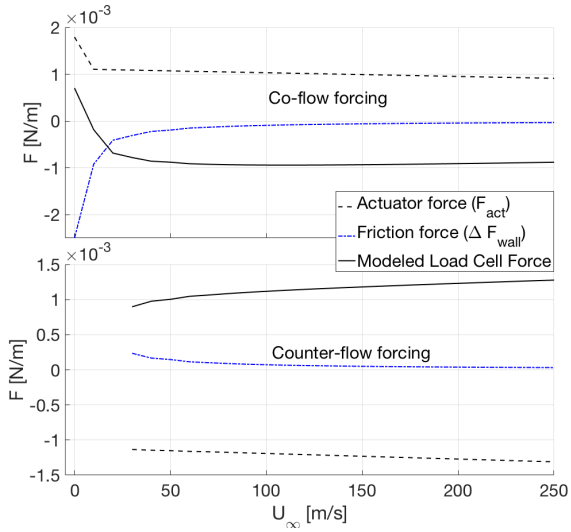

(d) H = 40 km

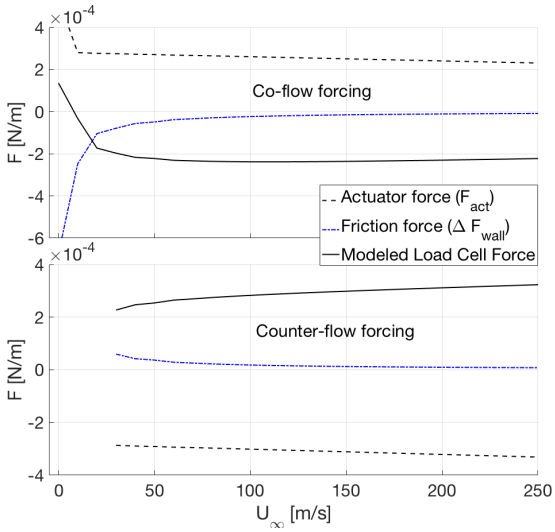

(e) H = 50 km

Figure 5.12: Modelled results for DBD actuator forcing in both configurations for different altitudes

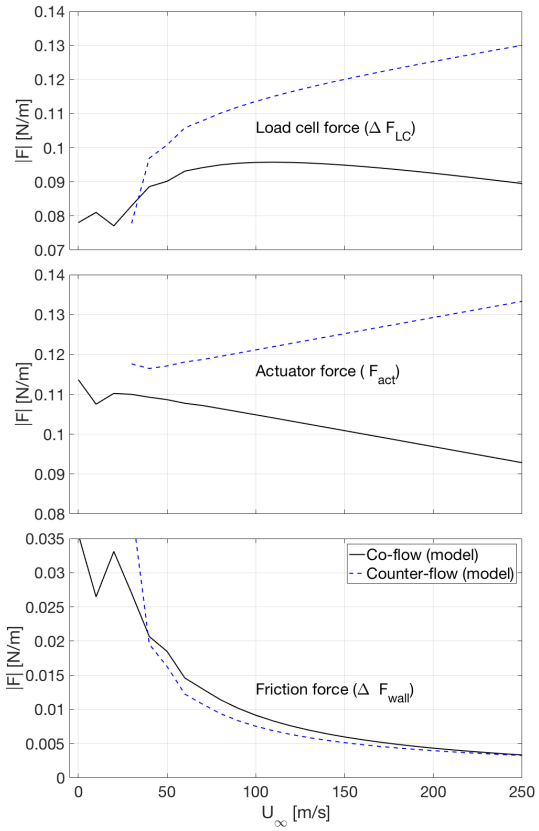

(a) H = 10 km

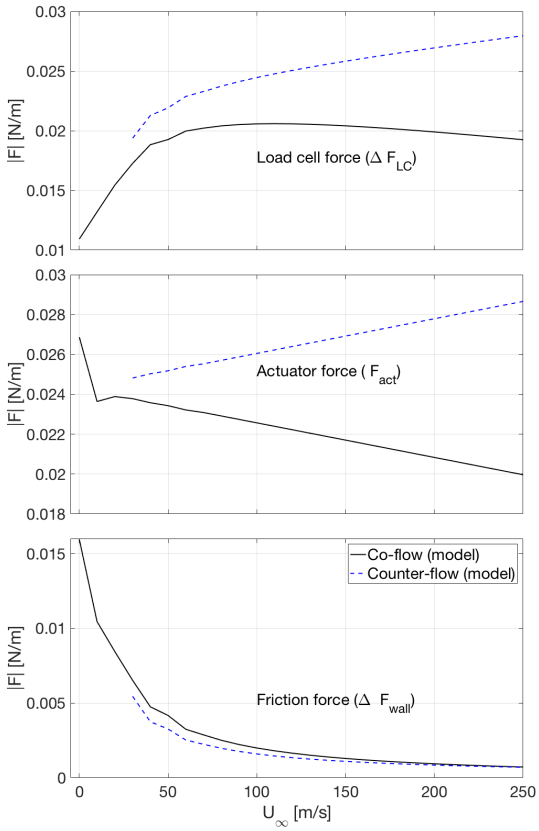

(b) H = 20 km

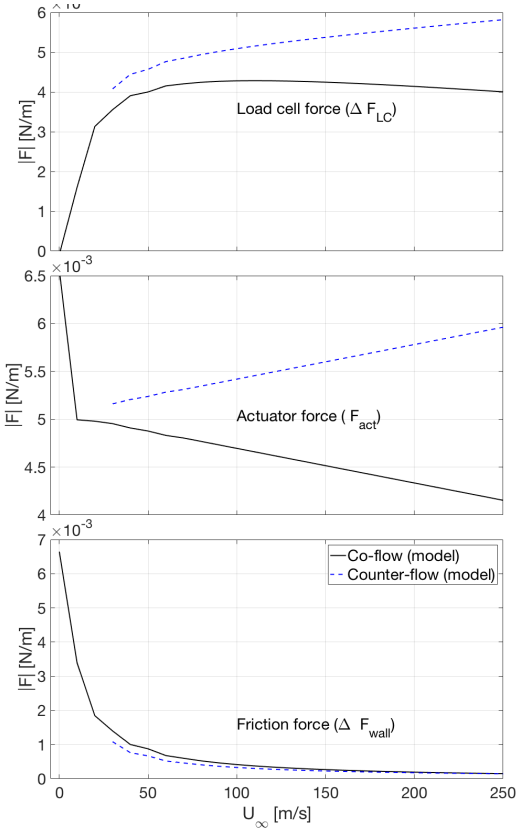

(c) H = 30 km

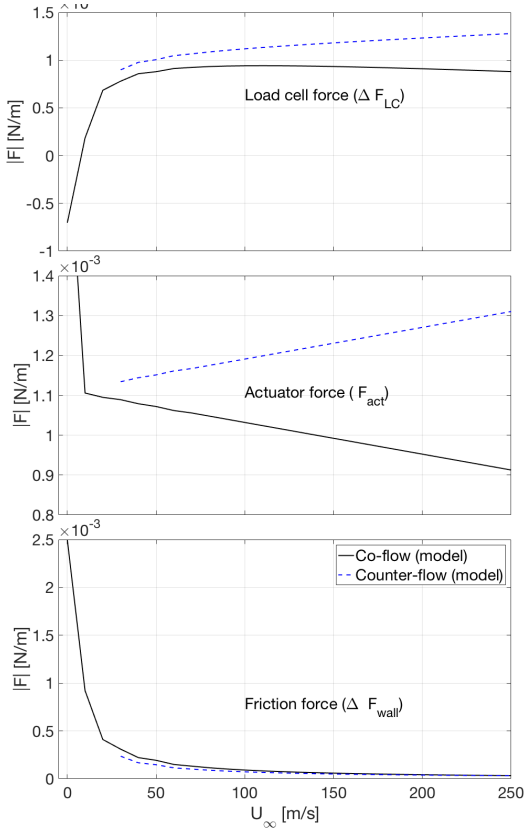

(d) H = 40 km

Figure 5.13: Modelled results for an individual absolute force terms in co-flow and counter-flow configurations for different altitudes (**load cell force top axis in (c) and (d) goes to** $6 * 10^{-3}$ **and** $1.5 * 10^{-3}$ **respectively**)

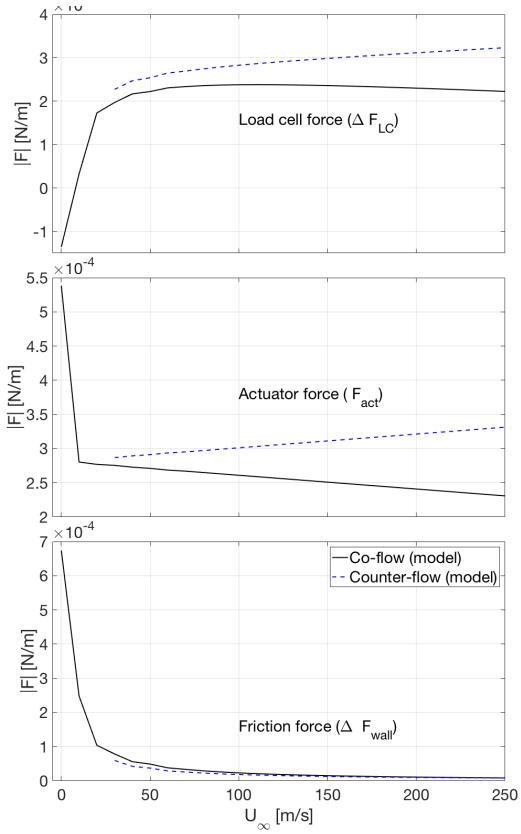

Figure 5.14: Modelled results for an individual absolute force terms in co-flow and counter flow configurations at an altitude of 50 km (**load cell force top axis goes to** $4 * 10^{-4}$)

Figures 5.13 and 5.14 represent results of an individual absolute force terms for both configurations. Similar to [Pereira, 2016] finding, due to incompressibility effects reason behind forcing behavior at higher external flow velocities is unclear and requires additional research.
If the measured load cell forces for an external flow velocity of 50 m/s is compared across altitudes, it can be seen that force scales down with altitude. Approximated values of forces and altitudes for both co-flow and counter-flow configurations are presented in Table 5.5.

Table 5.5: Absolute modelled load cell forces computed at $U_\infty = 50\ m/s$

H (km)	Co-flow	Counter-flow
10	0.09	0.1
20	0.019	0.022
30	$4 * 10^{-3}$	$4.6 * 10^{-3}$
40	$0.9 * 10^{-3}$	$1 * 10^{-3}$
50	$2.2 * 10^{-4}$	$2.6 * 10^{-4}$

Table 5.5 shows that DBD plasma actuator's modelled load cell force drops on average 4.51 and 4.44 times per 10 km altitude for co-flow and counter-flow configurations respectively. This can be used for first order force estimation for even higher altitudes. However one should always consult assumptions made, as one of them assumes E/p_0 ratio to be constant meaning that ion drift velocity and fraction of ionized atoms stay

constant with a function of altitude. This could only be possible under certain condition, which would require change of power supply as a function of reduction in pressure.

5.3 Chapter Conclusions

Goal of this chapter was to estimate altitude effects on operational performances of DBD plasma actuators. In order to do this an existing model made by [Pereira, 2016] was modified. Author's simple analytical model estimates impact of external flow velocity on the transfered momentum created by DBD actuator positioned both in co-flow and counter-flow configurations for sea level conditions. Model made by [Pereira, 2016] is valid under following major assumptions:

- Flow is considered incompressible meaning that external flow velocity shall not exceed Mach numbers higher than 0.3.
- Impermeability of the wall.
- Atmosphere at which actuator is operated composes of two most common molecules, namely 79% N_2 and 21% O_2.
- Momentum of the ionized species is transferred to neutral particles through numerous collisions in a way that velocity after momentum transfer, is the same for all molecules across each divided fluid element.
- During momentum transfer estimation no distinction is made between negative ions, free radicals and positive ions.
- In order to compute wall shear stresses at wall surface and top of the fluid element author makes a first order approximation meaning that the gradient of velocity normal to the wall is estimated using average velocity on the element at the representative height.

Author found that at sea level conditions, estimated load cell force increases with increase in external flow velocity. [Pereira, 2016] also found that higher force is measured in counter-flow forcing, and is nearly constant.

In order to extend model, one more assumption had to be made. Last major assumption is that the electric field strength to external pressure ratio (E/p_0) stays constant. This assumption had to be made in order to keep scope of this research manageable and concentrated to questions from Chapter 1. In order to keep this assumption valid, power supply of the actuator system had to be variable. This means that with decrease in altitude, electric field strength would also has to decrease. Extended model showed that under stated assumptions all forces modeled have same trend as estimated by [Pereira, 2016]. Another found result is that load cell force for external flow velocity of 50 m/s scales down for an average value of 4.51 and 4.44 times per 10 km altitude for co-flow and counter-flow configurations respectively. These load cell force scaling factors could be roughly explained by their linear dependence with density, which on average scales down for 4.19 each 10 km. Due to numerous assumptions made, this phenomenon requires addition research.

6 PROOF OF SPACE-BASED APPLICATION

Goal of this chapter is to suggest possible application of DBD plasma actuator in conditions related to space-based systems. This is done in order to show that spacecraft steering is possible with use of simple DBD actuators. In order to do this, a list below combines findings from previous chapters:

- Chapter 2 gave an insight into two different plasma actuators, namely corona discharge and DBD plasma actuators. Due to several beneficial reasons and available model and equipment it was decided to concentrate on **DBD actuator type**.
- Space-based systems are almost always related to high speed flow. Due to this reason research on possible usage of DBD and other actuators was conducted in Chapter 3. As a result of high temperatures occurring at stagnation point and related molecular dissociation, it was decided to keep **Mach number lower than 5.5**.
- Research made by [Nishihara et al., 2011] mentioned in Section 3.3 showed possible application. As previously stated authors used DBD actuator close to stagnation point in order to introduce compression wave that interacted with baseline shock wave. Figure 3.5 shows that due to mentioned interaction, relative shock stand-off distance changes for up **25%**.
- Chapter 4 models all relevant atmospheric conditions as a function of altitude that will be used to define DBD actuator operating parameters.
- Once flow field Mach number was limited to $\mathbf{M_\infty}$**=5**, existing model made by [Pereira, 2016] was modified. In Chapter 5 altitude limit of $\mathbf{H}_{max}$**=50 km**, specific heat constant of γ=1.4 and spherical body shape with radius of **R=1 m** were defined. Under certain conditions and assumptions actuator is capable of producing force at altitude of 50 km.

The most relevant application parameters are bold in list above, while rest can be found in mentioned chapters. Following section is going to relate increase in shock stand-off distance to pressure on circular cylinder (spherical body in 2D).

6.1 Shock Stand-Off Distance Approximation

Calculation of shock stand-off distance is going to be performed using approximation made by [Sinclair and Cui, 2017]. This study is based on Newtonian impact theory, it is approximated by free-stream Mach number and location of the point on body where M=1 (sonic point). When authors compared modeled with experimental results made by [Kaattari, 1961], [Chul-Soo, 1956] and [Alperin, 1950], they were almost identical. Geometry, sonic point coordinates and shock parameters used in [Sinclair and Cui, 2017] study are presented in Figure 6.1. According to the authors the shock stand-off distance can be found using Equation 6.1.

$$\delta = \frac{\beta_s^2}{\theta_s^2 cos\beta_s} \cdot \sqrt{\frac{2+(\gamma-1)M_\infty^2}{2\gamma M_\infty^2 - \gamma + 1}} \tag{6.1}$$

Where:

β_s is angle between free stream vector and sonic stream tube as defined in Figure 6.1 (b)

θ_s is angle defined by: $\theta_s = \frac{\pi}{2} - \beta_s$

γ is specific heat constant defined in Section 5

M_∞ is free stream Mach number, before normal shockwave: $M = 5$

[Sinclair and Cui, 2017] state that Equation 6.1 is valid under the assumption that Mach number remains constant between shockwave and surface of cylindrical body. Authors also state that above *"equation is already non-dimensionalized by radius $R = 1$" [Sinclair and Cui, 2017].* This fits perfectly together with exactly same assumptions made in Section 5.

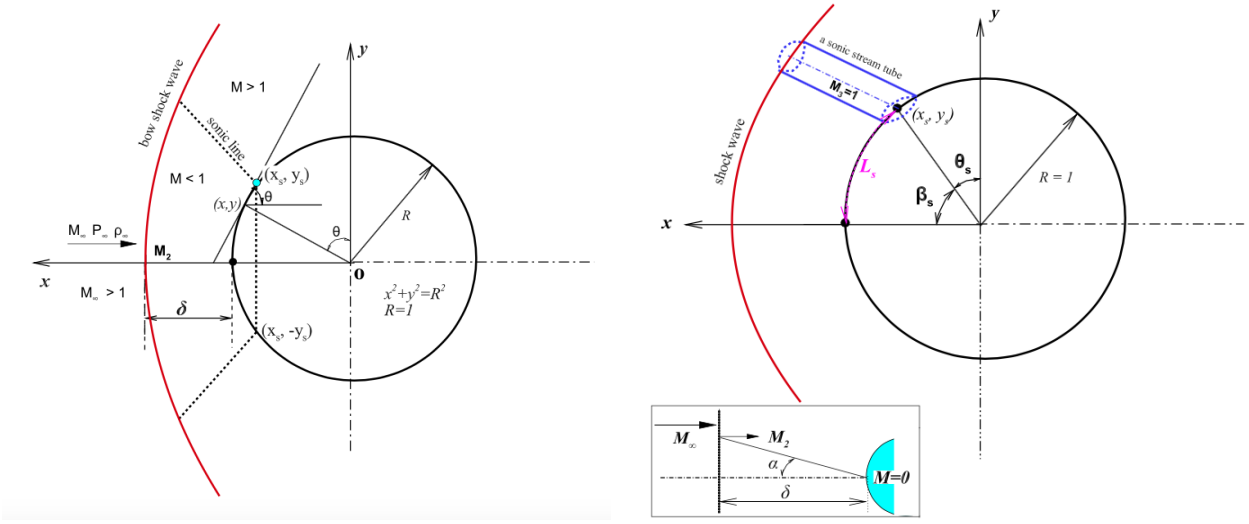

(a) (b)

Figure 6.1: (a) flow field geometry and (b) sonic point location schematic [Sinclair and Cui, 2017]

In order to find β_s angle authors use Equation 6.2.

$$\beta_s = \frac{\pi}{2} - sin^{-1}\sqrt{\frac{C_{ps}}{C_{p,max}}} \tag{6.2}$$

Where:

C_{ps} is pressure coefficient at coordinates (x_s, y_s) defined in Figure 6.1 (b)

$C_{p,max}$ is maximum pressure coefficient at stagnation point ($\beta_s = 0$)

Sonic C_{ps} and maximum $C_{p,max}$ pressure coefficients can be found using equations 6.3 and 6.4 respectively. Both equations depend on only two parameters, namely γ and M_∞.

$$C_{ps} = \frac{2}{\gamma M_\infty^2}\left\{\left(\frac{\gamma+1}{2}\right)^{-\frac{\gamma}{\gamma-1}}\left[\frac{(\gamma+1)^2 M_\infty^2}{4\gamma M_\infty^2 - 2(\gamma-1)}\right]^{\frac{\gamma}{\gamma-1}} \times \left[\frac{1-\gamma+2\gamma M_\infty^2}{\gamma+1}\right] - 1\right\} \tag{6.3}$$

$$C_{p,max} = \frac{2}{\gamma M_\infty^2}\left\{\left[\frac{(\gamma+1)^2 M_\infty^2}{4\gamma M_\infty^2 - 2(\gamma-1)}\right]^{\frac{\gamma}{\gamma-1}} \times \left[\frac{1-\gamma+2\gamma M_\infty^2}{\gamma+1}\right] - 1\right\} \tag{6.4}$$

To find pressure coefficient at any part of the body Equation 6.5 can be used. In it only unknown is θ, which is the angle of the body surface tangent to the free stream direction as defined in Figure 6.1 (a).

$$C_p = C_{p,max} sin^2\theta \tag{6.5}$$

Relation between pressure coefficient and pressure value on the surface of a cylindrical body is given by Equation 6.6.

$$C_p = \frac{2}{\gamma M_\infty^2}\left(\frac{p}{p_\infty} - 1\right) \tag{6.6}$$

Combining equations 6.5 and 6.6 a relation for pressure values is obtained and presented as Equation 6.7.

$$p = p_\infty\left(\frac{C_{p,max} sin^2\theta M_\infty^2 \gamma}{2} + 1\right) \tag{6.7}$$

6.2 Implications Related To Change In Shock Stand-Off Distance

In order to determine what are the implications due to change in shock stand of distance by 25% sonic line will be used. At sonic line flow field impinging surface has Mach number M = 1. Using conditions listed above, for an altitude of 50 km, knowledge of shock stand-off distance increase as computed by [Nishihara et al., 2011] and iterative process; it was found that pressure at coordinates (x_s,y_s) decreases for 55.62% of the original value. This clearly shows that increase of δ has large influence on pressure at surface of cylindrical sphere. Pressure distribution before DBD actuator operation can be seen in Figure 6.2.

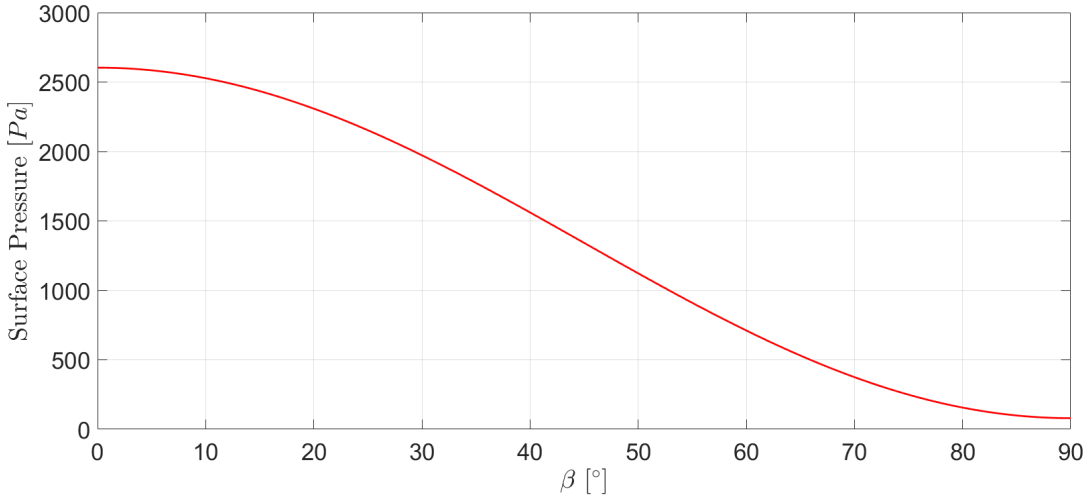

Figure 6.2: Pressure distribution for quarter cylinder before DBD actuation

Figure 6.2 shows pressure distribution starting from stagnation point until top or bottom cylindrical parts (as zero angle of attack was assumed) that are 90° from stagnation line. Highest modeled pressure is at the stagnation point and equals 2603.5 Pa. This value is matches stagnation pressure value obtained in Section

5.2. It should be noted that model made by [Sinclair and Cui, 2017] does not consider compressibility effect after normal shockwave, but takes isentropic flow relations, same as assumed in Section 5.2.

By appropriate actuator placement, pressure distribution from Figure 6.2 could be modified for up to 55.62%. This is a promising result that could be used for spacecraft steering applications. When more information on dimensions and mission profile are known, a deeper analysis of this theory shall be performed.

7 ACTUATOR MATERIAL AND BONDING QUALIFICATION

In order apply DBD plasma actuator on space-based system investigation on actuator's components behavior under harsh environmental conditions shall be done. First investigated aspect is thermal cycling expected to occur during orbit phase of spacecraft's life. Vacuum environment means that there is no atmosphere to shield spacecraft from incoming Sun's energy flux. This means that during one orbit large temperature difference will occur between cases when spacecraft is exposed to Sun or behind Earth in its shade. To compute thermal Von Misses stresses and maximum deflections expected to occur in actuator, a parametric model is made. In second part of this chapter experimental test is proposed in order to validate parametric model and qualify various dielectric materials bonded with two different room temperature curing adhesives. Model and qualification test will provide next step in creating space-based application of DBD actuators as they will give definite results concerning components survivability during spacecraft orbiting phase.

7.1 Modeling

The first step in modeling of thermal cycling effect on DBD plasma actuator is to define cycling conditions, actuator's dimensions and materials it's made of. These parameters will be put into academic version of ANSYS R16.1 and using transient analysis Von Misses stresses and maximum deflections will be computed. ANSYS is finite element method program used for modeling of stresses in structures. Thermal loads are result of different coefficients of thermal expansion that components making DBD actuator have. As temperature increases or decreases, each component expands or shrinks at different rates due to dissimilar coefficients of thermal expansion. Stresses will occur as a result of different expansion rates and rigid bond connections between actuator components.

7.1.1 Definition of thermal cycling conditions

In order to define thermal cycling conditions, reference on typical temperature maxima and minima had to be found. [Fatemi et al., 2013] conduced research in which flush mounted solar panels for space missions were qualified and produced. In it, different temperature extremes were defined for various orbital altitudes. For Geostationary Equatorial Orbit (GEO) application typical temperature range is from -170°C to +145°C and for Low Earth Orbit (LEO) temperature range is from -125°C to +125°C. According to previous chapters it was found that currently DBD actuator could not be operated at altitudes above 50 km. Hence this thesis considers DBD actuator operation during launch or re-entry flight phases. Apart from Apollo program no spacecraft was orbiting at GEO or higher orbit and returned back to Earth due to large distance and ΔV needed for re-entry. Thus all satellites orbiting at GEO altitude at the end of their life are sent to graveyard orbit located at higher altitude than GEO. Due to these reasons, modelling below will be conducted for satellite orbiting at LEO orbit. Roughly 10% margin is added to temperature extremes defined by [Fatemi et al., 2013] in order to produce more redundant model and results. This means that temperature range for proceeding model will be from -140°C to +140°C.

7.1.2 Actuator dimensions and materials

Initial idea was to use actuator materials and dimensions as proposed by [Pereira, 2016] in his research. Reason for this, is that both model and physical actuator already exist in-house, making experimental testing less expensive. During preliminary analysis, it was found that some parameters and materials had to be modified in order not to reach any yield strength values. If any material reaches its Von Misses yield strength, it will plastically deform, meaning that it will never return to original shape it had before stress was applied. Complete overview of all materials and their mechanical and thermal properties can be seen in Table 7.1.

First change concerns shape of the dielectric material. As complete actuator will be flush mounted to spacecraft it has to be inserted in it, meaning that any corner will present itself as stress concentration due to different expansion rates between aluminum spacecraft surface and dielectric material. Chosen dielectric shape is ellipsoid, together with spacecraft's surface and electrodes is presented in Figure 7.1. Dielectric material is depicted as transparent in order to show both air exposed and immersed electrodes. Electrodes are kept the same size as defined by [Pereira, 2016]. In his research author states that electrodes are made of copper but does not state their mechanical properties, which depend on alloy used and method of production. If annealed copper is used, it has very low yield strength ($\sigma_y = 33.3$ MPa) so under thermal stresses corresponding to LEO it will yield. In order improve electrode's mechanical properties copper which is produced using cold drawn method is selected.

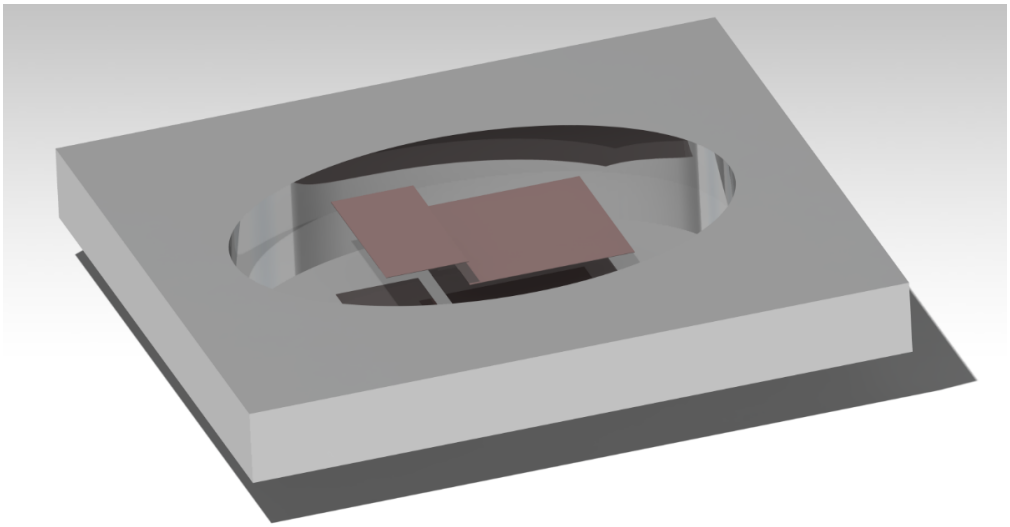

Figure 7.1: DBD actuator design used for ANSYS

If modeled actuator is compared to one used by [Pereira, 2016] one more modification is made. Namely PMMA dielectric material is exchanged with Lexan FR as it has lower coefficient of thermal expansion. According to manufacturers Lexan FR has coefficient of thermal expansion of 5.8 [SABIC Lexan, 2009], while original PMMA has coefficient equal to 7, which is about 20% higher. Both materials have similar mass density and yield strength.

Table 7.1: Mechanical and thermal properties required for analysis

Material	Yield Strength (MPa)	Coefficient of thermal expansion (x10^{-5} 1/°C)
Annealed Copper	33.3	1.64 @ $20 < T < 100$ °C and 1.85 @ $T = 250$ °C
Cold Drawn Copper	333.4	1.64 @ $20 < T < 100$ °C and 1.85 @ $T = 250$ °C
PMMA	70	7
Lexan FR	70	5.8
Aluminium 6061-T6	276	2.3

7.1.3 Model results

Using dimensions defined earlier, Computer Aided Design (CAD) drawing was made using CATIA. Drawing and material parameters defined as in Table 7.1 were put into ANSYS. Grid was defined iteratively so that the maximum amount of data points do not exceed 30000 limited due to tool's academic version. Finally transient analysis was be performed for two cases starting at 22 °C and finishing at +140 °C and -140 °C. After analysis actuator, stresses in separate parts are presented in proceeding figures.

Stresses in aluminum sheet are presented in Figure 7.2. It shows that the stresses are highest at tips of the oval edge, where radius of curvature is the lowest. As expected stresses are higher for case where complete system reaches -140°C, as ΔT is higher for 40°C. Both obtained maximum Von Misses stress values (124.3 and 170.6 MPa) are lower than Aluminum 6061-T6 material yield strength (276 MPa), meaning that spacecraft surface sheet will not plastically deform.

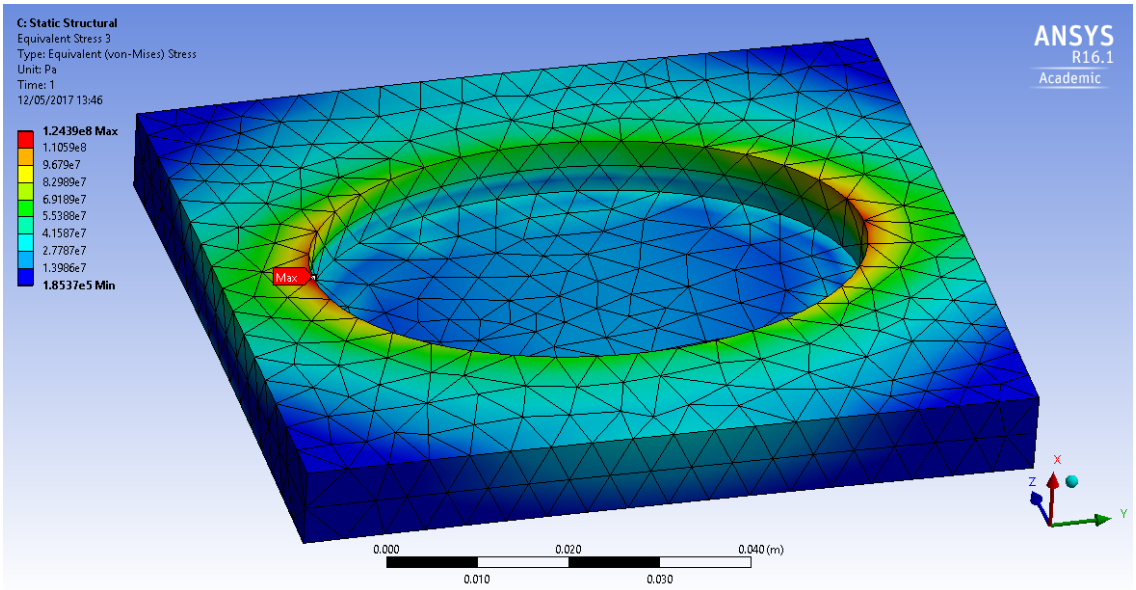

(a)

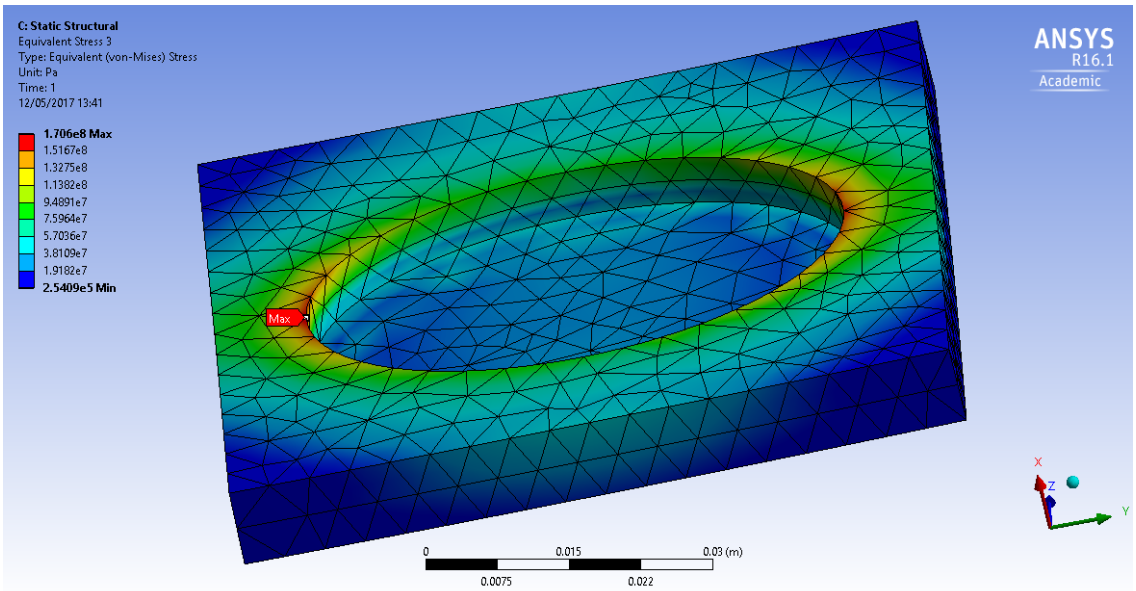

(b)

Figure 7.2: Von Misses stresses occurring in aluminum sheet - spacecraft surface insert hole at (a) +140 °C and (b) -140 °C

Stresses that occur in air-exposed electrode are presented in Figure 7.3. It is clear that the highest stress occurs at the electrode edge with values of 221.36 MPa and 314 MPa for +140 °C and -140 °C cases respectively. Using Table 7.1 it can be seen that if annealed copper is used, electrode will yield and deform. As electrode shall retain its original size and shape it is desirable to use cold drawn copper. In this way it is certain that no plastic deformation will occur, due to high cold drawn copper's yield strength of 333.4 MPa.

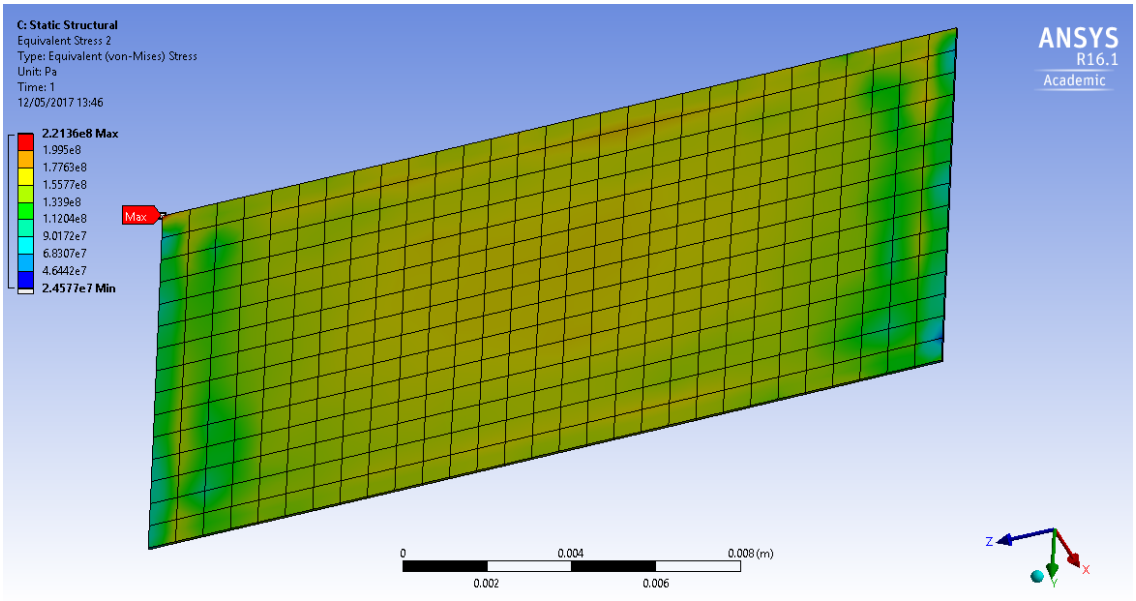

(a)

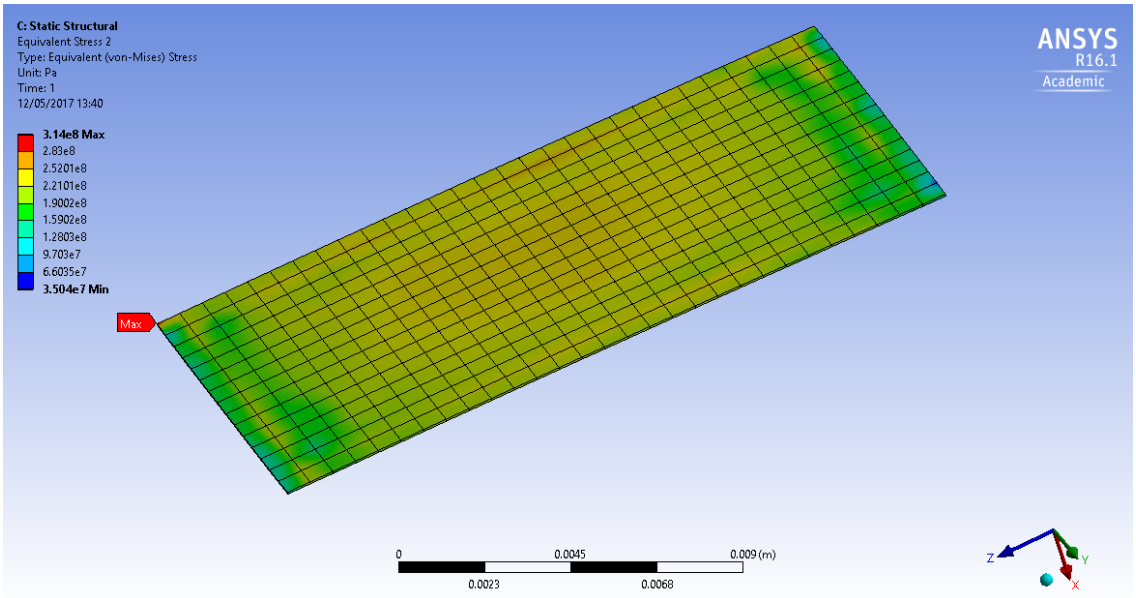

(b)

Figure 7.3: Von Misses stresses occurring in top air exposed electrode at (a) +140 °C and (b) -140 °C

Similarly to top electrode, stresses in an immersed electrode are presented in Figure 7.4. As stresses calculated for this electrode are lower than ones occurring at air exposed, it is safe to assume that cold drawn copper electrode is more than safe material choice.

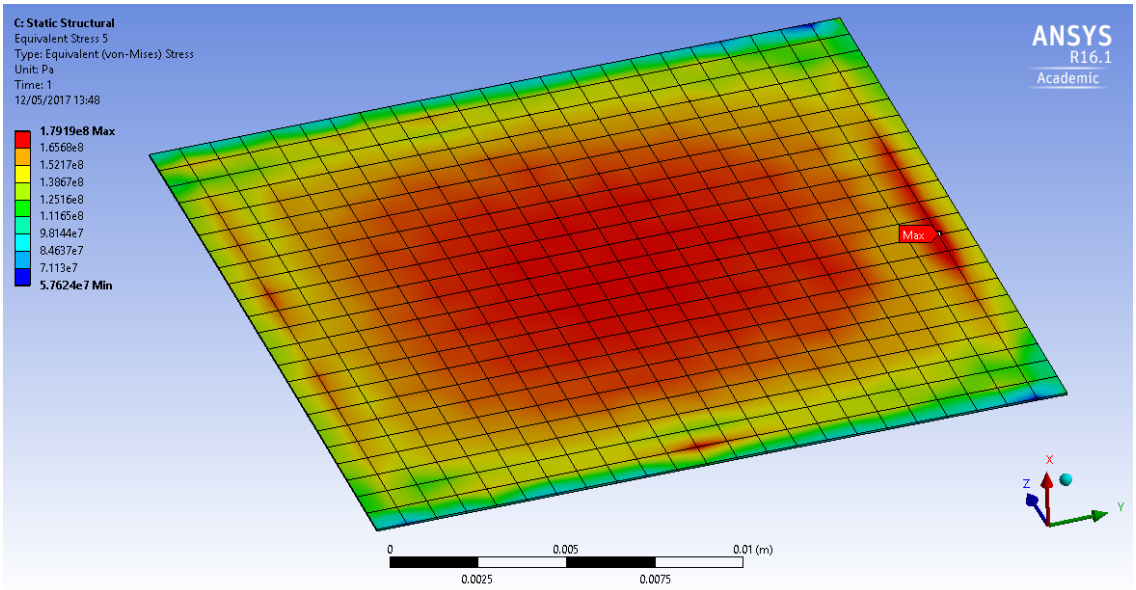

(a)

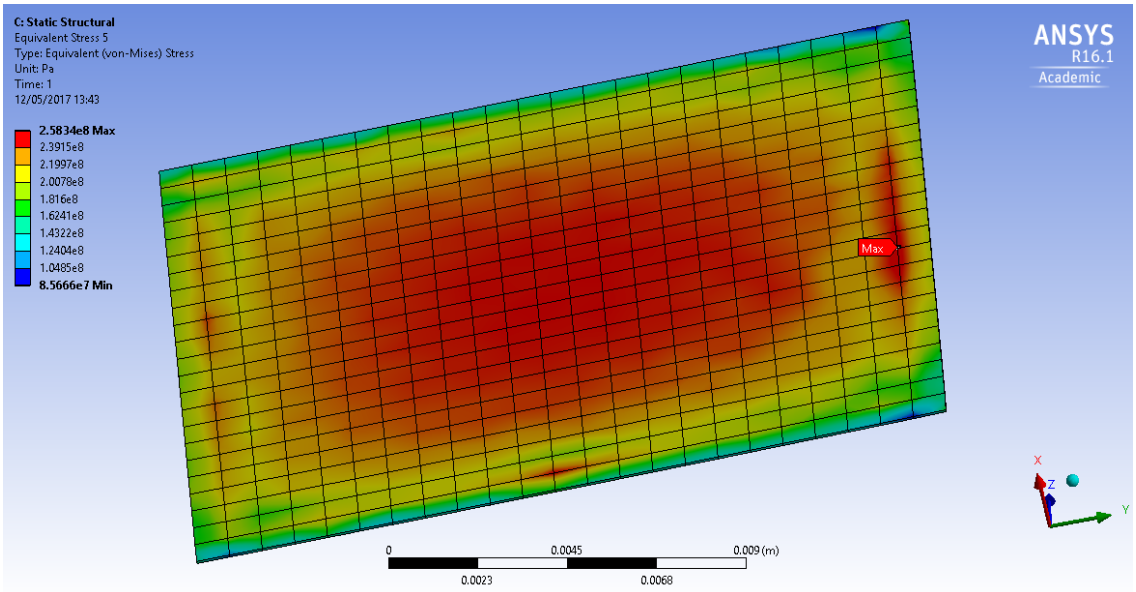

(b)

Figure 7.4: Von Misses stresses occurring in an immersed electrode at (a) +140 °C and (b) -140 °C

Dielectric material shall be composed of two parts, in order to simplify manufacturing efforts. Bottom electrode shall be shielded from air exposed and will be positioned in pre-made cut-out in bottom part of dielectric. Half of dielectric separating two electrodes is called top dielectric layer, and second position under immersed electrode is called bottom dielectric layer. Stresses in top and bottom layers are presented in Figure 7.5 and Figure 7.6 respectively. As earlier stated when PMMA was used, stresses in top dielectric exceeded 70 MPa, thus by use Lexan FR instead of PMMA lower stresses are obtained due to lesser difference in thermal expansion coefficients between dielectric and spacecraft's surface.

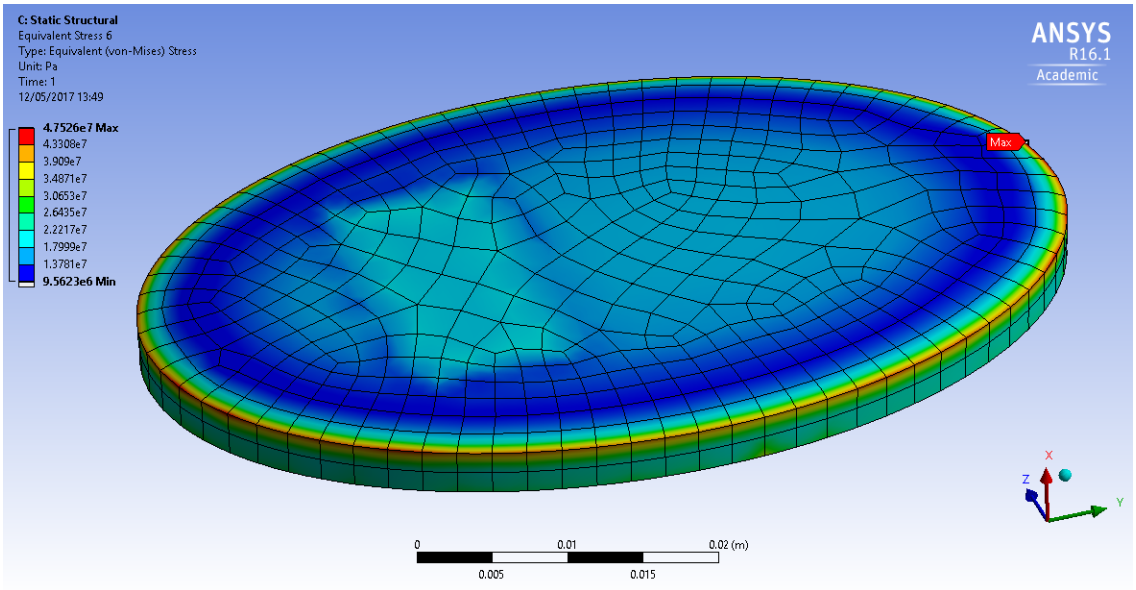

(a)

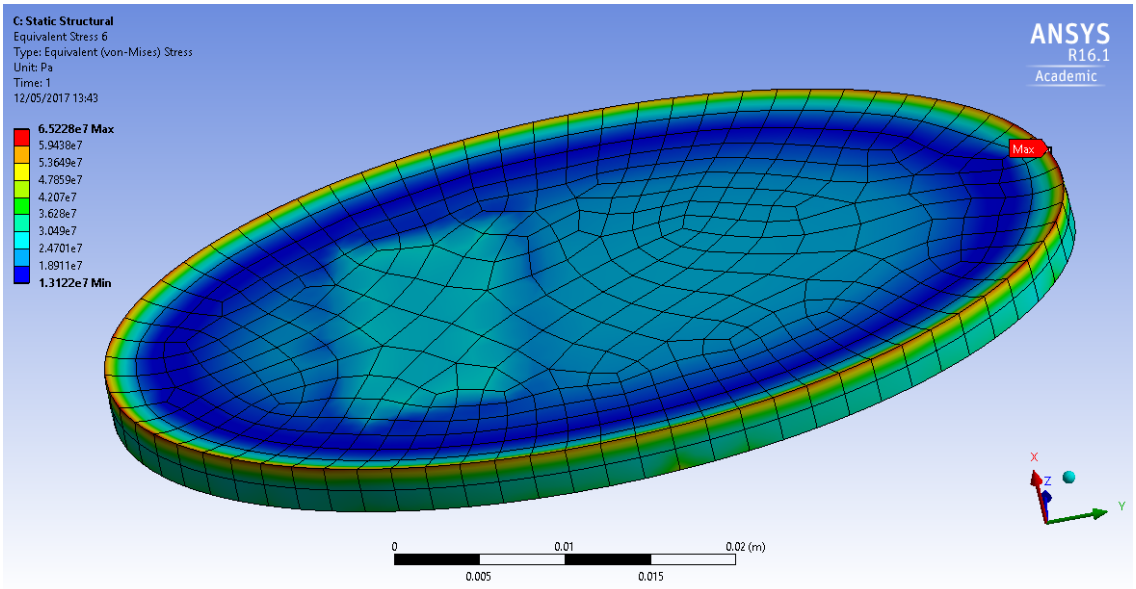

(b)

Figure 7.5: Von Misses stresses occurring in top dielectric layer at (a) +140 °C and (b) -140 °C

Both figures 7.5 and 7.6 show that stresses due to thermal gradients do not exceed yield stress of Lexan FR material.

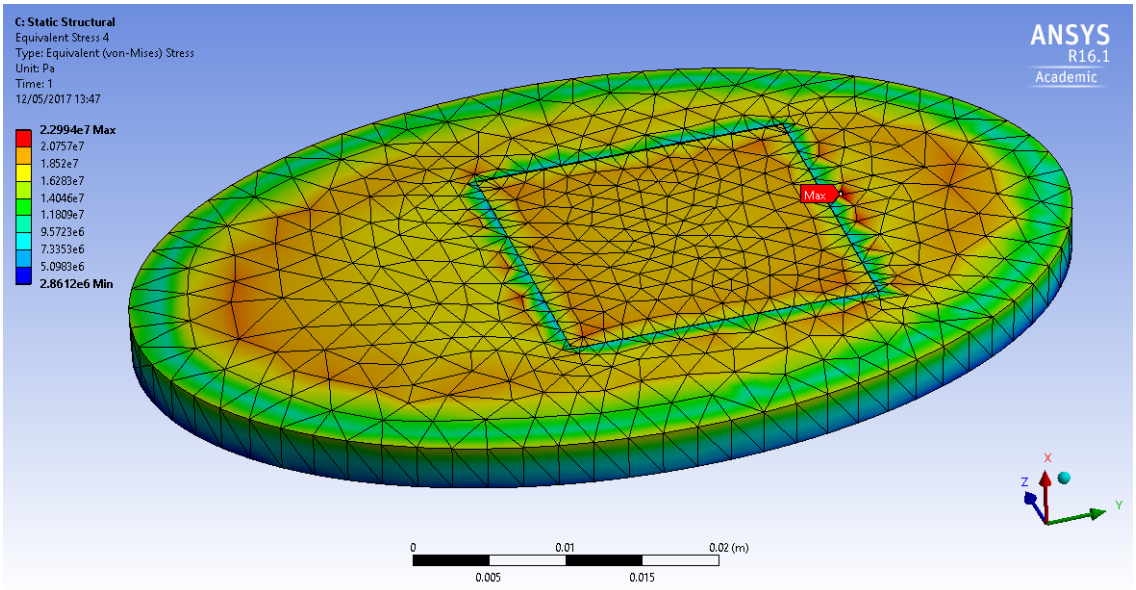

(a)

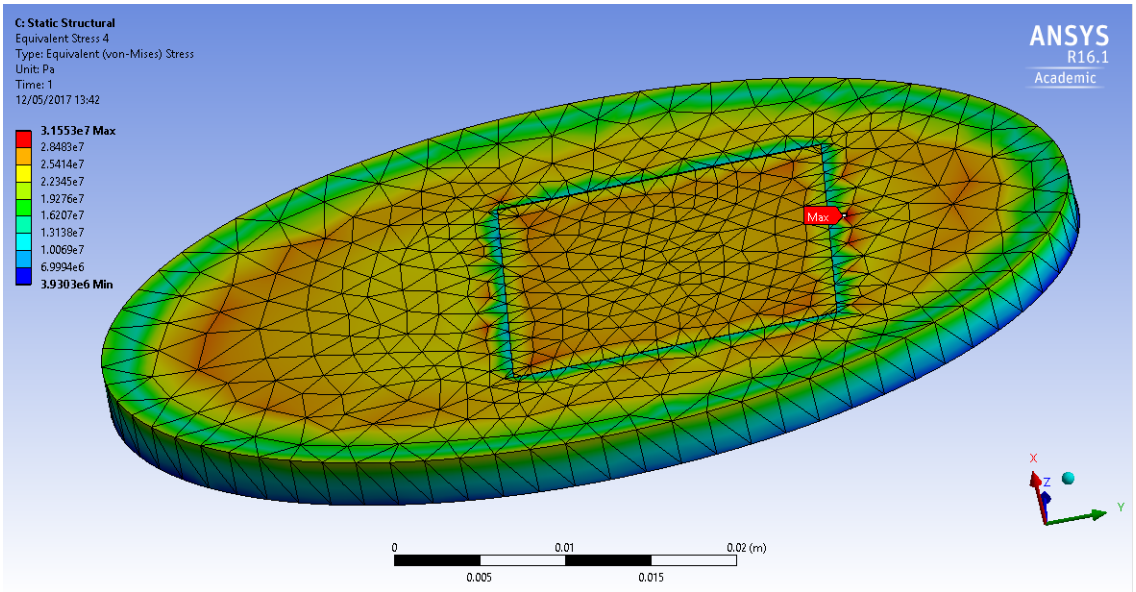

(b)

Figure 7.6: Von Misses stresses occurring in bottom dielectric layer at (a) +140 °C and (b) -140 °C

Finally deflections occurring due to thermal stresses are presented in Figure 7.7. Effect of temperature can clearly be seen as dielectric expands in +140 °C, and contracts in -140 °C case. Highest deflections of 0.2 mm and 0.27 mm can be seen at the edges of aluminum sheet for positive and negative extreme temperatures respectively.

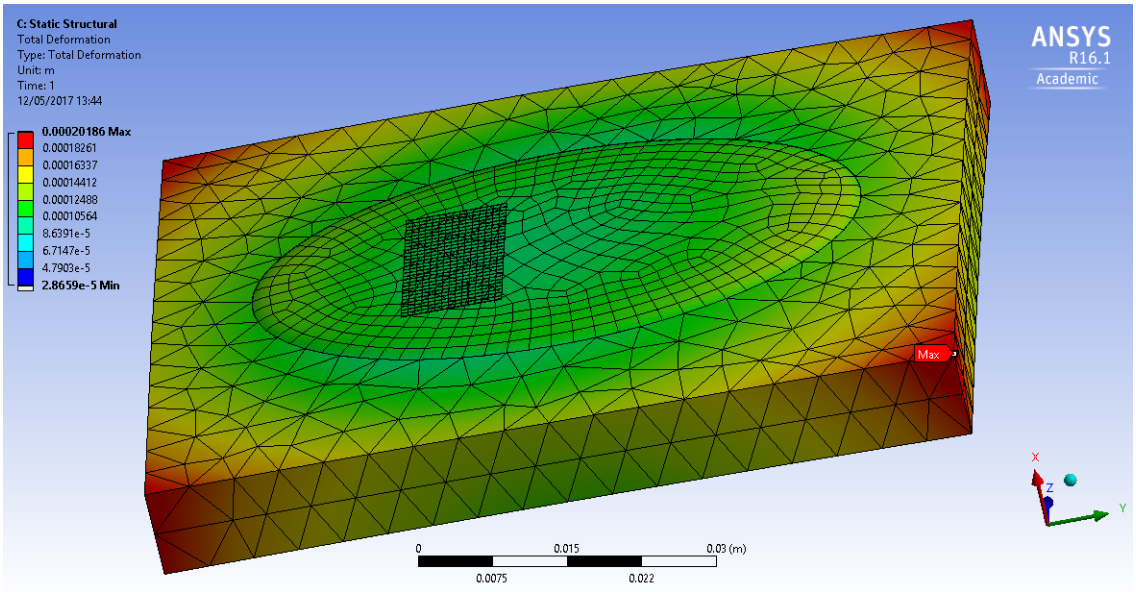

(a)

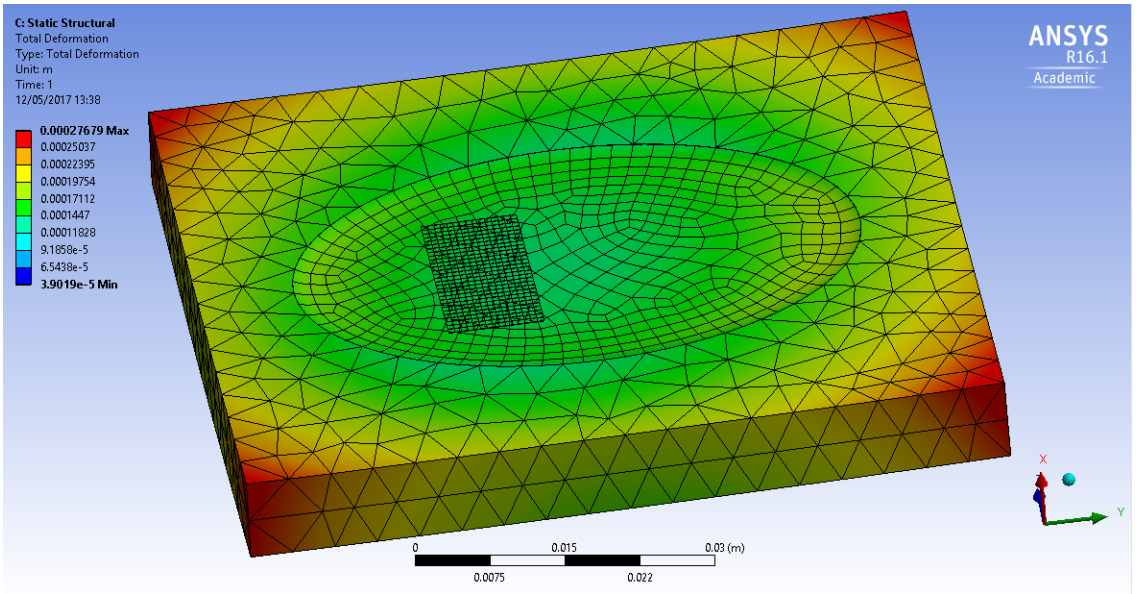

(b)

Figure 7.7: Actuator deflections occurring at (a) +140 °C and (b) -140 °C

Table 7.2: Summary of parts, materials and stresses occurring at two temperature extremes

Actuator Part	Material	Yield Strength (MPa)	Stress at +140 °C (MPa)	Stress at -140 °C (MPa)
Spacecraft Surface	Al 6061-T6	276	124.39	170.6
Air exposed Electrode	Cold Drawn Copper	333.4	221.36	314
Immersed Electrode	Cold Drawn Copper	333.4	179.19	258.34
Top Dielectric Part	Lexan FR	70	47.526	65.228
Bottom Dielectric Part	Lexan FR	70	22.994	31.553

To summaries all stresses per actuator part with their corresponding material and yield strengths are presented in Table 7.2. It shows that none of components comprising DBD actuator yield due to temperature gradients occurring during orbit phase of spacecraft's life. Knowing this one may proceed to Section 7.2 where test is proposed in order to qualify bonding of dielectric layer. As testing of single material, namely Lexan, would not be cost effective due to small physical size of test sample in comparison with thermal vacuum chamber, other dielectric materials shall be tested. In this way Aerospace Faculty would obtain large data bank and qualified numerous dielectric materials and adhesives for small increase in cost, as contributions from facilities and manpower many time exceed cost of raw materials.

7.2 Testing

If it is desired to use DBD plasma actuator during re-entry phase it must survive thermal loads that will occur during spacecraft's orbit. Hence the following section contains information, which defines test procedures and materials needed in order to qualify actuators with various dielectrics and adhesives. After qualification it will be certain that DBD actuator will withstand all thermal loads and be able to operate during re-entry.

7.2.1 Materials and Equipment

All needed equipment and materials are specified in tables 7.4 and 7.3 respectively. Equipment list is missing identification number and calibration date. This has to be filled before any testing is performed.

Table 7.3: Equipment and plant needed for this test

Equipment	Identification	Calibration / due date
Balance Scale		
Brushes, soft, diameter 2mm		
Compressed air		
Mixing cups, plastic		
Mixing paddles		
Ruler		
Spatulas		
Syringes		
Table		
Tampons for application		
of the promoter DC 1200-OS		
Vacuum cleaner or equivalent apparatus		

Table 7.4: Materials needed for this test

Name	Specification or Supplier
Avery Sign-Mask tape (gray)	Avery Dennision
Bleeder/Breather material Airwave N10FR	Aero Consultants Ltd.
ChoBond 1029 B	CHROMATICS
Clean, white cotton cloth	-
Clean, white, lint-free nylon cloth	[ECSS-Q-ST-70-01C, 2008]
Copper strip electrodes	-
CV 2646	Nusil
DC 1200 OS primer, adhesion promoter	Dow Corning
Dielectric Materials	Various manufacturers
Flashbreaker tape type 1	Aero Consultants Ltd.
Gloves, clean, white, lint-free nylon gloves	[ECSS-Q-ST-70-01C, 2008]
Gloves, Nitrile and powder free (IPA resistant)	[ECSS-Q-ST-70-01C, 2008]
Isopropyl Alcohol (IPA)	Merck or equivalent
Methyl Ethyl Ketone (MEK)	Merck or equivalent
Mylar foil	3M
Release film Wrightlon 4500 or equivalent	Aero Consultants Ltd.
RTV 566 (1-kit + catalyst dimetgylhydroxy(oleate) tin)	A.S.A.P. Technologies
SP-120	Nusil

7.2.2 Test Program

The goal of this subsection is to define: engineering tests, production of test panels, thermal cycling exposure and post-environmental performance testing.

Test samples

Test samples shall replicate bonding of copper electrodes with various dielectric materials using two different adhesives; namely RTV566+ChoBond and CV2646. CV2646 adhesive is already an electrically conductive adhesive, while in RTV566, ChoBond must be added in order to become electrically conductive. Conduction though adhesive is important as grounding of the actuator goes through dielectric material into surface that it is bonded to. Dielectric materials that will be bonded to aluminum plates are presented in Table 7.5. Each dielectric material has its index number from 1 to 12. That will be used later in marking the samples.

Table 7.5: Characteristics of various dielectric materials [Roth and Dai, 2006]

Material	Mass density ρ $[kg/m^3]$	Dielectric constant (ϵ_r)	Dielectric Strength (E) [kV/mm]	Dielectric loss $tan\delta$ (1MHz)	Loss Factor $\epsilon_r \cdot tan\delta$	References
1. Teflon	2160	2.1	11.2	0.0001	0.00021	DuPont
2. Quartz	2200	5	25	0.00001	0.00005	CEVP Ltd.
3. Aluminium Oxide	3700	9.4 (1 MHz)	15	0.0004	0.00376	KYOCERA
4. Glass	2600	3.8	10	0.004	0.0152	MatWeb
5. Lexan FR	1190	2.9 (1 MHz)	16	0.0085	0.02465	GE Plastics
6. Mica	2800	4-9	25	0.0013	0.0052-0.0117	McMaster
7. PC Board	1690	5	16.8	0.005	0.025	DuPont
8. Bakelite	1420	5-22	24	0.02	0.1-0.44	MatWeb
9. Kapton	1420	3.5	154	0.009 (100 kHz)	0.0315	DuPont
10. Garolite G10/FR4	1820	5.2	20 (62 mm)	0.0048	0.025	K-mac plastics
11. Garolite G7	1680	4.2	15 (62 mm)	0.00071	0.003	K-mac plastics
12. PMMA	1000	2.6 (1 MHz)	0.787-60	0.002-0.19	0.0056-0.76	MatWeb

In order to efficiently test all the above materials, one has to define a test panel. On this test panel there will be 24 samples, two for each dielectric material, as two adhesives will be tested. Test panel is presented in Figure 7.8. In this figure, test sample bonded with RTV566 + ChoBond is marked with number 1 and test sample bonded with CV2426 is marked with number 2. To clarify an example is used, sample 5.2 represents Lexan FR dielectric bonded with CV2646.
Sample plate dimensions cam be seen in Figure 7.8. Two of these panels will be produced. One panel will be subjected to thermal cycling while the other will be used as a reference sample.

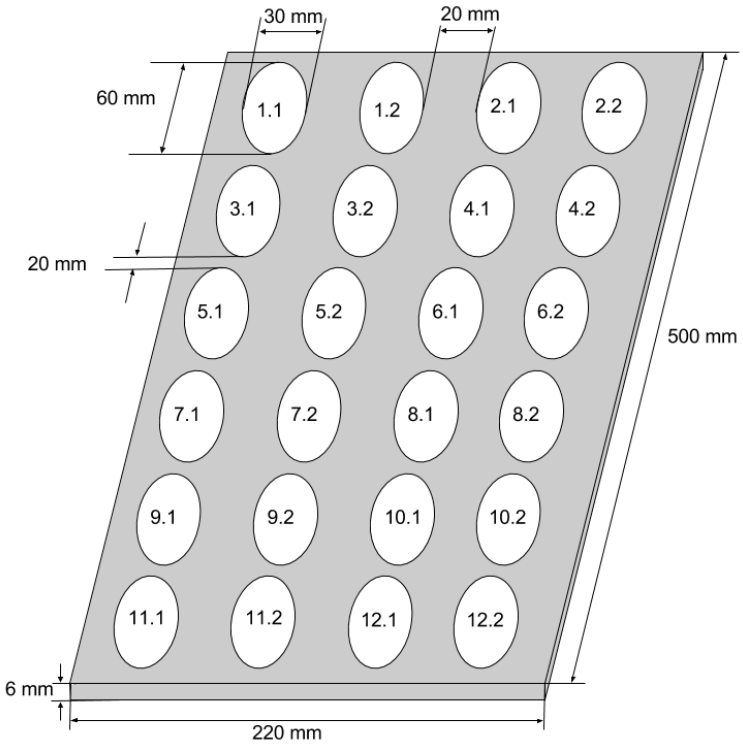

Figure 7.8: Combined test panel

Bonding procedures

Bonding of each sample will be performed using procedures stated in [ECSS-E-HB-32-21A, 2011] and Figure 7.9. In [ECSS-E-HB-32-21A, 2011] manual, information about surface preparation and application of adhesive can be found. However information about curing times is closely related to specific adhesive and cannot be found in manual. The choice of these two adhesives was primarily due to reason that they are both room temperature curing adhesives. Expected curing times for these adhesives is 7 days, but for exact times and application methods manufacturers shall be contacted.

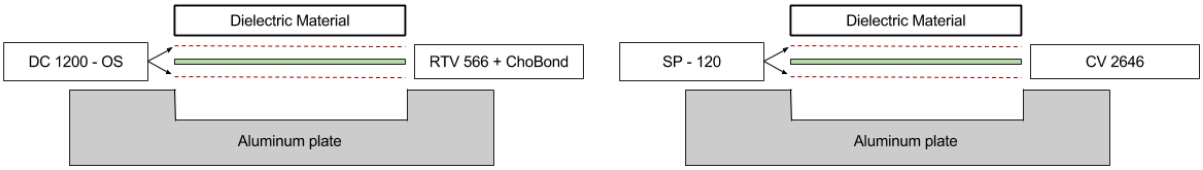

(a) (b)

Figure 7.9: Bonding of dielectric materials using RTV 566 + ChoBond (a) and CV 2646 (b) together with their primers DC1200-OS Red and SP-120

No other adhesive is used to bond or secure these parts from figure above. Therefore it is important to assess the behavior of the bonding system which will be submitted to thermal cycling during its mission. Visual inspection and dedicated test are planned to verify bonding strength with (panel A) and without (panel B)

thermal cycling.

Test procedures

After full cure, both panels shall be subjected to visual inspection prior to ambient pressure thermal cycling and vacuum thermal cycling to verify initial bonding and to check if actuator is able to withstand large temperature gradients. Next, panels shall be prepared and submitted to a dedicated pull test for each sample. In this way one will be able to compare effects of thermal cycling on different dielectrics and adhesives.

Visual inspection: The test samples shall be visually inspected for any defects (e.g. cracks, de-lamination or de-bonds) according to following method. Photographs of all test samples shall be taken. In case of detected defects, it also has to be photographed and reported.

Test method:	Visual inspection of panes with naked or aided eye
Test equipment:	Magnifying glass (x10 magnification)
Test samples:	See Figure 7.8 and Table 7.5
Test requirement:	See Section 7.2.4

Pull test: The adhesion of dielectric material samples shall be tested according to following method:

Test method:	Dedicated pull test
Test equipment:	Pull test device + metallic interface plate same as in the Figure 7.10
Test samples:	See Figure 7.8 and Table 7.5
Test requirement:	See Section 7.2.4

The pull test require preparation of dedicated interfaces Metallic plates shall be cut to the dielectric material sample dimensions and prepared in order to be an interface between the pulling machine and dielectric materials. This interface set-up cab ne seen in Figure 7.10.

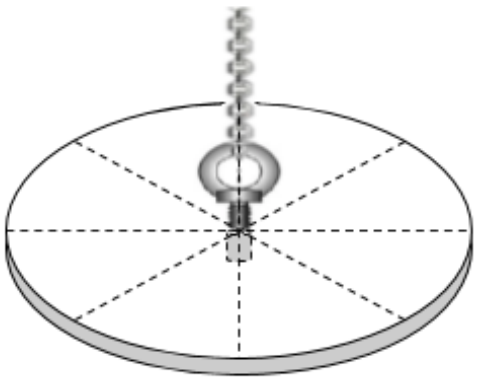

Figure 7.10: Interface between pull machine and test sample

Preparation of these interfaces consists of the following steps:

- Cutting the plates to the sample dimensions (oval 60 x 30 mm)
- Define the center of the metallic plate
- Drill a hole at the center of the plate
- Thread a hole to screw eye bolt (DIN 580)
- Adapt the eye bolt (DIN 580) to the thickness of the plate (6 mm)
- Verify the surface to the bonded (flatness and no impact of the eye bolt)

Firstly the dielectric material samples shall be bonded to a metallic backing plate using epoxy adhesive AW2101 after cleaning of each surface per. [ECSS-E-HB-32-21A, 2011] and [ECSS-Q-ST-70-01C, 2008]. This operation shall be done in order to prevent deformation of skins and breaking of dielectric material during the pull test. Secondly protection layers shall be installed around samples in order to avoid cyanoacrylate bonding between metallic plate and skins during next step. Thirdly the interface described in Figure 7.10 shall be cleaned and bonded on top of each sample with epoxy adhesive AW2101 just before pull tests.
Both plates will be tested. Each contain 24 actuator samples. Therefore there are in total 48 pull tests planed. Test speed of these pull tests shall be 1.5 ± 0.5 mm/minute.
Photographs of all samples shall be taken after pull tests to illustrates the nature of fractures (cohesive, inter-facial or mixed). Test values shall be reported as-is (no requirement).

Thermal cycling: After visual inspection sample panel A shall be submitted to thermal cycling while other plate shall be used as baseline reference. Panel A shall be subjected to ambient pressure thermal cycling and vacuum thermal cycling. Details about ambient pressure vacuum thermal cycling facilities that will be used are presented in Table 7.6 while the conditions under which this sample will be tested are presented in Table 7.7. It should be noted that if thermal vacuum chamber is not large enough, test panel shall be cut in half, with each containing six samples.

Table 7.6: Testing facilities

	Ambient pressure	Vacuum
Test Chamber	GRENCO (or equivalent)	Airbus DS Netherlands thermal vacuum facility
Temperature Rate [K/minute]	maximum 40	>10 [ECSS-Q-ST-70-04C, 2008]
Dwell time at temp. extremes	5 minutes minimum	5 minutes minimum

Table 7.7: Thermal cycling conditions

Phase	Pressure	Temperature °C		Number of cycles
		Minimum	Maximum	
Phase 1	Vacuum	-140	+140	5
Phase 2	Ambient	-140	+140	90
Phase 3	Vacuum	-140	+140	5

7.2.3 Test Sequence

Overview if test sequence can be found in Figure 7.11. This figure is divided into two main parts; where top par represents steps to be taken in the production of samples, while the bottom part shows different test types that will be performed.

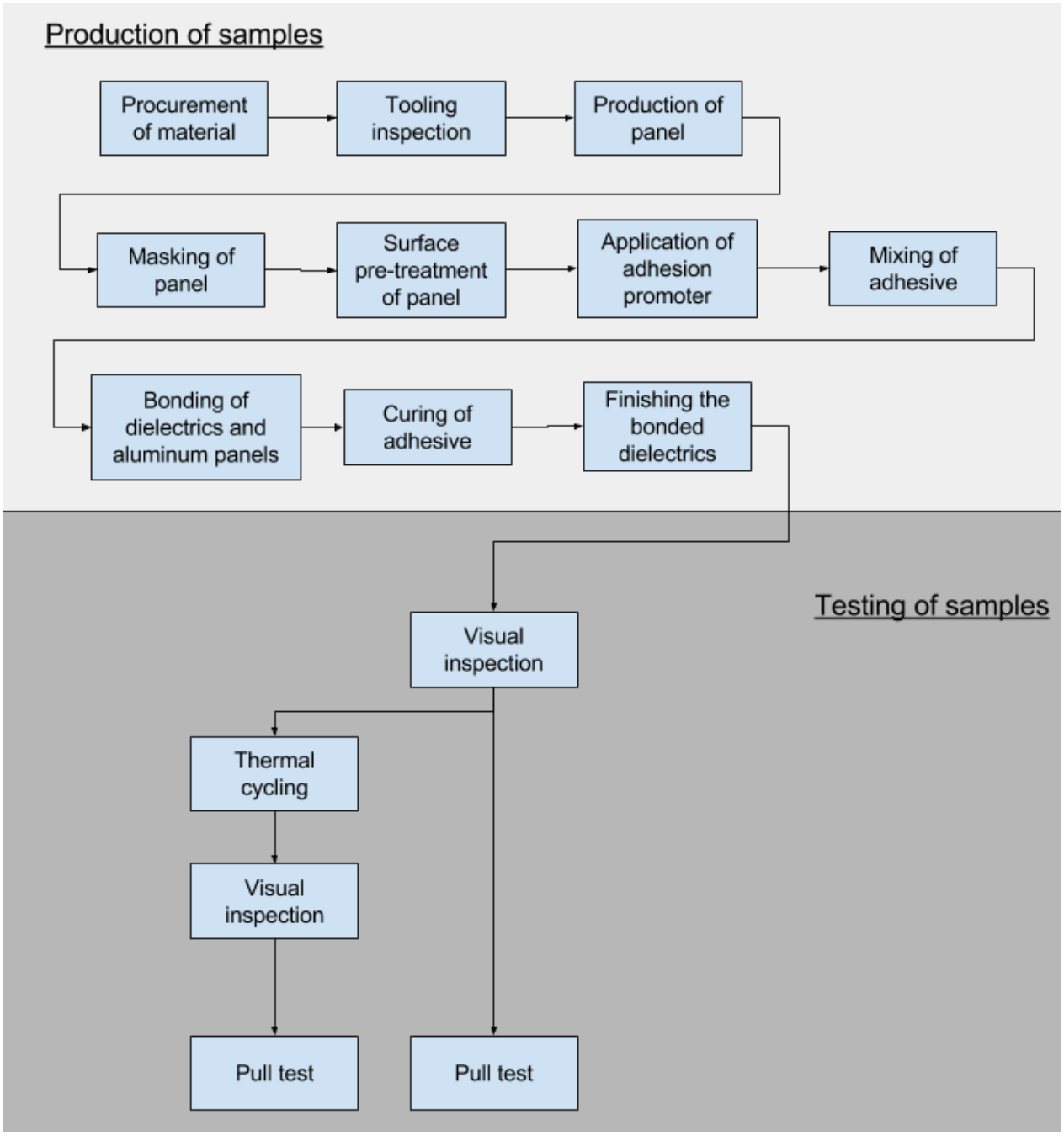

Figure 7.11: Flow down chart representing overview of test sequence

7.2.4 Pass/Fail Criteria

Samples will be graded with pass or fail according to the criteria below.

Visual inspections

Pass/fail requirements for visual inspections are:

- ✓ Adhesives and their primers shall show a homogeneous aspect
- ✓ Adhesives shall be free of cracks or local discoloration which can be a beginning of a crack
- *X* The samples shall not show any disbands between the silicon adhesive and the dielectric sample
- *X* Dielectric samples shall not show start of cracks and shall not be broken

Pull test

Pass/fail requirements for pull tests are:

- ✓ Good reproducibility of test results
- ✓ The pull tests on all adhesives shall have similar results
- ✓ The bonding of each dielectric material sample shall be sufficiently strong to withstand <**TBD**> N
- *X* The adhesion strength after thermal cycling shall be minimum 70% of the adhesion strength after thermal cycling (comparing two test panels)

7.3 Chapter Conclusions

Chapter 7 aims in providing actuator survivability information while spacecraft is in orbital stage of life. This is crucial if it is desired to operate DBD actuator during re-entry stage. This chapter is divided into two parts. First section covers Finite Element Method (FEM) modeling of thermal stresses occurring in actuator due to cyclic temperature gradients. Starting design point was actuator defined by [Pereira, 2016]. It had to be modified, both in shape and materials it is made from, due to large mismatches in coefficients of thermal expansion between parts composing actuator. Chosen part materials and stresses that occur, due to spacecraft's orbital motion and cyclic Sun exposure, are presented in Table 7.2. It shows that no part reaches its yield values, meaning that complete actuator is able to withstand all thermal stresses expected to occur. This provides required information and assurances needed in order to proceed and perform experimental tests needed in order to qualify this particular DBD plasma actuator for space-based applications. Second section of this chapter defines mentioned qualification test. When experiments are performed deeper knowledge of twelve dielectric materials, two room temperature curing adhesives and one electrode material will be obtained. This will provide foundation on which future research can build on in order to fly and operate DBD plasma actuator on space-based mission.

8 CONCLUSIONS AND RECOMMENDATIONS

Goal of this research was to check whether non-thermal plasma actuators could be used in space-based systems. These actuators show large potential when compared to mechanical actuators, due to their beneficial characteristics such as lower mass, faster response time, lower power consumption, and are less complex, making them more reliable. Figure 8.1 is modified version of Figure 1.1, which will help to clearly represent taken decisions and obtained results needed in order to answer research questions defined in Chapter 1.

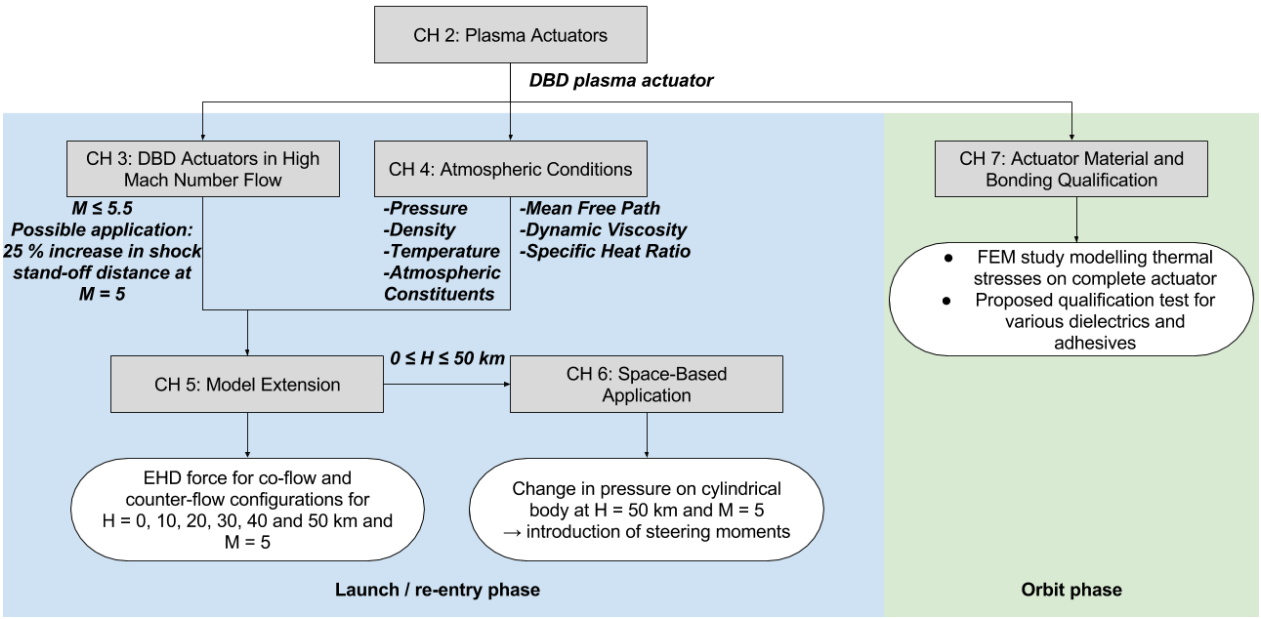

Figure 8.1: Thesis outline with main results

8.1 Conclusions

Chapter 2 was presented in order to choose appropriate actuator type for rest of thesis research. DBD actuators do not experience problems related to charge stability associated with discharge arcing occurring in corona discharge actuators. Thus DBD actuators can sustain a large volume discharge without it collapsing into a constricted arc. Stability benefits together with knowledge that this actuator type is currently developed, tested and used at Faculty of Aerospace Engineering of TU Delft, makes DBD, the actuator of choice. This can also be seen in Figure 8.1, which shows that output from Chapter 2 is DBD plasma actuator choice.

Following thesis outline, the input for chapters 3, 4 and 7 is DBD plasma actuator, based on decision earlier made. As DBD actuator is flush mounted to spacecraft's surface, it will be subjected to all environmental effects as outer structure of a spacecraft is subjected. This means that actuator will be subjected to flow characterized by high Mach number and atmospheric parameters defined by altitude. Hence, literature on DBDs subjected to high speed flow field and study on atmospheric parameters as a function of altitude were conducted. Chapter 3 gives an overview of DBD applications from transonic to hypersonic flow fields. Litera-

ture shows several major problems related to high Mach number flow fields. [Nishihara et al., 2011] state that it is difficulty to conserve high discharge electric field and high space charge density in supersonic and hypersonic flows. In addition to these, with Mach numbers higher than 5.5 dissociation of molecules will occur as temperatures at stagnation point reach 2000 K. Finally hypersonic flow as modelled by [Bhatia et al., 2014] is followed by problems associated with high temperatures, meaning that no dielectric materials could withstand temperatures of 12500 K. In order to limit the scope of this research it was decided not to exceed flow fields with $M \geq 5.5$. If DBD plasma actuator is positioned near stagnation point at M=5, it will be capable of modifying natural bow shock, by increasing its stand-off distance for a quarter of its original value [Nishihara et al., 2011]. Shock modification is manifested as change in pressure on a spacecraft. This was the only feasible application that could be found. In order to keep up with scope limitation earlier said, it was decided to keep M=5 for rest of this thesis.

In Chapter 4 all relevant atmospheric parameters are presented either as a function of altitude or temperature. All results and figures are based on three different models for both low and moderate solar activity. This chapter computes and provides information about: pressure, density, temperature, number of atmospheric constituents, mean free path, dynamic viscosity and specific heat ratio for altitude range from sea level to 400 km.

Thesis outline in Figure 8.1 shows that all previous chapters provide necessary information needed in order to extend an existing parametric model made by [Pereira, 2016]. This model estimates two dimensional forces occurring due to momentum exchanged between neutral particles and charged ions created by single DBD surface plasma actuator. Original model was limited to sea level conditions meaning that it could not take altitude variations into account, so an extension was made. With one additional assumption new extended model is able to estimate force variations for altitudes up until 50 km for both co-flow and counter flow forcing configurations. At altitude of 50 km it is clear that crated force is only a fraction of one produced at sea level altitude. For external flow velocity of 50 m/s in co-flow configuration, model estimates load cell force equal to 90 mN and 0.22 mN for 10 km and 50 km altitude respectively. It was found that per 10 km force drops for 4.51 and 4.44 times for co-flow and counter flow configurations. As density is linearly proportional to produced force and on average decreases 4.19 times each 10 km in altitude, it can be assumed that it is the main contributor to force drop ratio. Due to numerous assumptions listed in Section 5.3, phenomenon behind linear force vs. altitude decreasing trend is not fully understood and has to be investigated in further research.

Knowing that force production is available at an altitude of 50 km and combining two studies made by [Nishihara et al., 2011] and [Sinclair and Cui, 2017] a brief concept application is presented. Chapter 6 presents a correlation between an increase of shock stand-off distance and pressure distribution on cylindrical body. Thus due to instantaneous change in pressure, steering moments on spherical body can be introduced. This being a first order feasibility study, spacecraft body shape (spherical cylinder) was chosen in order to keep scope narrow and focused on research questions. These steering moments could be used during spacecraft's launch and re-entry stages.

Last research question checks DBD actuator's ability to withstand thermal loads expected to occur during orbit stage of spacecraft life. Answer to this question is given in Chapter 7, which comprises of two sections. First part models thermal loads using FEM tool named ANSYS. Modelled actuator is a modified version of

one used in [Pereira, 2016] dissertation. Modification had to be made so that no actuator part reaches its yield stress value. This was an iterative process as each actuator parts are made from different materials, having dissimilar coefficients of thermal expansion. One of many possible combinations was chosen. It defines actuator made from: cold drawn Copper electrodes, Lexan FR dielectric and 6061-T6 aluminum spacecraft surface. Modelling of this particular actuator in thermal cycling environment from -140 °C to +140 °C showed that none of the actuator parts reaches its yield stresses. This gave confidence to define qualification test, which is presented in second part of Chapter 7. Test is designed such that faculty will obtain large bank of qualified materials for the cost of one.

8.2 Final Notes and Recommendations

This study provides a first insight in use of single DBD plasma actuators in space-based applications. The amount of available research on this subject is very limited. Hence many opportunities for future research and development will be available due to numerous benefits that DBD plasma actuation has over conventional methods. Thesis presents an extensive literature study on most available research concerning DBDs in space applications. It covers all life stages from launch to re-entry. Knowledge concerning altitude effects on force production is extended from 12 km made by [Benard et al., 2008a] to 50 km. Presented thesis shows correlation between change in shock stand-off distance, produced by DBD actuation, and pressure distribution on cylindrical body. This correlation proves that DBD actuators are able to introduce forces that could be used for spacecraft steering applications. Last part of this thesis designs and tests actuator so that it can withstand thermal cycling loads occurring during spacecraft orbital motion.

Much research is needed before this actuator could fly on space mission. Concerning this thesis several recommendations could be given. These are presented in list below.

- Model shall be extended beyond 50 km in altitude. Assumption made that E/p_0 ratios are constant need to be excluded, meaning that research made by [Varney, 1953] had to be revisited.
- Model shall be modified even further to take into account flow fields characterized with Mach numbers higher than 5.5. Hence model shall take dissociation of molecules into account. As earlier stated, high velocities are characterized by large heat loads. According to available literature no dielectric material is able to withstand these temperatures, meaning that actuator would require either development of some new materials or some cooling technique. As this would probably significantly increase mass and cost of an entire system, a cost-benefit analysis shall be conducted.
- Component degradation due to strong radiation and lack of shielding during orbital phase shall also be tested.
- During launch and re-entry phases stresses and vibrations will occur. In order to fully qualify DBD actuator, a proper design and testing are required.
- Space-based DBD actuator requires much research in order to be optimized. Some of the areas that shall be optimized are:

    1. geometrical parameters of an actuator (electrode and dielectric length, width and thickness)

2. electrode and dielectric material,
3. high voltage waveform input and frequency,
4. electrode shape, and
5. actuator placement on spacecraft

- Finally a multi-electrode configurations shall be investigated as they increase overall efficiency and effectiveness of DBD actuator system.

At this point it is not safe to say that DBD actuators have future in space systems, even though this research shows promising results. Most probable applications concern the currently developing returning rockets such as SpaceX's Falcon 9, on which plasma actuators could be used for drag reduction and steering applications. Only after above stated recommendations are performed, a cost benefit analysis shall be done, which would help determine future of these actuators in space-based systems.

Bibliography

[Alperin, 1950] Alperin, M. (1950). *A study of detached shock waves in two-dimensions*. PhD thesis, California Institute of Technology.

[Anderson Jr, 2010] Anderson Jr, J. D. (2010). *Fundamentals of aerodynamics*. Tata McGraw-Hill Education.

[Atkinson et al., 2013] Atkinson, M., Poggie, J., and Camberos, J. (2013). Control of high-angle-of-attack reentry flow with plasma actuators. *Journal of Spacecraft and Rockets*, 50(2):337–346.

[Atkinson, 2012] Atkinson, M. D. (2012). *Control of hypersonic high angle-of-attack re-entry flow using a semi-empirical plasma actuator model*. PhD thesis, University of Dayton.

[Atmosphere, 1976] Atmosphere, U. S. (1976). National oceanic and atmospheric administration. *Aeronautics and Space Administration, United States Air Force, Washington, DC*.

[Balcon et al., 2009] Balcon, N., Benard, N., and Moreau, E. (2009). Formation process of the electric wind produced by a plasma actuator. *IEEE Transactions on Dielectrics and Electrical Insulation*, 16(2):463–469.

[Benard et al., 2008a] Benard, N., Balcon, N., and Moreau, E. (2008a). Electric wind produced by a surface dielectric barrier discharge operating in air at different pressures: aeronautical control insights. *Journal of Physics D: Applied Physics*, 41(4):042002.

[Benard et al., 2013] Benard, N., Debien, A., and Moreau, E. (2013). Time-dependent volume force produced by a non-thermal plasma actuator from experimental velocity field. *Journal of Physics D: Applied Physics*, 46(24):245201.

[Benard et al., 2008b] Benard, N., Jolibois, J., Touchard, G., and Moreau, E. (2008b). A directional plasma-jet device generated by double dbd actuators: an active vortex generator for aerodynamic flow control. In *4th Flow Control Conference*, page 3763.

[Benard and Moreau, 2014] Benard, N. and Moreau, E. (2014). Electrical and mechanical characteristics of surface ac dielectric barrier discharge plasma actuators applied to airflow control. *Experiments in Fluids*, 55(11):1–43.

[Bhatia et al., 2014] Bhatia, A., Roy, S., and Gosse, R. (2014). Effect of dielectric barrier discharge plasma actuators on non-equilibrium hypersonic flows. *Journal of Applied Physics*, 116(16):164904.

[Bisek et al., 2014] Bisek, N. J., Poggie, J., Nishihara, M., and Adamovich, I. (2014). Hypersonic flow over a cylinder with a nanosecond pulse electrical discharge. *Journal of Thermophysics and Heat Transfer*, 28(1):18–26.

[Bletzinger et al., 2005] Bletzinger, P., Ganguly, B., Van Wie, D., and Garscadden, A. (2005). Plasmas in high speed aerodynamics. *Journal of Physics D: Applied Physics*, 38(4):R33.

[Boeuf et al., 2009] Boeuf, J., Lagmich, Y., and Pitchford, L. (2009). Contribution of positive and negative ions to the electrohydrodynamic force in a dielectric barrier discharge plasma actuator operating in air. *Journal of applied physics*, 106(2):023115.

[Bowman et al., 2008] Bowman, B., Tobiska, W. K., Marcos, F., Huang, C., Lin, C., and Burke, W. (2008). A new empirical thermospheric density model jb2008 using new solar and geomagnetic indices. In *AIAA/AAS Astrodynamics specialist conference and exhibit*, page 6438.

[Chul-Soo, 1956] Chul-Soo, K. (1956). Experimental studies of supersonic flow past a circular cylinder. *Journal of the Physical Society of Japan*, 11(4):439–445.

[Corke et al., 2010] Corke, T. C., Enloe, C. L., and Wilkinson, S. P. (2010). Dielectric barrier discharge plasma actuators for flow control*. *Annual review of fluid mechanics*, 42:505–529.

[Corke et al., 2007] Corke, T. C., Post, M. L., and Orlov, D. M. (2007). Sdbd plasma enhanced aerodynamics: concepts, optimization and applications. *Progress in Aerospace Sciences*, 43(7):193–217.

[Corke et al., 2009] Corke, T. C., Post, M. L., and Orlov, D. M. (2009). Single dielectric barrier discharge plasma enhanced aerodynamics: physics, modeling and applications. *Experiments in Fluids*, 46(1):1–26.

[Debien et al., 2012] Debien, A., Benard, N., David, L., and Moreau, E. (2012). Unsteady aspect of the electrohydrodynamic force produced by surface dielectric barrier discharge actuators. *Applied Physics Letters*, 100(1):013901.

[ECSS-E-HB-32-21A, 2011] ECSS-E-HB-32-21A (2011). Space engineering: Adhesive bonding handbook, volume = 2011, address = ESA Requirements and Standards Division, ESTEC, P.O. Box 299, 2200 AG Noordwijk The Netherlands, institution = European Cooperation for Space Standardization. Standard.

[ECSS-E-ST-10-04C, 2008] ECSS-E-ST-10-04C (2008). Space engineering: Space environment. Standard, European Cooperation for Space Standardization, ESA Requirements and Standards Division, ESTEC, P.O. Box 299, 2200 AG Noordwijk The Netherlands.

[ECSS-Q-ST-70-01C, 2008] ECSS-Q-ST-70-01C (2008). Product assurance: Cleanliness and contamination control, volume = 2008, address = ESA Requirements and Standards Division, ESTEC, P.O. Box 299, 2200 AG Noordwijk The Netherlands, institution = European Cooperation for Space Standardization. Standard.

[ECSS-Q-ST-70-04C, 2008] ECSS-Q-ST-70-04C (2008). Product assurance: Thermal testing for the evaluation of space materials processes mechanical parts and assemblies, volume = 2008, address = ESA Requirements and Standards Division, ESTEC, P.O. Box 299, 2200 AG Noordwijk The Netherlands, institution = European Cooperation for Space Standardization. Standard.

[Enloe et al., 2009] Enloe, C., McHarg, M., Font, G., and McLaughlin, T. E. (2009). Plasma-induced force and self-induced drag in the dielectric barrier discharge aerodynamic plasma actuator. *AIAA Paper*, 1622:2009.

[Enloe et al., 2004] Enloe, C., McLaughlin, T. E., Van Dyken, R. D., Kachner, K., Jumper, E. J., and Corke, T. C. (2004). Mechanisms and responses of a single dielectric barrier plasma actuator: plasma morphology. *AIAA journal*, 42(3):589–594.

[Fatemi et al., 2013] Fatemi, N., Lyons, J., and Eskenazi, M. (2013). Qualification and production of emcore ztj solar panels for space missions. *Photovoltaic Specialists Conference (PVSC), 2013 IEEE 39th*, pages 2793–2796.

[Font et al., 2009] Font, G., Enloe, C., and McLaughlin, T. E. (2009). Effect of volumetric momentum addition on the total force production of a plasma actuator. *AIAA paper*, 4285.

[Goldman et al., 1985] Goldman, M., Goldman, A., and Sigmond, R. (1985). The corona discharge, its properties and specific uses. *Pure and Applied Chemistry*, 57(9):1353–1362.

[Grundmann and Tropea, 2007] Grundmann, S. and Tropea, C. (2007). Experimental transition delay using glow-discharge plasma actuators. *Experiments in Fluids*, 42(4):653–657.

[Im et al., 2010] Im, S., Do, H., and Cappelli, M. (2010). Dielectric barrier discharge control of a turbulent boundary layer in a supersonic flow. *Applied Physics Letters*, 97(4):041503.

[Jayaraman and Shyy, 2008] Jayaraman, B. and Shyy, W. (2008). Modeling of dielectric barrier discharge-induced fluid dynamics and heat transfer. *Progress in Aerospace Sciences*, 44(3):139–191.

[Kaattari, 1961] Kaattari, G. E. (1961). Predicted shock envelopes about two types of vehicles at large angles of attack.

[Kotsonis and Ghaemi, 2012] Kotsonis, M. and Ghaemi, S. (2012). Performance improvement of plasma actuators using asymmetric high voltage waveforms. *Journal of Physics D: Applied Physics*, 45(4):045204.

[Kriegseis et al., 2012] Kriegseis, J., Schwarz, C., Duchmann, A., Grundmann, S., and Tropea, C. (2012). Piv-based estimation of dbd plasma-actuator force terms. *AIAA paper*, 411:2012.

[Leger et al., 2002] Leger, L., Moreau, E., and Touchard, G. (2002). Electrohydrodynamic airflow control along a flat plate by a dc surface corona discharge—velocity profile and wall pressure measurements. *AIAA paper*, 2833:2002.

[Likhanskii et al., 2008] Likhanskii, A. V., Shneider, M. N., Macheret, S. O., and Miles, R. B. (2008). Modeling of dielectric barrier discharge plasma actuator in air. *Journal of Applied Physics*, 103(5):053305.

[Massines et al., 1998] Massines, F., Rabehi, A., Decomps, P., Gadri, R. B., Ségur, P., and Mayoux, C. (1998). Experimental and theoretical study of a glow discharge at atmospheric pressure controlled by dielectric barrier. *Journal of Applied Physics*, 83(6):2950–2957.

[McKnight, 1970] McKnight, L. (1970). Drift velocities and interactions of negative ions in oxygen. *Physical Review A*, 2(3):762.

[Moreau, 2007] Moreau, E. (2007). Airflow control by non-thermal plasma actuators. *Journal of Physics D: Applied Physics*, 40(3):605.

[Nishihara et al., 2011] Nishihara, M., Takashima, K., Rich, J., and Adamovich, I. (2011). Mach 5 bow shock control by a nanosecond pulse surface dielectric barrier discharge. *Physics of Fluids*, 23(6):066101.

[Pal et al., 2012] Pal, S., Sriram, R., Rao, M. S., and Jagadeesh, G. (2012). Effect of dielectric barrier discharge plasma in supersonic flow. In *28th International Symposium on Shock Waves*, pages 867–872. Springer.

[Pavon et al., 2007] Pavon, S., Dorier, J., Hollenstein, C., Ott, P., and Leyland, P. (2007). Effects of high-speed airflows on a surface dielectric barrier discharge. *Journal of Physics D: Applied Physics*, 40(6):1733.

[Pereira, 2016] Pereira, R. (2016). *Active Stall Control for Horizontal Axis Wind Turbines*. PhD thesis, TU Delft, Kluyverweg 1, 2629 HS Delft.

[Pereira et al., 2014] Pereira, R., Ragni, D., and Kotsonis, M. (2014). Effect of external flow velocity on momentum transfer of dielectric barrier discharge plasma actuators. *Journal of Applied Physics*, 116(10):103301.

[Pons et al., 2004] Pons, J., Moreau, E., and Touchard, G. (2004). Electrical and aerodynamic characteristics of atmospheric pressure barrier discharges in ambient air. In *ISNTPT-4*, pages 307–310.

[Popov, 2001] Popov, N. (2001). Investigation of the mechanism for rapid heating of nitrogen and air in gas discharges. *Plasma physics reports*, 27(10):886–896.

[Porter et al., 2007] Porter, C., Baughn, J., McLaughlin, T., Enloe, L., and Font, G. (2007). Plasma actuator force measurements. *AIAA journal*, 45(7):1562–1570.

[Post and Corke, 2004] Post, M. L. and Corke, T. C. (2004). Separation control on high angle of attack airfoil using plasma actuators. *AIAA journal*, 42(11):2177–2184.

[Robinson, 1961] Robinson, M. (1961). Movement of air in the electric wind of the corona discharge. *Transactions of the American Institute of Electrical Engineers, Part I: Communication and Electronics*, 80(2):143–150.

[Roth and Dai, 2006] Roth, R. and Dai, X. (2006). Optimization of the aerodynamic plasma actuator as an electrohydrodynamic (ehd) electrical device. *AIAA paper*, 1203.

[SABIC Lexan, 2009] SABIC Lexan (2009). Lexan, valox and ultem films, volume = 2009, address = Plasticslaan 1, 4612 PX Bergen op Zoom, The Netherlands, institution = SABIC Innovative Plastics. Technical manual.

[Schlatter, 2009] Schlatter, T. W. (2009). Atmospheric composition and vertical structure. *Earth System Research Laboratory, National Oceanic and Atmospheric Administration, Boulder, CO, USA*.

[Schutze et al., 1998] Schutze, A., Jeong, J. Y., Babayan, S. E., Park, J., Selwyn, G. S., and Hicks, R. F. (1998). The atmospheric-pressure plasma jet: a review and comparison to other plasma sources. *IEEE transactions on plasma science*, 26(6):1685–1694.

[Sigmond and Lågstad, 1993] Sigmond, R. and Lågstad, I. (1993). Mass and species transport in corona discharges. *High Temp. Chem. Processes*, 2(4):5.

[Sinclair and Cui, 2017] Sinclair, J. and Cui, X. (2017). A theoretical approximation of the shock standoff distance for supersonic flows around a circular cylinder. *Physics of Fluids*, 29(2):026102.

[Sriram et al., 2012] Sriram, R., Jagadeesh, G., and Reddy, K. (2012). Experimental investigations on the effect of dielectric barrier discharge on the hypersonic flow around a flat plate. In *28th International Symposium on Shock Waves*, pages 979–985. Springer.

[Varney, 1953] Varney, R. N. (1953). Drift velocity of ions in oxygen, nitrogen, and carbon monoxide. *Physical Review*, 89(4):708.